

ዘዴ

የኢትዮጵያ መሠሪያ ስርዓት ስርዓት ስርዓት መጽሔት

ISSN: 0514-6216

Indexed on  
AJOL

zede

**Journal of Ethiopian Engineers and Architects**

**38**

ሐምሌ ፳፻፳  
July 2020

Annual Publication of the Addis Ababa Institute of Technology  
Addis Ababa University



የኢትዮጵያ መሰሪያዎችና አርኪቴክቶች መጽሔት

# Zede

Journal of Ethiopian Engineers and Architects

፳፻፲፯፻፺፯ Established 1963	ሐምሌ ፳፻፳፯ July 2020	<b>38</b>	፳፻፲፯፻፺፯ P.O.Box 385	አዲስ አበባ Addis Ababa
-----------------------------	-----------------------	-----------	------------------------	------------------------

**Editor-in-Chief**  
*Abebe Dinku*

**Asso. Editor**  
*Mohammed Abdo*

**Editorial Board Members**  
*Adil Zekaria*  
*Beyong Soo Lim*  
*Beteley Tekola*  
*Edessa Dribssa*  
*Getachew Bekele*  
*Heyaw Terefe*

**Publisher**  
Addis Ababa University  
AAU Printing Press  
P.O.Box 1178  
Addis Ababa  
Ethiopia

**Postal Address**  
Addis Ababa University, AAiT  
P.O.Box 385  
Addis Ababa  
Ethiopia

**Website:** [www.aait.edu.et/zede](http://www.aait.edu.et/zede)  
**Email:** [zede@aait.edu.et](mailto:zede@aait.edu.et)

## CONTENTS

### Pages

- Sieve Tray Pressure Drop by Means of CFD Modeling and Simulation  
**by: *Getye Gesit*** 1
- Practical Considerations for Diminishing Piled Rafts on Weak Layered Soils  
**by: *Henok Fikre*** 13
- Neutral Axis Depth Profile of Reinforced Concrete Beams  
**by: *Abrham Gebre*** 27
- Ancient Ethiopic Manuscripts Character Recognition Using Deep Belief Networks  
**by: *Siranesh Getu, Eneyachew Tamir and Menore Tekeba*** 37
- Effects of Etching Process Inaccuracy in the Malfunctioning Level of PCB Circuits - A Simulation Based Analysis  
**by: *Hgigat Aregawi and Mohammed Abdo*** 53
- Performance Comparison of Inverted Land F-Shape Dual Band Micro strip Antenna  
**by: *Solomon Muluneh and Fikreselam Gared*** 65
- Application Layer DDoS Attack Detection in the Presence of Flash Crowd  
**by: *Biruk Asmare Muse and Surafel Lemma Abebe*** 75

THE EDITORIAL BOARD IS NOT RESPONSIBLE FOR VIEWS EXPRESSED BY INDIVIDUAL AUTHORS.

## Guide to Authors

ZEDE is a scientific journal on engineering science and application, produced under the auspices of the Addis Ababa Institute of Technology, Addis Ababa University. The main objective of the journal is to publish research articles, findings and discussions on engineering sciences, technology and architecture thereby assisting in the dissemination of engineering knowledge and methodologies in solving engineering problems. Technical Notes of significant contribution may be considered for publication.

Original papers for publication in the journal should be submitted in triplicate to the Editor-in-Chief, P.O. Box 385, Addis Ababa, Ethiopia. All articles submitted for publication in the journal should comply with the following requirements:

**1. Title of Paper:** The title of the paper should be phrased to include only key words and must have a length of not exceeding 80 characters including spaces.

**2. Format of Manuscript:** The manuscript should be (double-spaced single column draft and single spaced double column final) in A-4 sized paper with MS word 2007 or later version. Margins of 25 mm should be used on all sides of the paper.

**3. Length of Article:** The length of the article should not exceed word equivalent of 6000 words, or 20 pages, double spaced using font size 12 typed in Times New Roman.

**4. Author's Affiliation:** The author's full name, institutional affiliation and rank, if applicable, must appear on the paper.

**5. Abstract:** All articles submitted must include an abstract of length not exceeding 200 words in *italics*.

**6. Keywords:** All articles submitted must include Keywords not exceeding 6 in number.

**7. Style of Writing:** It is recommended that third person pronoun/s be used when referring to author/s.

**8. Illustrations:** Figures should be drawn in black, at a size with a 50% reduction to fit in 160 mm width of journal. Photographs should be submitted as glossy prints. Explanations and descriptions must be placed in the text and not within figures. All figures must include numbered captions. See example:

Figure 1 Typical creep strain versus time curve

**9. Tables:** Tables must be numbered in the same order as cited in the text. Explanations of tables must appear in the text.

**10. Equations:** Equations numbers should be right-justified. See example:

$$u(x, y) = -y\theta(x) \quad (1)$$

**11. References:** References in the body of the Article should be cited at the end of the paper by placing a reference number in square brackets and should be arranged sequentially as they appear in the text. Ethiopian names may be given in direct order, i.e. given name followed by father's name. All main words in titles (papers, books, reports) should be initialized by capital letters. Items in citations should be separated by commas. Page numbers should be included whenever applicable

### Examples:

#### 1. References to Journal Articles and Proceedings

Spillers, W.R. and Lefeochilos, E.,  
"Geometric Optimization Using Simple Code Representation", Journal of the Structural Division, ASCE, vol. 106, no. ST5, 1980, pp. 959-971.

#### 2. References to Books and Reports

Korsch, H.L. and Jodl, H. -J.,  
"Chaos: A Program Collection for the PC", Springer-Verlag, 1994.

**12. Units:** SI units must be used.

**13. Conclusions:** A set of conclusions must be included at the end of the paper.

#### 14. Submission of Paper:

Any paper submitted for publication in ZEDE must not have been published previously, or submitted for publication elsewhere; and if accepted for publication by ZEDE, the author/s shall transfer the copy right to ZEDE.

# SIEVE TRAY PRESSURE DROP BY MEANS OF CFD MODELING AND SIMULATION

Getye Gesit

School of Chemical and Bio Engineering, Addis Ababa Institute of Technology,  
Addis Ababa University, Addis Ababa, Ethiopia  
E-mail: getye.gesit@aait.edu.et

## ABSTRACT

*Sieve trays must be designed to have and operated at acceptably low enough tray pressure drop. Both of these tasks (i.e., tray design and tray analysis) require method(s) for sieve tray pressure drop determination. So far, only empirical correlations have been used for sieve tray pressure drop estimation. However, the correlations are not based on actual mechanics of flow but are based on gross oversimplifications and empirical correlations— hence often have large errors and are not reliable. A reliable and accurate way for the pressure drop determination can be achieved by use of working computational fluid dynamics (CFD) modeling and simulation. With working CFD model provided, the CFD modeling and simulation is mechanistic and first principles based or fundamentals based. In this work, a CFD model is developed and used to model and simulate and predict sieve tray pressure drop. The model considers the three-dimensional two-phase flow of gas (or vapour) and liquid in which each phase is treated as an interpenetrating continuum having separate transport equations. Interaction between the two phases occurs via interphase momentum transfer. For the CFD analysis, the commercial package CFX 17.0 of ANSYS was employed. Total and dry tray pressure drops are predicted for various combinations of gas and liquid flow rates. Predicted results are unacceptable and good agreement with experimental results.*

*The objective of the work was developing CFD model for sieve tray pressure drop and studying and finding out the extent to which the CFD modeling and simulation can be used as a prediction and design tool and method for sieve tray pressure drop. From the results and the CFD model performance, it is concluded that the CFD model provided here is acceptably good for sieve tray pressure drop modeling and simulation and hence is acceptably good for tray design and analysis.*

**Keywords:** Sieve Tray, Pressure Drop, Tray Pressure Drop, Tray Design and Analysis, CFD Modeling and Simulation

## INTRODUCTION

Sieve trays are widely used as phase contacting devices. They are commonly used in distillation that is the dominant separation process of the chemical and related processing industries. They are also used in the closely related mass transfer operations of absorption and stripping as well as in liquid-liquid extraction. Low cost, high separation efficiency, simplicity of fabrication and non-proprietary nature are some of the reasons that make sieve trays the first choice and standard column internals. Sieve tray design information may also be extended to the design of other type of trays.

Sieve trays must be designed to have and operated at acceptably low enough tray pressure drop. Both of these tasks (i.e., tray design and tray analysis) require method(s) for sieve tray pressure drop determination. So far, only empirical correlations have been used for sieve tray pressure drop estimation. However, the correlations are not based on actual mechanics of flow but are based on gross oversimplifications and empirical correlations— hence often have large errors and are not reliable.

Therefore, better models and methods of modeling and predicting sieve tray hydrodynamics and determining sieve tray pressure drop are of paramount significance and in dire need.

Recently, the development of powerful computers, advances in numerical methods, and improvements in multiphase flow models permit the investigation of complex flow problems. The technique that combines these is computational fluid dynamics (CFD), a technique that is emerging as an important predictive and design tool for flows in process equipment. Solution of the momentum, mass and energy transfer equations gives for each phase the time and spatial distribution fields of velocities, temperatures, pressures, volume fractions, and concentrations or compositions such as mole or mass fractions of species or components. The concern of this work is pressure drop determination. From the pressure solution distribution field of the CFD model and simulation, pressure drop can be calculated.

No CFD work has been done so far that is solely devoted to sieve tray pressure drop alone. There are no direct attempts made to use CFD for sieve tray pressure drop modeling and simulation Noriler, D, whose work was devoted to prediction of

efficiencies, only briefly and partially mentions the prediction of tray pressure drop using CFD. [2], [3] whose works were devoted to prediction of weeping by CFD technique, present comparison of experimental and CFD prediction of sieve tray dry pressure drop. Therefore, so far there no works done that can be used to know first what models to use and second if CFD technique can be used for sieve tray pressure drop modeling and simulation.

The work of this paper is the only first work that presents and answers first what models to use and second if CFD technique can be used for sieve tray pressure drop modeling and simulation. In the work here, a CFD model is presented to model, simulate and predict the hydrodynamics and total and dry pressure drops of sieve trays. This work here studies, answers and presents modeling issues such as what flow geometry model to use, what mathematical model equations to use, what closure relations to use, there is a need to include the tray thickness, and what boundary conditions models to use. Tray geometry and fluids are based on the work of [4].

The CFD simulation results are unacceptable and good agreement with the experimental results of Thomas. The objective of this work was developing CFD model and studying and finding out the extent to which the CFD modeling and simulation can be used as a modeling and simulation and prediction tool and method for pressure drop of sieve trays. From the results and the CFD model performance, it is concluded that the CFD model provided here is acceptably good for sieve tray pressure drop modeling and simulation and hence is acceptably good for tray design and analysis.

## MODEL EQUATIONS

The model considers the flow of gas (or vapour) and liquid in the Eulerian-Eulerian framework in which each phase is treated as an interpenetrating continuum having separate transport equations. With the model focusing on the liquid-continuous region of the sieve tray as done in [5,6], the gas phase is taken as the dispersed phase and the liquid phase as the continuous phase. Since the focus is on the pressure drop behaviour of sieve trays, energy transfer has not been considered in this work since that has little or no effect on tray pressure drop simulations since the flow is essentially isothermal and incompressible. Thus for each phase the time and volume averaged continuity and momentum equations were numerically solved.

### Continuity Equations

#### Gas phase

$$\frac{\partial}{\partial t}(r_G \rho_G) + \nabla \cdot (r_G \rho_G \mathbf{V}_G) = 0 \quad (1)$$

#### Liquid phase

$$\frac{\partial}{\partial t}(r_L \rho_L) + \nabla \cdot (r_L \rho_L \mathbf{V}_L) = 0 \quad (2)$$

### Momentum Equations

#### Gas phase

$$\begin{aligned} \frac{\partial}{\partial t}(r_G \rho_G \mathbf{V}_G) + \nabla \cdot (r_G \rho_G \mathbf{V}_G \mathbf{V}_G) = \\ -r_G \nabla p_G + \nabla \cdot [r_G \mu_{eff,G} (\nabla \mathbf{V}_G + \\ (\nabla \mathbf{V}_G)^T)] + r_G \rho_G \mathbf{g} - M_{LG} \end{aligned} \quad (3)$$

#### Liquid phase

$$\begin{aligned} \frac{\partial}{\partial t}(r_L \rho_L \mathbf{V}_L) + \nabla \cdot (r_L \rho_L \mathbf{V}_L \mathbf{V}_L) = -r_L \nabla p_L + \\ \nabla \cdot [r_L \mu_{eff,L} (\nabla \mathbf{V}_L + (\nabla \mathbf{V}_L)^T)] + r_L \rho_L \mathbf{g} + \\ M_{LG} \end{aligned} \quad (4)$$

Equations (1) to (4) are for the unsteady state case. For the steady state case, terms involving the time derivative are zero. As

one source for the equations, the ANSYS CFX 17.0 Documentation *ANSYS CFX* [7] can be consulted.

The gas and liquid volume fractions,  $r_G$  and  $r_L$ , are related by the summation constraint:

$$r_G + r_L = 1 \quad (5)$$

The same pressure field has been assumed for both phases, i.e.,

$$p_G = p_L \quad (6)$$

$\mu_{eff,G}$  and  $\mu_{eff,L}$  are the effective viscosities of the gas and liquid phase, respectively, obtained as:

$$\mu_{eff,G} = \mu_{laminar,G} + \mu_{turbulent,G} \quad (7)$$

$$\mu_{eff,L} = \mu_{laminar,L} + \mu_{turbulent,L} \quad (8)$$

The term  $M_{LG}$  in the momentum equations represents interphase momentum transfer between the two phases.

### Closure Relationships

In order to solve Equations (1) to (8) for velocities, pressure, and volume fractions, we need additional equations that relate the interphase momentum transfer term  $M_{LG}$  and the turbulent viscosities to the mean flow variables.

The interphase momentum transfer term  $M_{LG}$  is basically interphase drag force per unit volume. With the gas as the dispersed phase, the equation for  $M_{LG}$  is [7]:

$$M_{LG} = \frac{3}{4} \frac{C_D}{d_B} r_G \rho_L |V_G - V_L| (V_G - V_L) \quad (9)$$

The interphase drag relation proposed by [8] was used. For the relation proposed by [8], the interphase momentum transfer term as a function of local variables and constant coefficients put in a form suitable for the CFD is:

$$M_{LG} = \frac{(r_G^{average})^2}{(1-r_G^{average})V_S^2} g(\rho_L - \rho_G)r_G r_L |V_G - V_L| (V_G - V_L) \quad (10)$$

For the average gas holdup fraction,  $r_G^{average}$ , the correlation of Bennett et al. [5] was used:

$$r_G^{average} = 1 - \exp \left[ -12.55 \left( V_S \sqrt{\frac{\rho_G}{\rho_L - \rho_G}} \right)^{0.91} \right] \quad (11)$$

For the liquid and gas phase turbulence viscosities, a homogeneous shear stress transport turbulence model was selected and used. For turbulence transfer, Sato enhanced eddy viscosity model was also selected and used.

## MODEL FLOW GEOMETRIES

The model sieve tray geometries were selected based on the work of Thomas. A round (or circular) and a rectangular cross-section sieve trays were modeled and simulated. This work studied the effect of tray geometry modeling. The geometry modeling issues investigated were whether to use one tray or two trays and whether to include or ignore the tray thickness. The study showed that unless two trays with tray thickness included are used, the CFD simulations will not predict the correct pressure drop. Inclusion of inlet down comer was also found to help convergence and hence was used. Of course, the right way is to use actual experimental sieve tray geometries and compare the results of experiments and CFD modeling and simulations, which is what is attempted in this work.

Details of the dimensions of the sieve trays are given in [4]. Just to give a view of the sizes of the trays, the circular one has a diameter of 0.8128 m and a tray spacing of 1.016 m while the rectangular one has an

overall length of 0.9144 m, a width of 0.3048 m, and a tray spacing of 0.6096 m. Dimensions not present in Thomas need to be given and they are as follows. The down comer clearance height was set using the recommendations and relations found in Lieberman, N.P et al., and a down comer clearance of 63.5 mm was used for both the circular and rectangular cross-section sieve trays. For both trays, liquid (water) entrances are at the top of the tray horizontally in the negative x-axis direction 0.0762 m (equal to weir height) above the gas outlet holes plane. The heights of the liquid entrance used were 0.03 m for the circular sieve tray and 0.043175 m for the rectangular sieve tray. Liquid weir crest height relation found in Towler, G. was used for setting the heights of the liquid entrances.

For the circular cross-section sieve tray, symmetry was assumed about the centerline geometrical symmetry vertical plane and only half of the tray was considered so as to reduce computational load. For the rectangular cross-section sieve tray, the full tray was considered since it was possible to do so from computational load view point. For both shapes of trays, actual number and shape of holes were modeled since that was manageable. The whole tray spacing was considered in the simulation, even though the primary focus is in the froth region. This resulted in better numerical convergence, as well as provided with the ability to calculate tray pressure drops. The model sieve tray geometries and boundaries are shown in Figures 1 and 2.

## MODEL BOUNDARY CONDITIONS

To solve the continuity and momentum equations, appropriate boundary conditions must be specified at all external boundaries plus at any specific internal boundaries of the flow geometry.

Boundary conditions were specified in line with that used in Gesit, G [12].

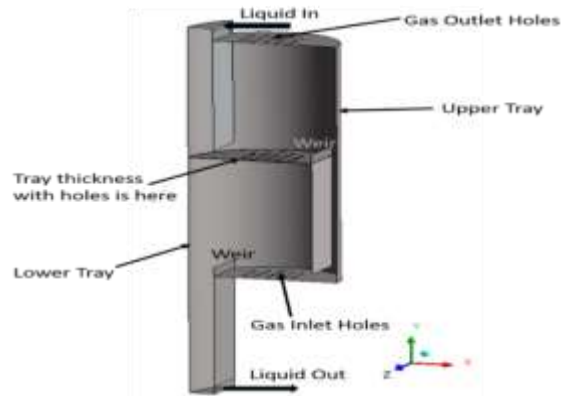


Figure 1 Model geometry and boundaries of the circular cross-section sieve tray (the plane of symmetry is just the whole front face of geometry shown, towards +z direction shown)

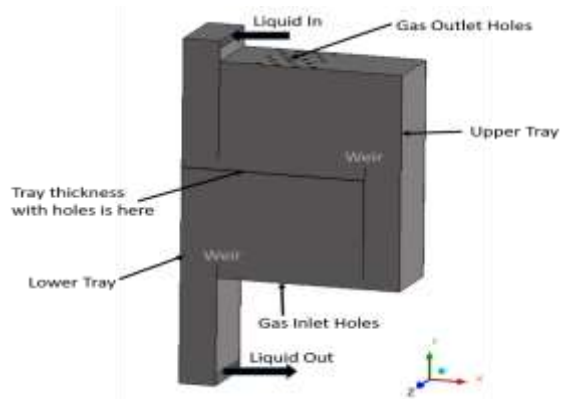


Figure 2 Model geometry and boundaries of the rectangular cross-section sieve tray (internal features are not visible and shown)

### Liquid Inlet

For all simulations, uniform or flat inlet liquid velocity profile was specified. The liquid volume fraction at the liquid inlet was taken to be unity assuming that only liquid enters through the down comer clearance.

### Gas Inlet

Uniform gas bubbling was used. The gas volume fraction at the inlet holes was specified to be unity.

### Liquid and Gas Outlets

The liquid and gas outlet boundaries were specified as outlet boundaries with velocity specifications. At the liquid outlet, only liquid was assumed to leave the flow geometry and only gas was assumed to exit through the gas outlet. These specifications will be in agreement with the specifications at the gas inlet and liquid inlet where only one fluid phase was assumed to enter.

### Wall and Symmetry Boundaries

The no-slip wall boundary condition was used for both the gas and liquid phases. The symmetry plane was specified as a symmetry boundary.

### Operating conditions and system properties

Steady state CFD simulations were conducted for all modeling and simulations. The fluid system and operating conditions were based on the work of Thomas, so that comparisons could be made. The fluid system is air-water with both fluids and tray operation at 1 atmosphere pressure and room temperature (25 °C).

### Mesh, mesh convergence and solution algorithms

Analysis Meshing 17.0 was used where default meshing method was used (which is Automatic: Patch Conforming/Sweeping), Physics was set to CFD and the Solver Preference was set to CFX. The number of nodes of the mesh has been given below. The meshing technology used is acceptable and the mesher tells if there is any unacceptable mesh statistics and if there is any mesh problem. For the meshes used here, the mesher didn't report any mesh

problem and it also didn't report any unacceptable mesh statistics. Knowing the mesher used and the number of nodes, one can get the mesh statistics from the meshing software.

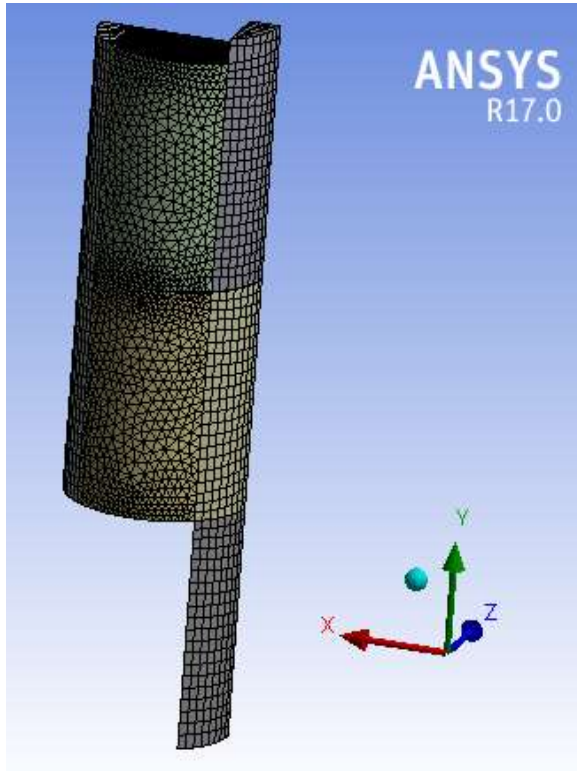


Figure 3 Mesh of circular cross-section sieve tray model geometry

The size of the mesh will have effect on the simulation results. Mesh size convergence study was conducted for the circular sieve tray. For the circular tray, above about 107087 nodes, the mesh size was found to have little effect on the simulation results and 107087 nodes mesh was selected as the working mesh. The rectangular sieve tray mesh was set at about the same mesh size of the circular one and 103819 nodes of mesh was selected as the working mesh. Table 1 gives the mesh convergence study CFD simulation results for the circular tray while Figures 3 and 4 show the meshed circular and rectangular sieve trays.

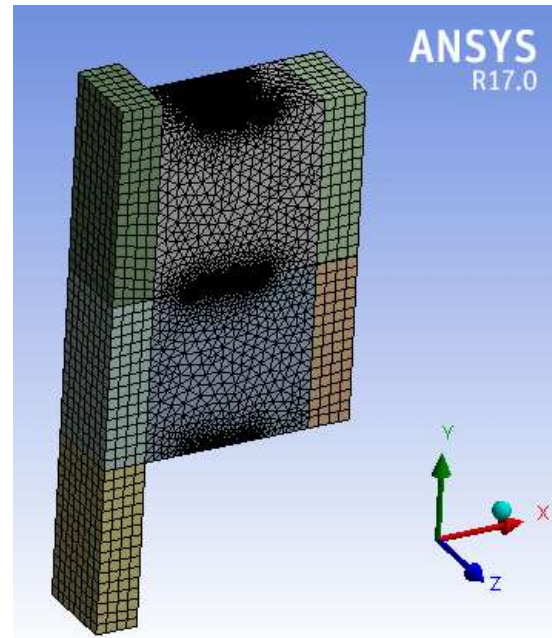


Figure 4 Mesh of rectangular cross-section sieve tray model geometry

Table 1 Mesh convergence study for the circular cross-section sieve tray (water flow rate =  $2.27 \times 10^{-3} \text{ m}^3/\text{s}$ , air hole velocity = 14.78 m/s).

Number of Nodes of Mesh	Total Pressure Drop by CFD [Pa]
84265	691.359
107087	865.391
130300	869.727

High Resolution differencing scheme was used for all the equations. Convergence criteria of  $\text{RMS} = 10^{-5}$  was used for all simulations (default convergence criteria is  $\text{RMS} = 10^{-4}$ )

One peculiar solution algorithm that needs to be mentioned is that volume fraction coupling was selected and initial volume fraction smoothing was set to volume-weighted and these resulted in better and faster convergence. All other algorithms are

obvious from the models used here and elsewhere and while all others are default ones and need no mentioning.

### **Simulation Results**

The ability of the CFD model and simulations to model, simulates, and predicts sieve tray pressure drop behaviour has been checked by calculating sieve tray pressure drop from the pressure solution field. The CFD model predicted total and dry sieve tray pressure drops are compared with the experimental results of Thomas, W.J and the results are presented in this section. The pressure drop was calculated from the pressure solution field as the area average of absolute pressure at the holes inlet at the bottom of the tray thickness (located at the middle in Figures 1 and 2) minus the area average of absolute pressure at the holes outlet at the top of the tray.

As shown in the graphs in this section, the CFD simulation results are in acceptable and good agreement with the experimental results of Thomas, W.J. The CFD model performance is acceptably good. Besides, the results of the CFD simulations exhibit the correct trend with respect to gas and liquid flow rates; i.e., the CFD simulation results correctly predict that pressure drop increases with either gas or liquid flow rate.

### **Results for the Circular (or Round) Sieve Tray**

The total and dry sieve tray pressure drops of the CFD simulations results for the circular tray are shown in Figures 5 to 6. Figure 5 shows the total sieve tray pressure drop CFD simulation results whereas Figure 6 shows the dry sieve tray pressure drop

CFD simulation results. Also shown and given in all Figures are the experimental results of Thomas, W.J

As shown in Figure 5, the CFD simulation results for the circular sieve tray total pressure drop are in acceptable and good agreement with the experimental results of Thomas, W.J. This good agreement implies that the CFD model provided by this work performed and worked well. The good agreement and good performance of the CFD model provided may be ascribed to the fact that the CFD model involves several aspects of mechanistic modeling. The fact that the CFD model is mechanistic and worked well makes it more reliable than empirical correlations. It can be stated that for all cases (both circular and rectangular trays) the CFD model performance is acceptably good

As shown in Figure 6, is shown the dry sieve tray pressure drop prediction of the CFD model compared with the experimental results of Thomas, W.J. The agreement between the CFD model results and the experiments can be stated as acceptably good. For the dry case, we have a single phase fluid flow (here only flow of air). Again, the CFD model involves several aspects of mechanistic modeling and works for the single phase flow too, and is hence more reliable than correlations.

### **Results for the Rectangular Sieve Tray**

The total and dry sieve tray pressure drops results of the CFD simulations for the rectangular tray are shown in Figures 7 to 8. Figure 7 shows the total sieve tray pressure

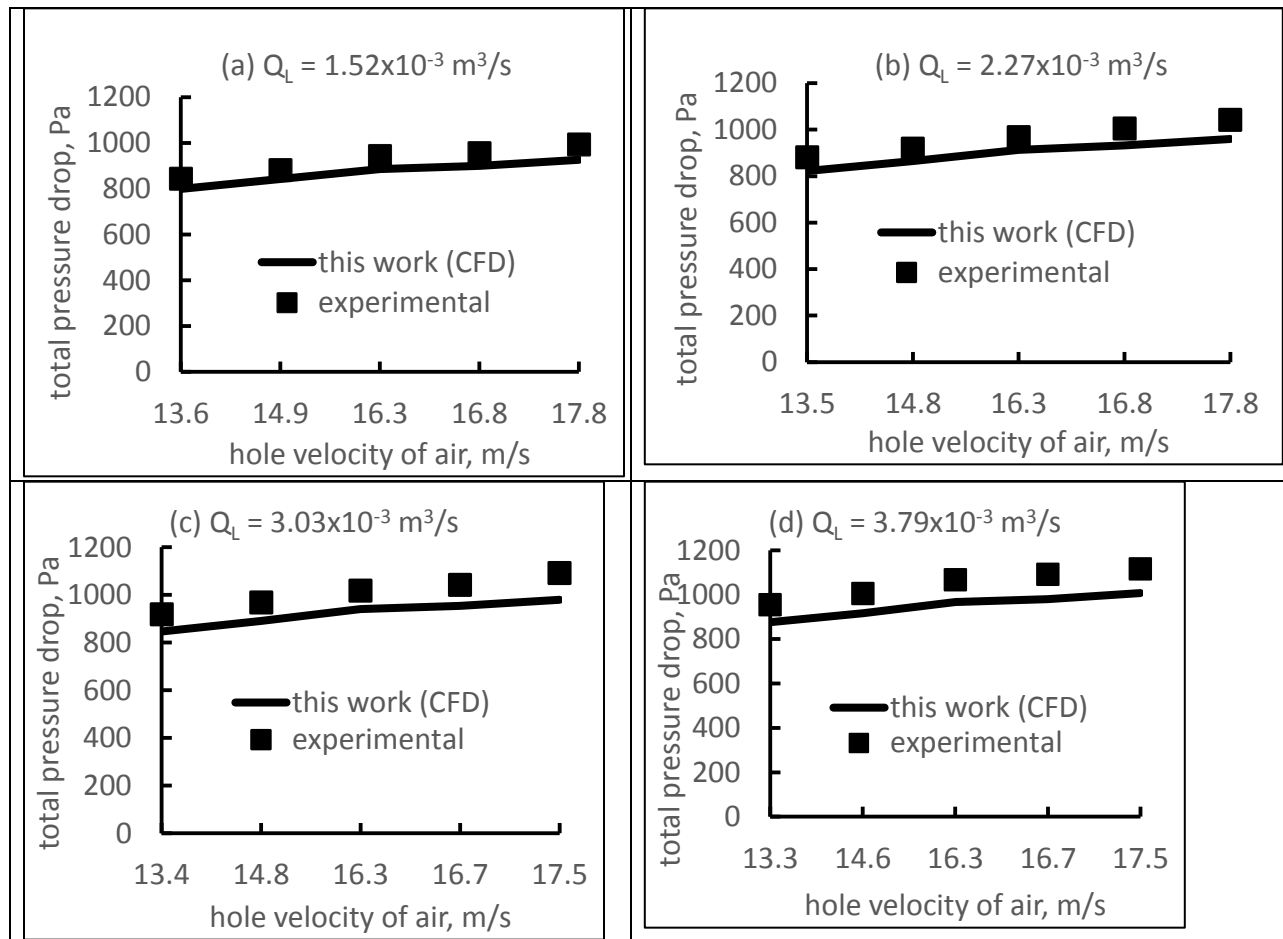


Figure 5 Total pressure drop of circular cross-section sieve tray

Drop CFD simulation results whereas Figure 8 shows the dry sieve tray pressure drop CFD simulation results. Also shown and given in all Figures are the experimental results of Thomas, W. J .

As shown in Figure 7, the CFD simulation results for the rectangular sieve tray total pressure drop are unacceptable and good agreement with the experimental results of Thomas, W. J For the rectangular sieve tray too, the CFD model has several mechanistic aspects of modeling and acceptably and reliably captured the flow behaviour and is hence more reliable than correlations.

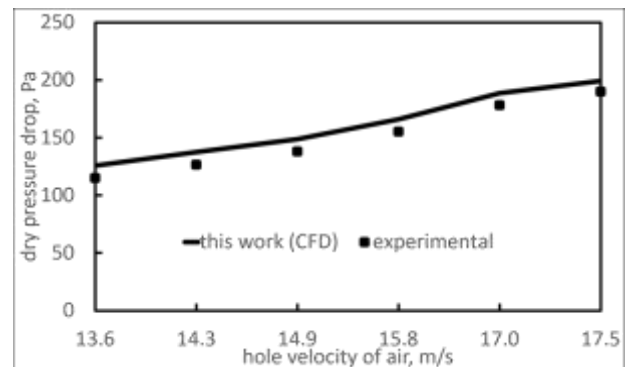


Figure 6 Dry pressure drop of circular cross-section sieve tray

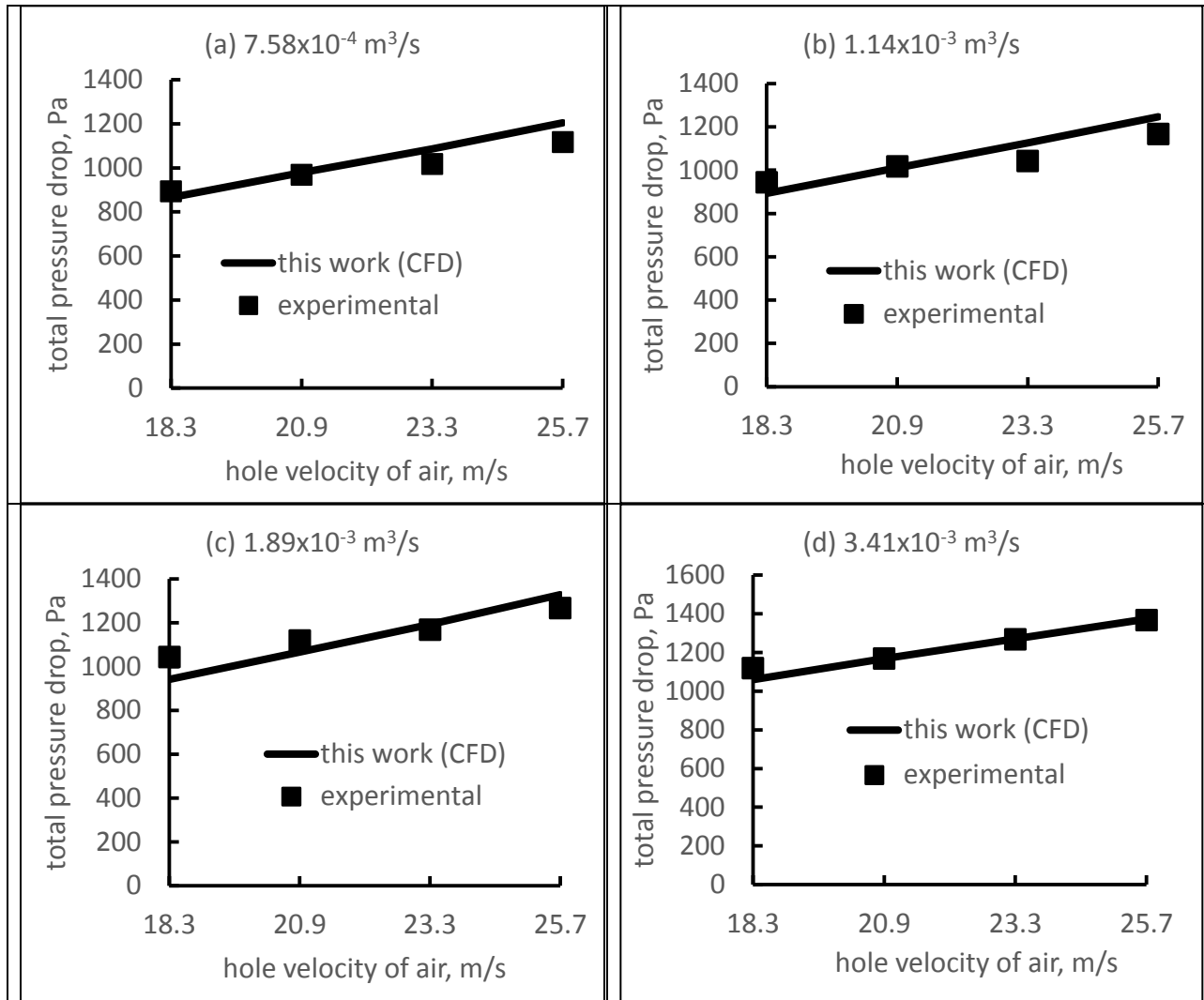


Figure 7 Total pressure drop of rectangular cross-section sieve tray

Figure 8 shows the dry pressure drop CFD model simulation results for the rectangular tray. It can be seen that the CFD model simulation results under predicted the dry pressure drop particularly at high gas rates.

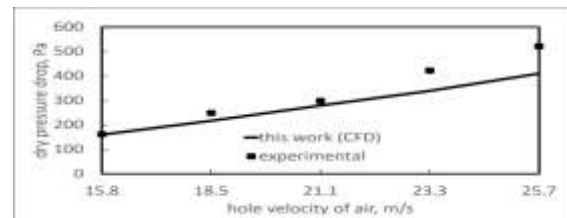


Figure 8 Dry pressure drop of rectangular cross-section sieve tray

The reason for this was found to be that some fraction of the gas bypassed the holes by going up through the lower down comer clearance. What is meant by this is depicted and explained by the gas streamlines shown in Figure 9 for the dry gas flow.

But the gas streamlines of Figure 10, which are for the two phase flow case, show that there is little or no gas bypassing when two phase flow. The streamlines show the path followed by the gas.

A solution to this problem of gas bypassing holes is to use a model geometry that has gas inlet located above the lower down comer clearance. This will make all the gas pass through the holes.

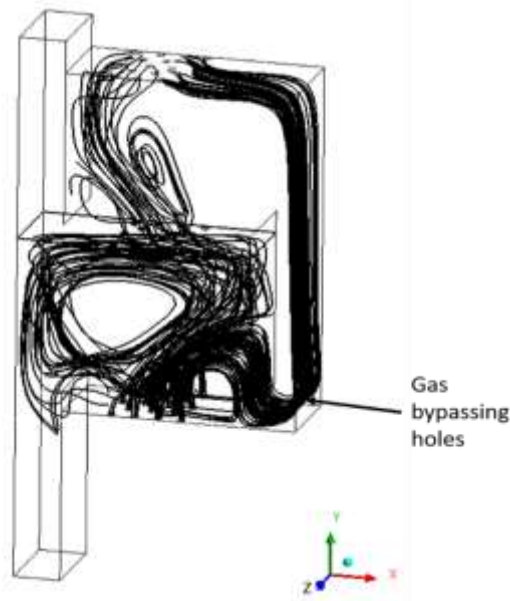


Figure 9 Gas streamlines (in dark black) of the single phase (dry gas) flow (air hole velocity = 25.7 m/s, rectangular tray)

### CONCLUSIONS

This work provided validated model for modeling and simulating and predicting the pressure drop of sieve trays by means of computational fluid dynamics (CFD) using steady state simulations. The flow inside the tray was modeled as a three-dimensional two-phase flow of gas and liquid in the Eulerian-Eulerian framework. The time and volume averaged continuity and momentum transfer equations were numerically solved using the commercial package CFX 17.0 of ANSYS. The gas and liquid phase equations were coupled through appropriate interphase

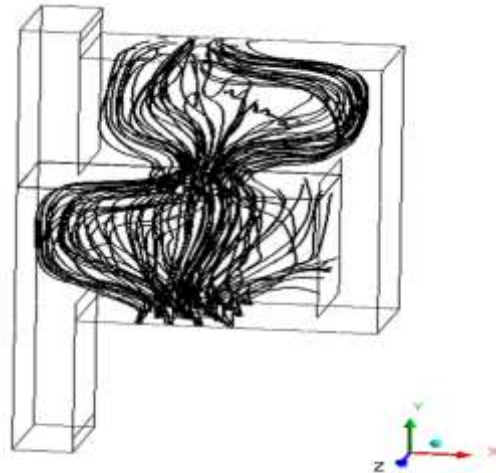


Figure 10 Gas streamlines (in dark black) of the two phase flow (water flow rate =  $3.41 \times 10^{-3} \text{ m}^3/\text{s}$ , air hole velocity = 25.7 m/s, rectangular tray)

Momentum transfer closure model. Appropriate working CFD flow geometry model was also identified and provided. The CFD model was used to predict total and dry tray pressure drops. The CFD simulation results are in acceptable and good agreement with experimental results.

So far, only empirical correlations have been used to estimate sieve tray pressure drop. However, the correlations are not based on actual mechanics of flow but are based on gross oversimplifications and empirical correlations—hence often have large errors and are not reliable. Therefore, so far methods for satisfactorily modeling and predicting sieve tray pressure drop are lacking. This work showed that the CFD model provided here can be used as an acceptably good and a powerful tool and method for modeling and predicting sieve tray hydrodynamics and calculating tray pressure drop.

Compared to existing methods, the CFD model provides and adds appreciable good, significant, and advanced improvements and performance for sieve tray pressure drop determination. On top of being mechanistic, the modeling using CFD offers several advantages. For example, it overcomes many of the limitations associated with experiments and correlations and offers ease of changing tray geometry and operating conditions without incurring appreciable cost of time and other resources. From the results and the CFD model performance, it is concluded that the CFD model provided here is acceptably good for sieve tray pressure drop modeling and simulation and hence is acceptably good for tray design and analysis.

### Nomenclature

$C_D$  drag coefficient  
 $d_B$  bubble diameter [m]  
 $g$  gravitational acceleration vector [ $m\ s^{-2}$ ]  
 $g$  gravitational acceleration [ $m\ s^{-2}$ ]  
 $\mathbf{M}_{LG}$  Interphase momentum transfer vector [ $kg\ m^{-2}\ s^{-2}$ ]  
 $p_G$  gas phase pressure [ $N\ m^{-2}$ ]  
 $p_L$  liquid phase pressure [ $N\ m^{-2}$ ]  
 $Q_L$  liquid volumetric flow rate [ $m^3/s$ ]  
 $r_G$  gas (or vapour) phase volume fraction  
 $r_G^{average}$  average gas holdup fraction in froth  
 $r_L$  liquid phase volume fraction  
 $V_G$  gas phase velocity vector [m/s]  
 $V_L$  liquid phase velocity vector [m/s]  
 $V_S$  gas phase superficial velocity based on bubbling area [m/s]

### Greek Letters

$\mu_{laminar,G}$  molecular viscosity of gas [ $kg\ m^{-1}\ s^{-1}$ ]  
 $\mu_{laminar,L}$  molecular viscosity of liquid [ $kg\ m^{-1}\ s^{-1}$ ]

$\mu_{turbulent,G}$  turbulent viscosity of gas [ $kg\ m^{-1}\ s^{-1}$ ]  
 $\mu_{turbulent,L}$  turbulent viscosity of liquid [ $kg\ m^{-1}\ s^{-1}$ ]  
 $\rho_G$  gas phase mass density [ $kg/m^3$ ]  
 $\rho_L$  liquid phase mass density [ $kg/m^3$ ]

### REFERENCES

- [1] Noriler, D., Barros, A.A.C., Maciel, .R.W., and Meier, H.F., “*Simultaneous Momentum, Mass, and Energy Transfer Analysis of a Distillation Sieve Tray using CFD Techniques: Prediction of Efficiencies*”, Ind. Eng. Chem. Res., Vol. 49, 2010, pp. 6599–6611.
- [2] Zarei, A., Hosseini, S.H., and Rahimi, R., “*CFD and experimental studies of liquid weeping in the circular sieve tray columns*”, Chemical Engineering Research and Design, Vol. 91, No. 12, 2013, pp. 2333-2345.
- [3] Zarei, A., Hosseini, S.H., and Rahimi, R., “*CFD study of weeping rate in the rectangular sieve tray columns*”, Journal of the Taiwan Institute of Chemical Engineers, Vol. 44, 2013, pp. 27-33.
- [4] Thomas, W.J. and Ogboja, O., “*Hydraulic Studies in Sieve Tray Columns*”, Ind. Eng. Chem. Process Des. Dev., Vol. 17, No. 4, 1978, pp. 429-443.
- [5] Bennett, D. L., Agrawal, R. and Cook, P. J., “*New Pressure Drop Correlation for Sieve Tray Distillation Columns*”, AIChE Journal, Vol. 29, 1983, pp. 434-442.

- [6] Bennett, D.L., Watson, D.N. and Wiescinski, M.A., “*New Correlation for Sieve-Tray Point Efficiency, Entrainment, and Section Efficiency*”, *AIChE Journal*, Vol. 43, No. 6, 1997, pp. 1611-1626.
- [7] *ANSYS CFX 17.0 Documentation*, ANSYS Inc.
- [8] Van Baten, J. M. and Krishna, R., “*Modelling Sieve Tray Hydraulics using Computational Fluid Dynamics*”, *Chemical Engineering Journal*, Vol. 77, No. 3, 2000, pp. 143-151.
- [9] Lieberman, N.P., and Lieberman, E.T., “*A Working Guide to Process Equipment*”, McGraw-Hill, 4<sup>th</sup> Edition, 2014.
- [10] Towler, G., and Sinnott, R.K., “*Chemical Engineering Design: Principles, Practice and Economics of Plant and Process Design*”, Elsevier Ltd., 2<sup>nd</sup> Edition, 2013.
- [11] Kister, H. Z., “*Distillation Design*”, McGraw-Hill, 1992.
- [12] Gesit, G., Nandakumar, K. and Chuang, K. T., “*CFD Modeling of Flow Patterns and Hydraulics of Commercial-Scale Sieve Trays*”, *AIChE Journal*, Vol. 49, No. 4, 2003, pp. 910-924.

# PRACTICAL CONSIDERATIONS FOR DIMINISHING PILED RAFTS ON WEAK LAYERED SOILS

Henok Fikre

School of Civil and Environmental Engineering  
Addis Ababa Institute of Technology, Addis Ababa University  
E-mail:henok.fikre@aait.edu.et

## ABSTRACT

*Alluvial deposits are abundant in the world especially in coastal areas. Due to their young geological formation, very stiff strata are not normally obtained even at great depth, which maximizes the cost of conventional foundation variants for heavy weight structures. This paper presents basic considerations for optimized design of foundations of high-rise buildings on alluvial soils of the West African coastal city of Lagos by using piled rafts. Soil parameters have been determined from interpretation of extensive soil data from test records of different high-rise building projects within the area and back analysis of static pile load test results. Effects of raft thickness, pile length and spacing on the load-settlement behaviour of piled rafts were studied by employing three-dimensional non-linear Finite-Element Analysis. Normalized curves for practical loads in the area were produced to enhance design of piled rafts for similar conditions. The extensive parametric studies with uniform length piles and uniformly distributed external loads indicated the advantage of having widely spaced piles for reducing the foundation costs. Analysis results of a specific high-rise building in Lagos were found to be in good agreement with the findings of the parametric studies and previous researches with comparable input parameters.*

**Keywords:** Piled rafts, back-analysis, weak layered soils, non-linear, 3D Finite Element Analysis

## INTRODUCTION

Piled raft is a hybrid foundation system which accounts for the load share of rafts resting on group of piles, which is traditionally ignored in the conventional pile design methods irrespective of the existing interactions between the piles, raft and soil layers. Due to its economic significance, wide ranges of application have been exercised in the last four decades for different soil conditions [1, 2, 3]. Much has not been reported about its suitability on alluvial deposits around coastal areas of younger geological ages [4]. This research has been motivated from the observations of the actual design and construction practice related to structures on such deposits.

Due to the relatively weak subsoil formation in the development-oriented megacity of Lagos [5], it is customary to use very long piles for the foundations of these high-rise buildings to achieve the required capacity to withstand the super-structural loads and the associated settlements [6].

The introduction of this hybrid foundation system of piled raft not only provides economic benefits, but also favours the enhancement of the construction industry by solving the practical difficulties of using very long piles with the introduction of shorter piles to reduce the settlement of the raft which can share a certain portion of the total super-structural load acting on the foundation [7].

The research was carried out by analysing the ground condition in the selected area and preparing the material parameters required for the numerical analysis which employed the commercial Finite Element software package ABAQUS. While an axisymmetric simulation was used to calibrate the parameters from pile load test results with appropriate constitutive model, three-dimensional non-linear analysis was employed for modelling the behaviour of the piled raft foundation system. The load share of the foundation elements and settlement reduction has been studied by varying the length of piles configured in simple and practical arrangements. Pile length staggering is beyond the scope of this research and the load is assumed to be uniformly distributed.

### Load -Settlement Behaviours

#### Resistance of the components

Being a composite foundation system constituting the piles, the raft and surrounding soil, quantifying about the interactions between these components of a piled raft foundation is the basis for its behaviour [8]. The bearing capacity of a piled raft is thus a function of the interactions between these components. By considering the characteristic loads, subscripted as  $k$  in the following equations, the settlement dependent total resistance of the foundation unit,  $R_{tot,k}(s)$  is the sum of the resistances of all individual piles  $R_{pile,k,j}(s)$  and the raft  $R_{Raft,k}(s)$ , or equivalently:

$$R_{tot,k}(s) = \sum_{j=1}^m R_{pile,k,j}(s) + R_{Raft,k}(s) \quad (1)$$

The resistance of the individual piles is computed as the sum of the base and skin friction resistances:

$$R_{pile,k,j}(s) = R_{b,k,j}(s) + R_{s,k,j}(s) \quad (2)$$

The resistance of the raft can be determined by integrating the stress under the raft  $\sigma(x, y)$  over the (raft-soil) contact area:

$$R_{Raft,k}(s) = \iint \sigma(x, y) dx dy \quad (3)$$

The total external load  $F_{tot,k}$  is carried partly by the piles and partly by the contact pressure between the raft and the soil. The proportion of the load carried by the piles is usually expressed using the pile - raft coefficient,  $\alpha_{pr}$ , which is defined as:

$$\alpha_{pr} = \frac{\sum_{j=1}^m R_{pile,k,j}(s)}{R_{tot,k}(s)} \quad (4)$$

The value of pile – raftco efficient depends fully on the allowable settlement. If there is a stringent requirement to limit the settlement within a certain prescribed range, then higher number of piles or longer piles can be used leading to a higher value of the pile-raft coefficient, and vice versa. This can be explained better with the relationship between the pile - raft coefficient and the normalized settlement, defined as the ratio of the settlement of piled raft to that of unpiled raft,  $\xi_s$ , shown in Fig. 1, which has been derived from practical cases recorded in the past.

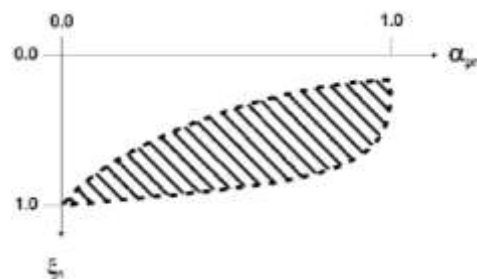


Fig. 1 Relationship between normalized settlement and pile-raft coefficient [4]

**Safety provisions of piled rafts**

$$R_{tot,k} \geq F_{c,k} \cdot \gamma_F \cdot \gamma_R \tag{5}$$

Various research works have been carried out to assess the bearing capacity of piled rafts using theoretical, experimental and numerical tools in different parts of the world [9, 10, 11]. Katzenbach et al. [12] proposed a piled raft design concept based on the provisions of [13]. The overall resistance of piled rafts in ultimate limit state (ULS)  $R_{tot,k}$  is defined as the point at which the increase in settlement becomes significantly super-proportional, analogous to single pile resistance, as presented in Fig. 2a. However in most cases of piled rafts the variation of settlements with the resistance is of the form shown in Fig 2b, where a gradual variation of the resistance with settlement is observed. This is due to the enhanced bearing resistance of piled rafts due to favourable interactions within the components. Thus a minimum resistance  $min R_{tot,k}$  shall be set in such a way that failure of the foundation can be adequately avoided. In both cases the overall resistance shall be greater than the sum of the applied characteristic load  $F_{c,k}$ , multiplied by the partial safety factors for the load ( $\gamma_F$ ) and the resistance ( $\gamma_R$ ).

The use of a partial safety factor of unity for the resistance and two for the characteristic load as suggested in [14] is equivalent to the customary method of applying a single global safety factor of 2. The guideline compiled by Katzenbach and Choudory [15] defines the safety concept both for the ultimate and serviceability limit states by applying appropriate partial safety factors for individual components in the respective cases.

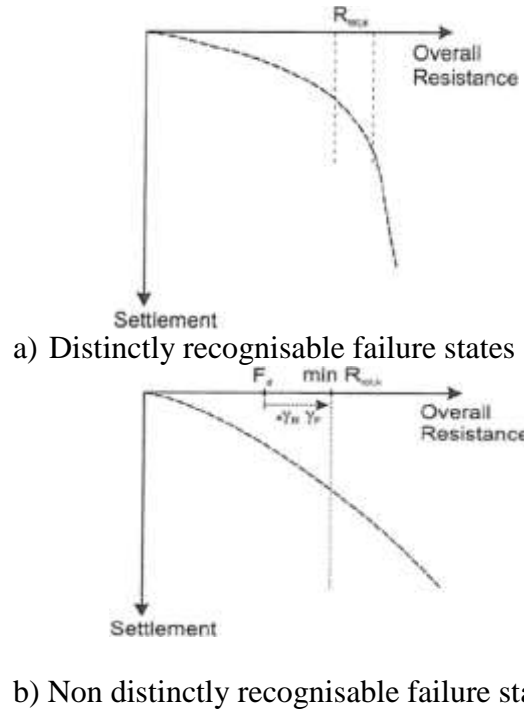


Fig. 2 Non-linear system behaviour of a piled raft and determination of the overall resistance [12]

**Study Area**

The area under investigation lies within the alluvial deposits of South-West Nigeria Basin which is an integral part of Dahomeyan Embayment, which lies to the east of the Dahomey Republic and to the north of the Bight of Benin [16, 17]. The local formation consists of sedimentary deposits of silts sands and clays underlain by recent deposits which vary from the littoral and lagoon sediments to the coastal belt and alluvial deposits of the major rivers [18]. A continuously shifting sedimentation of the clay and sand sediments was also reported by [19, 20].

The engineering soil properties in the study area have been evaluated from extensive field and laboratory investigation results of different high-rise building projects in Victoria Island, which is located in the southern part of Lagos city [4]. Field investigation included more than 19 boreholes with standard penetration tests (SPT) and 47 cone penetration tests (CPT) up to a maximum depth of 63 m. The water table was found within a depth of 3.5 m from the ground surface, and all further computations in this research were carried out by assuming the whole soil to be submerged in water. Based on interpretation of these field investigation results, the multi-layered soil has been idealized to consist of our soil layers as shown in Table 1. Soil parameters for the

computational models have not been taken simply from the laboratory test results, due to the reason that laboratory results are generally extremely conservative [21]. Constrained moduli of the soils have thus been determined by employing empirical correlations with the SPT and CPT values in addition to the laboratory Oedometer test results, to account for the in-situ conditions. The basic soil parameters summarized in Table 1 are thus obtained by combining the measured values from laboratories with those correlated based on extensive field investigation results. These basic parameters have further been calibrated using the pile load test simulations discussed in the next section.

Table 1. Summary of soil parameters determined from field and laboratory investigation results.

Depth [m]	0 – 10	10 – 20	20 – 40	40 – 63
Soil layer	Loose sand (SAND1)	Medium dense sand (SAND2)	(Firm clay CLAY)	Dense sand (SAND3)
Standard penetration test N ranges	1- 12	11-22	-	12-57
Cone penetration $q_c$ ranges	0.2-7	0.5-40	0.5-35	-
Young's modullus of Elasticity $E$ [MN/m <sup>2</sup> ]	18 - 24	26-41	5-33	45-70
Effective unit weight $\gamma'$ [kN/m <sup>3</sup> ]	8.0	8.5	8.0	10.0
Effective angle of friction $\phi'$ [°]	29.0	32.2	22.6	34.0
Cohesion $c'$ [kN/m <sup>2</sup> ]	-	-	29.2	-
Poison's Ratio $\nu$ [-]	0.3	0.3	0.4	0.3
Static Earth pressure coeff. $K_0$ [-]	0.52	0.47	0.54	0.44

### Calibration of Materials Parameters from Pile Load Test

Since the use of soil parameters representing the in-situ conditions is a key requirement for simulating the real problems, pile test results are recommended for high-rise buildings categorized into the Geotechnical Category GC 3 of the Eurocode EC 7 [13,

15]. Accordingly pile load tests performed within the study area have been used to calibrate the soil parameters based on in-situ conditions.

A working pile of 47 m length and 800 mm diameter, loaded up to a maximum of 6 MN and a corresponding settlement of 8 mm, has been used to investigate its load - settlement

behaviour. Since the pile load test was not carried out till failure as shown in Fig. 3, the back analysis has mainly been based on comparison of the initial part of the test result. The axis-symmetric Finite Element analysis using the commercial software ABAQUS considered the cap plasticity constitutive model for the soil and elastic behaviour for the pile. Since the major

parameter affecting the load-settlement behaviour is the stiffness of the soil layers, as proven by preliminary sensitivity analysis, different calculation variants were carried out by varying the elasticity modulus of successive layers from the range of values in Table 2. Results of selected computation variants only have been presented in Fig. 3.

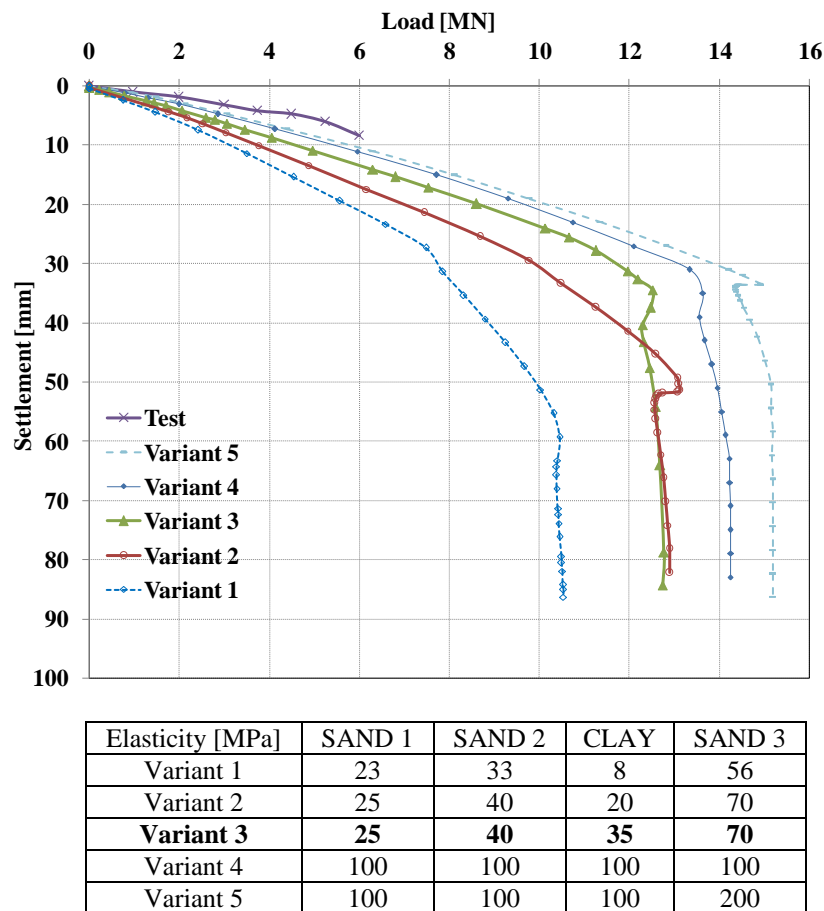


Fig. 3 Calibration of representative static pile-load test using FEM

The results of Variant 1, where the stiffnesses of the soil layers were taken as the arithmetic mean of the corresponding layers (Table 1), deviated noticeably from the pile - load test results. Since the test results were found to be about three times stiffer than the simulated results, which is actually in agreement with findings of previous

researches [21], the other variants were performed by considering the upper ranges of the soil layer stiffnesses. Variant 3 was performed by considering the values from the upper limit of the range of elasticity shown in Table 1, while variant 2 is used to show the influence of the soil layer where the pile tip rests. Variants 4 and 5 were

performed by stiffening all the soil layers beyond the aforementioned ranges of parameters with the aim of approaching the measured values. Since stiffening the soil layers to as much as 4 times the mean value of Variant 1, the required calibration could not have been achieved. Thus Variant 3, which considers the maximum range of elasticities from the mean values and whose results plot mid-way between the results of the test and the FE simulation with that of Variant 1, has been chosen for the remaining research works.

### Settlement and Load Sharing Behavior of Piled Rafts on Weak Ground

Application of piled rafts for the ground condition calibrated earlier have been investigated after rigorous parametric studies by varying selected geometric parameters of the foundation units with the location of the pile tip in the various soil layers. The pile diameter of 1 m was held constant in all the variant computations. After preliminary analysis of using various pile configurations, two pile spacing, namely three and six times the diameter of the pile, 3D and 6D, respectively, were considered for further analyses, which allow the group effect of piles without exaggerated difference between the pile loads, except edge piles of the closely spaced arrangement. This is in line with the recommended range of application of piled rafts [22, 23]. For the configurations of pile presented in Fig. 4, three raft thicknesses (0.5 m, 1.5 m and 2.5 m) were considered, for each of which the pile length was varied between 5 m and 50 m and the raft edge distance was taken as three times the pile diameter, which is known as the simple case [22].

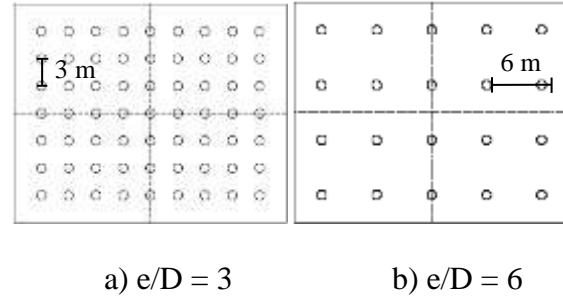


Fig. 4 Pile spacing used for the study

In the 3D-FE computations the successive evolution of the load history has been modeled starting from an initial state in which the primary stresses act on the soil continuum and no construction phases begin. Subsequently installation of the piles follows by removing soil and adding concrete elements as well as excavation of the soil above the raft level by removing the soil within the location of the pit. The raft was then introduced into the foundation system by activating its weight  $G_{Raft}$ , as uniformly distributed load over the surface, its stiffness being activated in the subsequent step.

Finally, the super-structural load was gradually added over the surface of the raft till its maximum value. Soil profiles together with their corresponding parameters and constitutive models were adopted from the calibration of the pile-load test.

The major findings of these computations, for a uniformly distributed load of 462 kN/m<sup>2</sup>, which has been taken from practical loading conditions of high-rise building projects in the area [4], are summarized in Fig. 5 and 6, using plots of normalized settlement  $\varepsilon_s$  and pile-raft coefficient  $\alpha_{pr}$  respectively, as a function of the pile length  $L_p$ .

## Practical Consideration for Diminishing Piled Rafts on Weak Layered Soils

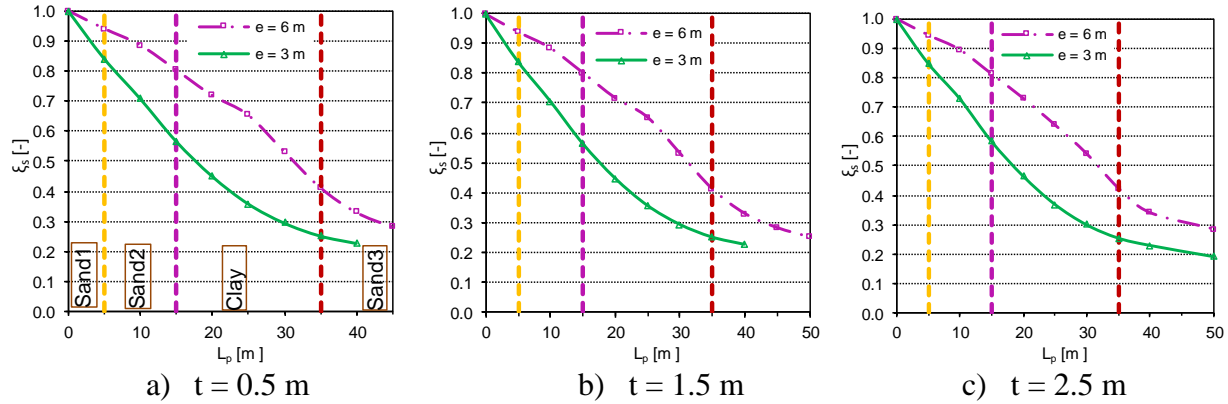


Fig. 5 Variations of the normalized settlement with geometric parameters of the piles and raft.

The settlement reduction curves show no sudden bend or break at the successive soil layer interfaces except that at the bottom SAND3 layer. Placing the pile tips at this bottom layer, which is twice as stiff as the overlying CLAY layer resulted in very much limited or insignificant reduction instead of further settlement reduction. It is however evident from Fig. 5 that the normalized settlement is found to be affected more significantly by the geometric parameters of the piles. For all the three cases of raft thickness, a limiting pile length is observed, beyond which further pile length increment

will not produce settlement reduction, irrespective of the pile spacing. Thus, the wider spacing remains to be economical above the limiting length as far as settlement reduction is concerned. The advantages of the closer spacing in reducing the settlements can only be appreciated when the pile length is well below the limiting length especially with flexible raft. The maximum difference between the two spacings is actually observed at intermediate depth (about 10 – 30 m in this case), though it calls for further investigations in order to determine the optimum value.

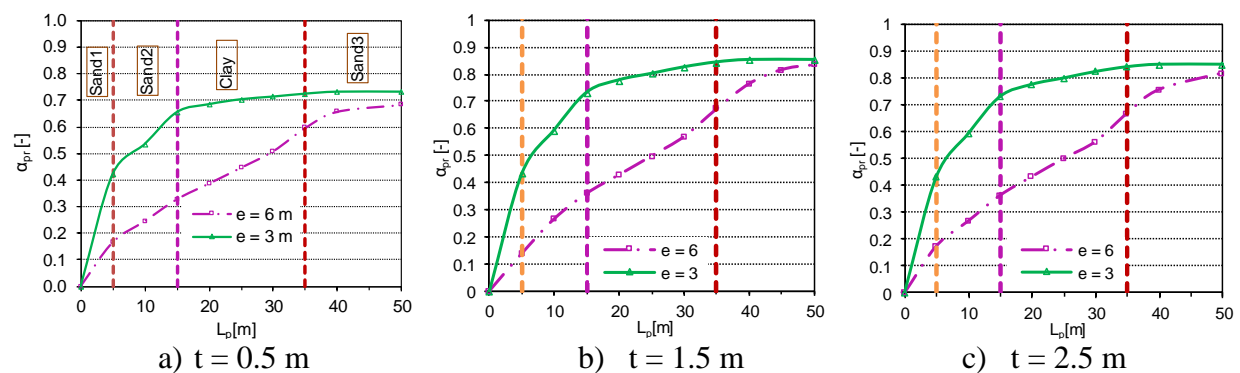


Fig. 6 Variations of the pile raft coefficient with geometric parameters of the piles and raft.

The dominant factors affecting the pile - raft coefficient are pile spacing and length, in a similar fashion as that of the normalized settlement (Fig. 6). For the ground condition

under consideration, with no great variation of the soil stiffness till great depth, the change in layer stiffness of the soil layers as well as raft thickness do not substantially

influence the pile-raft coefficient. However, further detailed studies with regard to the effects of soil layering and raft thickness are recommended to come to confirmed conclusions.

The general tendency of reduction of the pile-raft coefficient with increasing pile spacing agrees with previous findings [23], as it might be expected. While the denser pile spacing doesn't favor the contribution of the raft on load sharing except for short piles (up to about 15 m), the raft shares considerable amount of the total load for wide range of investigated pile length (up to about 40 m) in the case of widely spaced piles. This is due to the enhanced pile-raft interaction by wider pile spacing except for exceptionally long piles. Thus, pile length increment has practically no significance on the load share of the foundation elements if excessively long piles are to be used. It is

also to be recalled that the use of very long piles with denser pile spacing can only lead to limited settlement reduction without even increasing the pile load share, which was the practice in the study area.

The above results motivate the use of the wider spacing in almost all cases, except for minimizing settlement while using piles of intermediate length. To assist the choice of a better arrangement of the piles to optimize the required outputs, the normalized settlement is plotted against the pile - raft coefficient for the range of raft thickness and pile spacings considered as shown in Fig. 7. The 'total pile meters',  $nL$ , calculated as the product of the uniform pile length and the number of piles, is used for a better comparison. Points of equal pile meter in the two configurations are joined using arrow lines in the plots to facilitate interpretation.

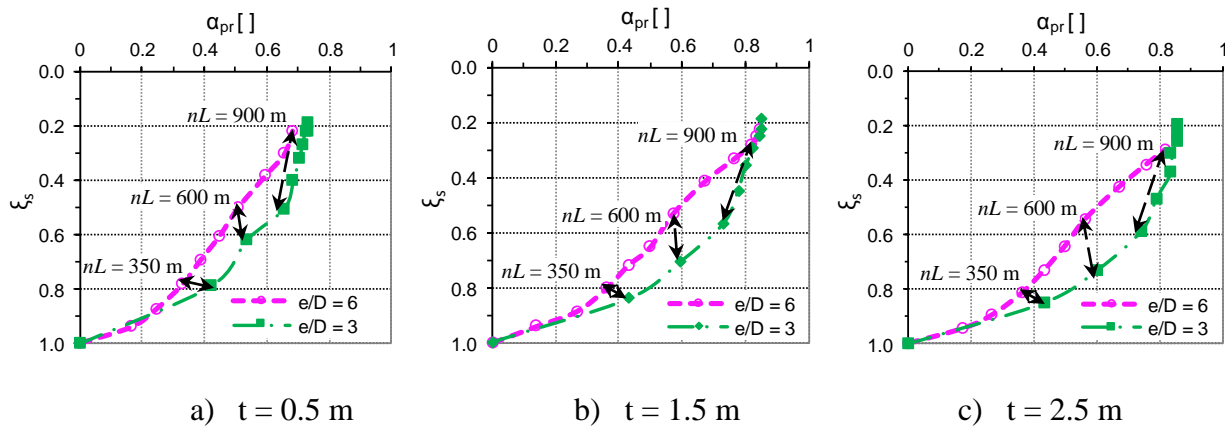


Fig. 7 Variation of the normalized settlement with pile-raft coefficient for different geometric conditions

In all the cases, the normalized settlement decreases while using the wider spacing although the difference will be exaggerated when total pile meters increases, due to enhanced stiffness of the ground. On the other hand, the pile raft coefficient remains fairly constant at intermediate pile meters (about  $nL = 600$  m), while the contribution of

the raft is enhanced by smaller pile meters for the wider spacing, and by higher pile meters at closer spacing, though the latter is not significant. For instance, the use of the very close spacing with very large pile meters could only help reduce the pile-raft coefficient by less than 10 % while

increasing the settlement as much as twice as that of the widely spaced configuration, which will not be practically desired.

While all the curves plot within the ranges of Fig. 1, indicating the possible applicability of piled rafts in the region, the use of flexible raft as in Fig 7a is characterized by somehow reduced pile - raft coefficient. Quantitative comparison of the results shows that the load share of flexible raft will be higher for both spacings of piles as illustrated in the works of [24] due to increased pile-raft interaction. On the other hand thickening the raft leads to widening the gap between the settlement reduction curves for the two pile spacings.

Widening the pile spacing and reducing the raft thickness contribute to the enhancement of the pile-raft interaction, by decreasing the pile-pile interaction, and hence increasing the load share of the raft. Doubling the pile spacing is thus generally found to enhance the performance of the piled raft, as both normalized parameters are reduced substantially in a very wide range of total pile meters.

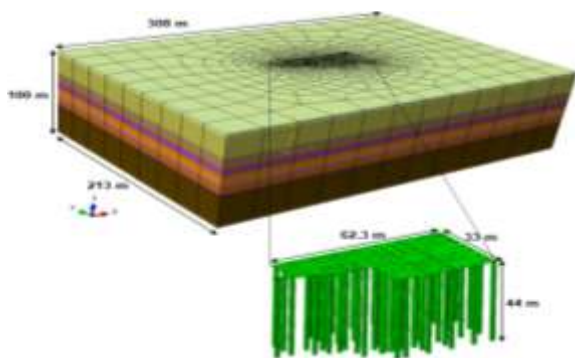


Fig. 7 Geometry of the basic numerical model

### Practical Case of Piled Rafts on Layered Deposits of Lagos

The practical applicability of piled rafts in the study area is illustrated by a 75 m high building project with similar loading and material parameters as the case indicated in the previous sections. Even if soil investigation results for the project indicated that the ground condition of the site were found to be similar to the case of the previous sections of this research, further considerations were also made, including Osterberg cell pile-load tests corresponding to the specific project. The calibration of the parameters using site specific soil investigation and back-analysis of the pile-load tests, which have also been reported by [22], were found to be in conformity with the results shown in Table 1.

A three-dimensional, non-linear analysis has been carried out for assessing the behavior of a piled raft foundation by incorporating the calibrated soil parameters, with due consideration of the irregular geometry of the raft and the different loads from the superstructure. The geometry of the model shown in Fig. 7 was used to idealize the soil continuum with the piled raft at the center. The FE-mesh used in the numerical analysis using the commercial software ABAQUS had 97,775 elements and 95,160 nodes. The stepwise calculation phases were similar to the model in the previous section, except the loading conditions, which were idealized as realistic as possible.

Loads on the foundation were determined based on structural calculations by considering dead and live loads, designated as  $G$  and  $Q$  respectively. Load combinations representing the serviceability limit states and ultimate limit states conditions mentioned earlier in Section 2.2 of this research.

Correspondingly full dead load and live load including the raft own weight,  $G_{\text{Raft}}$ , or  $G + G_{\text{Raft}} + Q$ , was used to represent the behavior at serviceability condition. The resistance at ultimate limit states was also determined using the load combination explained in Section 2.2 of this paper using a global safety factor of 2 suggested by [14].

Settlement prediction on the other hand, was carried out by considering the load combination called ‘settlement inducing load’ [25], which is defined as the sum of full dead load and one third of the live load ( $G + G_{\text{Raft}} + Q/3$ ).

After a series of calculations with different pile configurations, a variant with piles of 30 to 44 m long, arranged in such a way that the total load is fairly distributed among all the piles has been selected as the optimal arrangement.

The controlling parameter was the maximum relative differential settlement calculated as 1:700, which was specified by the structural engineers. Further comparison of the maximum settlement with that of unpiled raft shows that the use of piled raft is advantageous in reducing the settlements by 70 %.

The associated load share of the raft corresponding to this settlement reduction was found to be 20 %, and is within the practical values of 0.3 to 0.9 from previous experience of [22]. The contribution of the raft is not large because the design was restricted with the specified deformation requirement, for which the piles were spaced according to the external loads with non-uniform spacing varying between 1.5D and 4.5D. These results of the present case are in a fair agreement with the plots of Fig. 7b, that the normalized settlement and pile-raft coefficient are almost the same, although the load and pile arrangements are different. Thus, the normalized charts of Fig. 7 can be used as guidelines for preliminary design of piled rafts in the area for the specific loading conditions. Further charts can be produced for other load levels, depending on practical developments in the region.

Load-settlement curves have been generated for selected points on the raft (around corners, core and edge of the raft) and plotted in Fig. 8, to determine the load-settlement behavior of the foundation system. All the load-settlement curves have similar patterns except the stiffer behavior at the left part of the raft (Location 1) due to the relatively smaller loads transferred to it. These curves are under the usual category of piled raft described in section Fig. 2b of this paper, non-distinctly recognizable failure states, showing gradual increment of the settlements with load. The observation of no abrupt increase of the settlements for gradual increment of applied load is also an indicator of the advantages of piled raft, that the foundation system doesn't show sudden failure at an expected ultimate load.

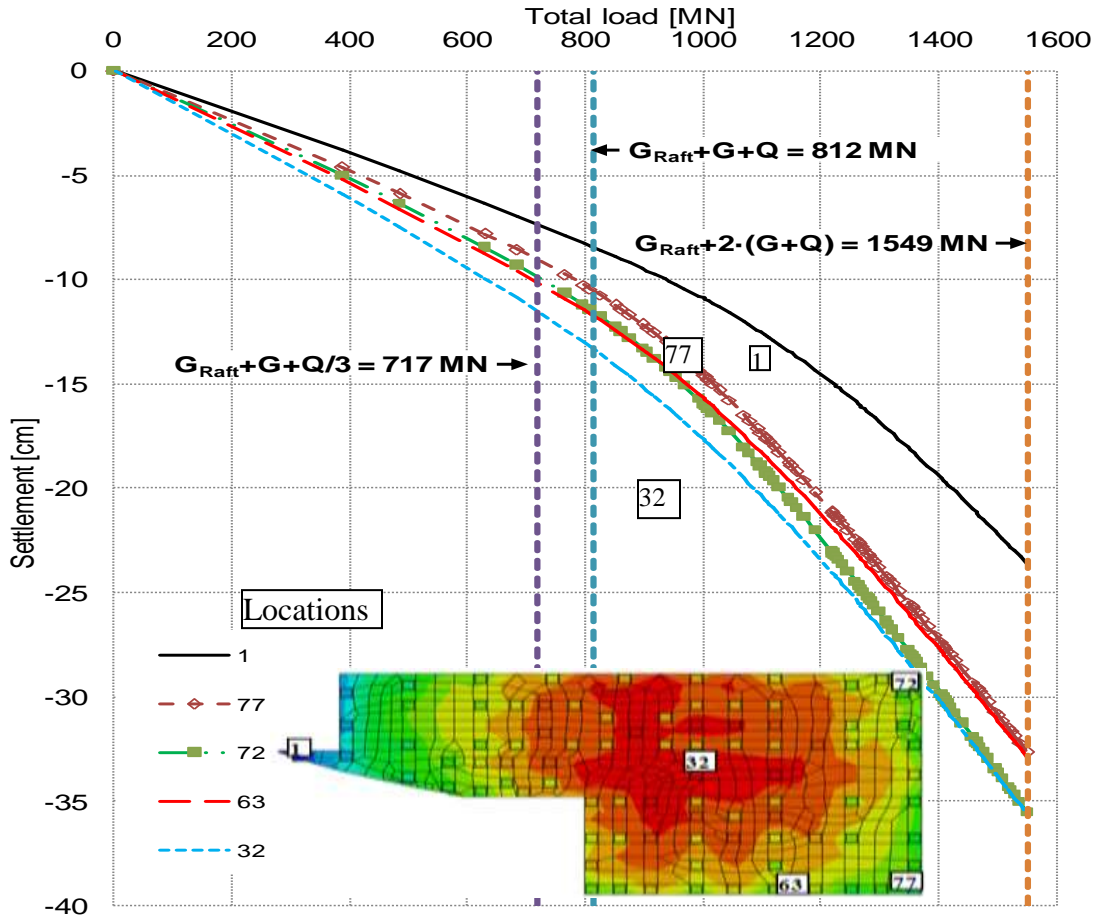


Fig. 8 Load settlement curves at different locations

### CONCLUSIONS

This research has focused on the behavior of piled rafts and their applicability on weak alluvial soils of the West African City Lagos, which do not show significant stiffness increment with depth, due to which the use of very long piles is associated with very high project costs. Extensive field and laboratory investigation results have been carefully interpreted and analyzed together with calibration of pile-load test measurements to set the soil parameters incorporated in the non-linear 3D Finite Element Analyses of foundation of multi-story buildings on the stratified alluvial deposits.

Normalized curves of maximum settlement versus pile-raft coefficient for common loading conditions with practical raft thickness ranges indicated the optimal ranges of applicability of piled rafts using two pile spacings, which have been chosen based on findings of previous research works. The common practice of using closely spaced and very long piles have been found to be disadvantageous for both settlement reduction and enhancing the load share of the raft.

The load share of the raft is actually dependent on the specific requirements of the projects regarding the maximum settlement, based on which economical arrangement of the foundation elements can give rise to its best load share. Under the same volume of structural members, the use of widely spaced piles has generally been found to enhance the efficiency of the foundation (reducing both the normalized settlement and the pile-raft coefficient). Economical spacing of the components can thus be considered as smaller pile meters with wider pile spacing, unless the use of higher pile meters is obliged to minimize the settlements, if that is restricted due to the requirements of the specific project.

The practical use of the normalized curves has later been checked by considering a specific site in the region by using piles of smaller length as the traditional practice in the region, which was found to be in good agreement with the general findings of the parametric studies. The load-settlement behavior of the piled raft for the specific site was also observed to have no significant super-proportionality, indicating the absence of sudden failure of the foundation system beyond ultimate loads, which is a characteristic of most piled rafts [12].

The general findings of the research show that piled rafts can be used as optimized foundation options for high-rise buildings on alluvial deposits and other comparable ground conditions which do not show significant increase in stiffness with depth. The use of densely configured long piles has been proved to bring nothing but economical loss, which is recommended to be avoided in the specific study area.

## REFERENCES

- [1] El-Mossallamy, Y., Lutz, B., Richter, R. (2006) *Innovative application of piled raft foundation to optimize the design of high-rise buildings and bridge foundations*. Proc. 10<sup>th</sup> International Conference on Piling and Deep Foundations, Amsterdam: 269-278.
- [2] Poulos, H.G., Small, J.C., Chow, H. (2011) *Piled raft Foundations for Tall Buildings*. Geotechnical Engineering Journal of the SEAGS & AGSSEA 42 (2): 78-84.
- [3] Yamashita, K., Yamada, T., Hamada, J. (2011) *Investigation of settlement and load sharing on piled rafts by monitoring full-scale structures*. Soils and Foundations 51(3): 513-532.
- [4] Gebregziabher, H.F. (2011) *Optimized Use of Combined Pile-Raft Foundation Design for High-Rise Buildings on Semi-Soft Soils*. Dissertation, Technische Universität Darmstadt.
- [5] Adeoye, A.A. (2010) *Lagos State Geoinformation Infrastructure Policy as a tool for Megacity Development: Opportunities and Challenges*. FIG Congress 2010, Sydney.
- [6] Height, D.W. and Green, P.A. (1976) *The performance of a piled raft foundation of a tall building in London*, Proc. 5<sup>th</sup> European Conference on Soil Mechanics and Foundation Engineering, Vienna, 1 (2): 467-472.

- [7] Russo, G., Viggiani, C., de Sanctis, L. (2004) *Piles as settlement reducers: a case history*. In: Potts and Higgins (eds) *Advances in geotechnical engineering: The Skempton conference*, Thomas Telford, London, Vol. 2, pp 1143-1154.
- [8] Hanisch, J., Katzenbach, R., König, G. (2002) *Kombinierte Pfahl-Plattengründung*. Ernst & Sohn, Berlin.
- [9] De Sanctis, L.Mandolini, A. (2006) *Bearing Capacity of Piled Rafts on Soft Clay Soils*. *Journal of Geotechnical and Geoenvironmental Engineering*, ASCE 132(12): 1600-1610.
- [10] Reul, O. (2004) *Numerical study on the bearing behaviour of piled rafts*. *Intl. Jnl. Geomechanics* 4(2): 59-68.
- [11] Wolff, Th., Witt, K.J., Hassan, A. (2007) *Experimental investigation at the load bearing capacity for deep foundation in Dubai (U.A.E)*. *Proc. 14<sup>th</sup> Darmstadt Geotechnical Conference*, Darmstadt Geotechnics, No. 15: 39-54.
- [12] Katzenbach, R., Bachmann, G., Gutberlet, C. (2007) *Soil-Structure-Interaction of deep foundations and the ULS design philosophy*. 15<sup>th</sup> European Conference on Soil Mechanics and Geotechnical Engineering, Madrid: 55-62.
- [13] CEN European Committee of Standardization, Eurocode 7: *Geotechnical design - Part 1: General Rules* (2004).
- [14] Katzenbach, R., Arslan, U., Moorman, C. (2000) *Piled Raft Foundation Projects in Germany*. In: Hemsley J.A. (ed), *Design applications of raft foundations*, Thomas Telford, London, pp 323-392.
- [15] Katzenbach, R., Choudhury, D. (2013) *ISSMGE Combined Pile Raft Foundation Guideline*. Darmstadt, Institute and Laboratory of Geotechnics, Darmstadt.
- [16] Faseki, O.E., Olatinpo, O.A., Oladimeji, A.R. (2016) *Assessment of Sub-Soil Geotechnical Properties for Foundation Design in Part of Reclaimed Lekki Peninsula, Lagos, Nigeria*. *International Journal of Advanced Structures and Geotechnical Engineering* 5 (4): 120-128.
- [17] Jones, H.A, Hockey, R.D. (1964) *The Geology of Part of South-Western Nigeria. Explanation of 1: 250,000 Sheets Nos. 59 and 68*.
- [18] Ademeso, O.A., Ademeso, V.F., Faseki, O.E. (2016) *Investigation of subsurface for engineering applications using standard penetration tests in Ikoyi, Lagos, southwest Nigeria*. *International Journal of Engineering Sciences* 5(2): 6-18.
- [19] Adebisi, N.O. and Fatoba, J.O. (2013) *Instrumentation for in-situ foundation investigation in Lagos, South West (SW) Nigeria*. *Journal of Geology and Mining Research* 5(4): 88-96.

- [20] Oyedele, K.F., Oladele, S., Okoh, C. (2015) *Assessment of Subsurface Conditions in a Coastal Area of Lagos using Geophysical Methods* Nigerian Journal of Technological Development 12(2): 36-41.
- [21] Bowles, J.E. (1996) *Foundation Analysis and design*. McGraw-Hill, New York.
- [22] Katzenbach, R., Leppla, S., Choudhury, D. (2016) *Foundation Systems for High-Rise Structures*. CRC, New York. 22
- [23] Mali, S., Singh, B. (2018) *Behavior of large piled-raft foundation on clay*. *Ocean Engineering*, 149(1): 205-216. 23
- [24] Gebregziabher, H.F., Katzenbach, R. (2012) *Parametric Studies on Application of CPRF on Semi Soft Stratified Soils*. Proceedings of the 2012 Geo Congress, ASCE, Oakland: 125-134.
- [25] Reul, O. (2010) Entwurf sop timierung von Hochhausgründungen. *Bauingenieur* 85: 177-187.

# NEUTRAL AXIS DEPTH PROFILE OF REINFORCED CONCRETE BEAMS

Abrham Gebre

School of Civil and Environmental Engineering, Addis Ababa Institute of Technology

Correspondence Author: abraham\_gebre@yahoo.com

## ABSTRACT

Many studies have been conducted for the estimation of effective moment of inertia expressions for Reinforced concrete (RC) beams. To compute deflection of reinforced concrete beams, study results show that the expressions for effective moment of inertia, in each case, are different and related to loading positions. As a result deflection of reinforced concrete beams using the empirical equations vary from the experimental values. In this study, variation in neutral axis depth profile of a simply supported reinforced concrete beam is studied and verified using experimental investigation. The experimental result reveal that neutral axis (NA) depth profile of a reinforced concrete beam varies longitudinally, moves with the load and in good agreement with the analytical curve. Moreover, a neutral axis depth profile and moment of inertia expression with parabolic functions for simply supported beam are proposed. These equations are to be used for the computation of deflection of reinforced concrete beams.

**Keywords:** Neutral axis depth, RC beam, effective moment of inertia, deflection

## INTRODUCTION

### Background

The variation in the modulus of elasticity with the increasing load is caused by the inelastic stress-strain behavior of concrete

beyond the elastic limits, while the variation in the moment of inertia is associated with the cracking of concrete due to the tensile strains greater than the cracking strain of concrete. The cracked zones in a concrete beam are ineffective in resisting stresses originating from applied loads and moments [1]. The overall moment of inertia of a concrete beam decreases gradually from the uncracked moment of inertia ( $I_{ucr}$ ) to the fully-cracked moment of inertia ( $I_{cr}$ ), as flexural cracks form at discrete locations along the span [1]. Deflections may be computed using the modulus of elasticity for concrete as specified in AASHTO [2, 3] by taking the effective moment of inertia expression proposed by Branson [4] and it is given in Eq. (1) by setting the value of  $m = 3$ .

$$I_{eff} = \left( \frac{M_{cr}}{M_a} \right)^m I_g + \left[ 1 - \left( \frac{M_{cr}}{M_a} \right)^m \right] I_{cr} \leq I_g \quad (1)$$

where:

$I_{eff}$  is effective moment of inertia ( $\text{mm}^4$ )

$M_{cr}$  is cracking moment (kN-m)

$I_g$  is the gross moment of inertia ( $\text{mm}^4$ )

$y_t$  is distance from the neutral axis to the extreme tension fiber (mm)

$I_{cr}$  is moment of inertia of the cracked section ( $\text{mm}^4$ )

$M_a$  is maximum moment in a component at the stage for which deformation is computed (kN-m)  $m$  is a constant

In cases when the effective flexural stiffness is assumed to be a function of flexural moment, the same expression as that of Eq. (1) with different exponent ( $m=4$ ) is given in JSCE Standard Specifications for Concrete Structures [5]. In some cases, the value of  $m$  decreases as the reinforcement ratio increases [1]. In this study, expressions for neutral axis depth and moment of inertia for simply supported beam are presented and verified experimentally.

Based on EC-2, reinforced concrete members behave in a manner intermediate between the uncracked and fully cracked sections and, the average curvature is given as follow [6]:

$$k = (1 - \xi)k_1 + \xi k_2 \quad (2)$$

where:

$k$  is the average curvature

$k_1$  is the curvature in the uncracked regions

$k_2$  is the curvature in the fully cracked regions

$\xi$  is distribution coefficient indicates how close the stress-strain state is to the condition causing cracking. It takes a value of zero at the cracking moment and approaches unity as the loading increases above the cracking moment.

Moreover, statistical parameters have been established for reinforced concrete beam specimens and deflection predictions made by the finite element package and design code methods ACI and EC2 was investigated. The result shows that, in most cases deflections were overestimated at the initial load intervals close to the cracking load. Justification for that were large standard deviations [7].

### Computation of Neutral Axis Depth and Moment of Inertia

Based on AASHTO LRFD [2] and Chen et al. [8], for cracked section, the neutral axis depth and moment of inertia are given in Eqs. (3a) and (3b), respectively.

$$y_0 = \sqrt{0.5b(nA_s(d - y_0) + (n-1)A'_s(d' - y_0))} \quad (3a)$$

$$I_{cr} = \frac{by_0^3}{3} + nA_s(d - y_0)^2 + (n-1)A'_s(y_0 - d')^2 \quad (3b)$$

where:

$d$  is effective depth (mm)

$b$  is width (mm)

$d'$  is position of compression steel, measured from the top fiber (mm)

$A_s$  is area of steel in tension (mm<sup>2</sup>)

$A'_s$  is area of steel in compression (mm<sup>2</sup>)

$n$  is modular ratio,  $E_s/E_c$

$y_0$  is neutral axis depth of the fully cracked section, measured from the top fiber (mm)

$I_{cr}$  is moment of inertia of the cracked section (mm<sup>4</sup>)

For uncracked section, the neutral axis depth and moment of inertia [2,] are given in Eqs. (4a) and (4b), respectively.

$$y_1 = \frac{0.5bh^2 + (n-1)(A_s d) + (n-1)(A'_s d')}{bh + (n-1)A_s + (n-1)A'_s} \quad (4a)$$

$$I_{unc} = \frac{bh^3}{12} + bh\left(\frac{h}{2} - y_1\right)^2 + (n-1)A_s(d - y_1)^2 + (n-1)A'_s(y_1 - d')^2 \quad (4b)$$

where:

$h$  is total depth (mm)

$y_1$  is neutral axis depth of the uncracked section, measured from the top fiber (mm)

$I_{unc}$  is moment of inertia of the uncracked section (mm<sup>4</sup>)

### Variation in Neutral Axis Depth Profile

To compute the effective moment of inertia, the variation in the neutral axis depth and moment of inertia along the span is taken into account. Actually, the neutral axis along the longitudinal line is not constant due to the tensile strength of concrete and the variation in effective reinforcement ratio in the section. For uniformly distributed loads, since the neutral axis depth is related to bending moment, a parabolic neutral axis and variable moment of inertia along the longitudinal direction are assumed [9]. The neutral axis depth profile be expressed by a quadratic equation given in Eq. (5).

$$\bar{y} = ax^2 + bx + c \quad (5)$$

where:

$\bar{y}$  is neutral axis depth at a section, measured from the top fiber (mm)

$x$  is distance measured from the left support of the beam (m)

$a$ ,  $b$  and  $c$  are constants

For the derivations of neutral axis depth variation and to obtain expressions for the moment of inertia along the line of a beam of new structures, consider the longitudinal cross section of a simply supported beam shown in Fig. 1. In the figure,  $y_l$  the neutral axis depth of the uncracked section and  $\bar{y}_0$  is the neutral axis depth of the fully cracked section, measured from the top fiber (mm).

The basic assumption considered is that the neutral axis profile varies with the load,

depends on its position and crack occurs at points where the bending moment is sufficiently large [9].

For new RC structures, the neutral axis depth profile is not steady and it moves with the load. In such a case, for the computation of moment of inertia, envelope for neutral axis depth profile is important. For old structures, for the derivation of neutral axis depth and moment of inertia at a section, the neutral axis depth is assumed to be independent of the location of the load and the section is fully cracked at the mid span [9]. Combining Eqs. (3a), (3b), (4a), (4b) and inserting to Eq. (5) gives a simplified neutral axis depth profile expression. The expression for the neutral axis depth profile is given in Eq. (6). In Eq. (6), the constants  $a$ ,  $b$  and  $c$  are determined from boundary conditions. The boundary conditions are: at  $x = 0$ ,  $\bar{y} = c = y_l$ , at  $x = x_l$ ,  $\bar{y} = y_0$  and at  $x = L$ ,  $\bar{y} = y_l$ . Upon substitution, the following expression for the neutral axis depth, except at  $x_l = 0$  is obtained.

$$\bar{y} = \frac{(y_0 - y_l)}{x_l(L - x_l)}(Lx - x^2) + y_l \quad (6)$$

where:

$L$  is length of the beam (m)

$x_l$  is location of load position, measured from the left support of the beam (m)

Upon substitution and simplification of Eq. (6), the expressions for NA depth and moment of inertia of a simply supported reinforced concrete beam at a section are expressed as follows.

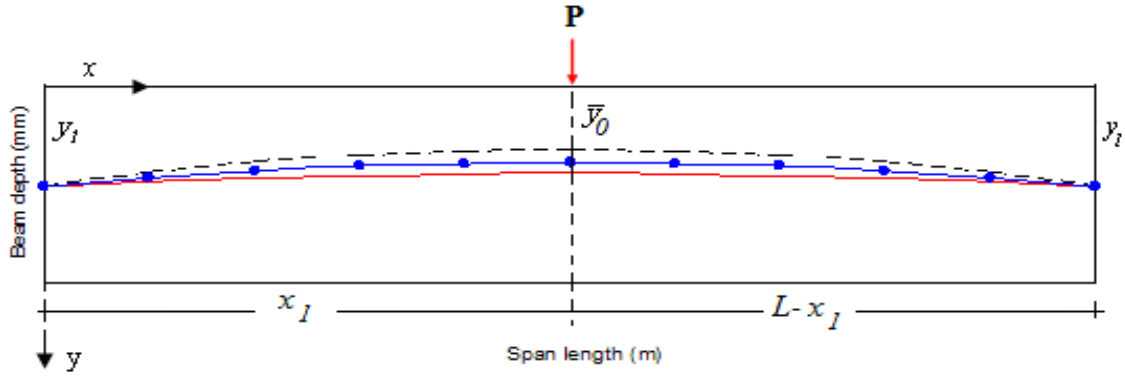


Fig. 1 Concept of variation in neutral axis profile at different loading condition

$$\bar{y} = y_1 \left( \frac{2x}{L} \right)^2 + y_0 \left( 1 - \left( \frac{2x}{L} \right)^2 \right) \quad (7)$$

$$I(x) = I_1 \left( \frac{2x}{L} \right)^2 + I_{cr} \left( 1 - \left( \frac{2x}{L} \right)^2 \right) \quad (8)$$

Due to the variation in applied load and cracking moment of concrete, the neutral axis depth,  $y_0$  is not constant and hence the effect of applied load has to be considered. The concept of variations in neutral axis profile due to a change in the applied load is shown in **Fig. 1**. By considering the variation in  $y_0$  as a second degree equation, the modified neutral axis depth of the cracked section is expressed as follow.

$$\bar{y}_0 = a_1 \beta^2 + c_1 \quad (9)$$

where:

$a_1, c_1$  are constants

$\bar{y}_0$  is modified neutral axis depth of the cracked section, measured from the top fiber (mm)

$\beta$  is ratio of  $M_a / M_{cr}$

The boundary conditions are: at  $\beta=0$ ,  $\bar{y}_0 = y_1$  and at  $\beta \geq 1$ ,  $\bar{y}_0 = y_0$ . Expressions for the modified neutral axis and moment of inertia of the cracked section are given in

Eq. (11) and Eq. (12). The modified neutral axis profile at any section is given in Eq. (10).

$$\bar{y}_0 = \beta^2 y_0 + (1 - \beta^2) y_1 \geq y_0 \quad (10)$$

$$\bar{I}_{cr} = \beta^2 I_{cr} + (1 - \beta^2) I_{unc} \geq I_{cr} \quad (11)$$

$$\bar{y} = \frac{(\bar{y}_0 - y_1)}{x_1(L - x_1)} (Lx - x^2) + y_1 \quad (12)$$

where:

$\bar{I}_{cr}$  is modified moment of inertia of the cracked section corresponding to  $\bar{y}_0$  ( $\text{mm}^4$ )

A similar method is used to get an expression for moment of inertia at a section.

$$I(x) = \frac{(\bar{I}_{cr} - I_{unc})}{x_1(L - x_1)} x(L - x) + I_{unc} \quad (13)$$

where:

$I(x)$  is moment of inertia at a section ( $\text{mm}^4$ )

For old (already cracked) structures, the distribution of the neutral axis profile is independent of load position, and it does not move with load and is assumed to be unchanged since the section is already

## Neutral Axis Depth Profile of Reinforced Concrete Beams

cracked by the maximum possible load experienced in the past [9]. In this case, the boundary conditions are: at  $x=0$ , and at  $x=L$ ,  $\bar{y} = y_1$ , at  $x=L/2$ ,  $\bar{y} = \bar{y}_0$ .

Upon substitution and simplification, the expressions for the neutral axis depth and moment of inertia at a section are given in Eqs. (14) and (15), respectively.

$$\bar{y} = \left( \frac{4x}{L^2} (L-x) \right) \bar{y}_0 + \left( 1 - \left( \frac{4x}{L^2} (L-x) \right) \right) y_1 \quad (14)$$

$$I(x) = \left( \frac{4x}{L^2} (L-x) \right) \bar{I}_{cr} + \left( 1 - \left( \frac{4x}{L^2} (L-x) \right) \right) I_{unc} \quad (15)$$

For uniformly distributed loads, since the neutral axis depth is related to bending moment, a parabolic neutral axis profile and variable moment of inertia along the longitudinal direction are assumed [9].

### Experimental Investigation of NA Depth Profile of RC Beam

To verify the variation in the NA depth profile with the load position a RC beam was prepared, experimentally tested and the result was analyzed.

#### Materials

Concrete with a 28 days characteristic compressive strength,  $f'_c$ , of 31.82MPa and steel bar with yield strength of 528MPa were used.

#### Test Specimen

A test beam specimen with rectangular cross section of  $b \times h = 500 \times 485\text{mm}$ , with overall length of 3200mm and 2800mm distance between supports was prepared. Four deformed bars on the bottom and three deformed bars on top surfaces with 35mm in diameter were provided. For the stirrups,

16mm diameter deformed bars with a spacing of 200mm were used. Fig. 2 shows the cross section of the beam. Strain gauges for steel bars and concrete are attached at 0.4m intervals.

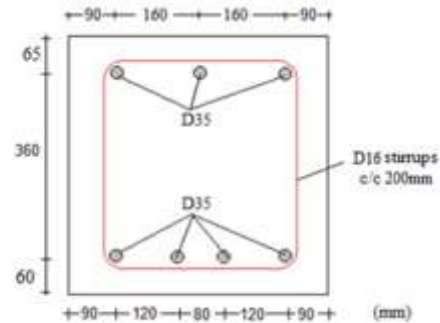


Fig. 2 Cross section of RC beam [9]

Strain gauges for steel and concrete at both top and bottom parts are attached. Locations of strain gauges are shown in Fig. 3.

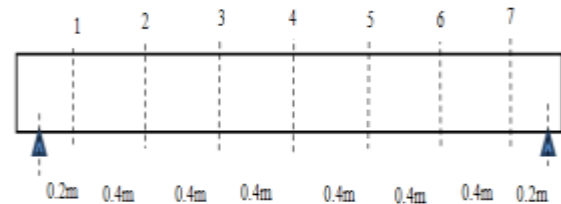


Fig. 3 Locations of strain gauges

#### Methods

To test the RC beam specimen, as per the recommendation of ASTM C 78 – 02, a standard test method for flexural strength of concrete beams using simple beam with three-point loading was used [10]. The specimen was simply supported at both ends and tested for with loading points symmetrically spaced at 400mm, 1200mm and 2000mm apart. The different load positions are shown in Table 1.

Table 1 Loading positions

Load position	1 <sup>st</sup> load from left support (x)	Load spacing (y)
Position 1	1.2m	0.4m
Position 2	0.8m	1.2m
Position 3	0.4m	2.0m

**RESULTS AND DISCUSSIONS**

By varying the magnitude and position of loads, nine different cases (by varying load position and magnitude) have been considered. Initially, at the specified load positions, the beam was loaded with 70kN load (below cracking load). This test was repeated (Fig. 4) and subsequently a load beyond cracking load is applied at the same load positions. The maximum load applied was 300kN.

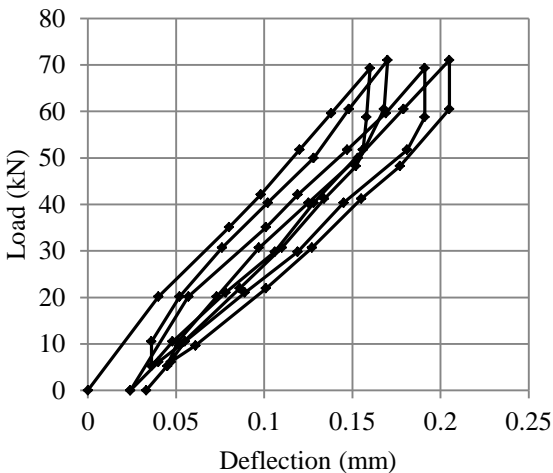


Fig. 4 Load deflection diagram of the test beam due to repeated loading

The neutral axis depth of reinforced concrete specimen at a particular section for different loading position is calculated from the strain distributions shown in Figs. 5-7 and the corresponding neutral axis depth profile is plotted. For other loading positions and values, similar procedure has been followed.

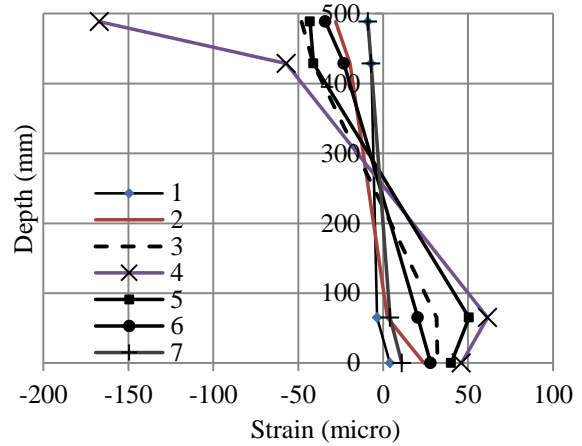


Fig. 5 Stain distribution at 70kN (Position-1)

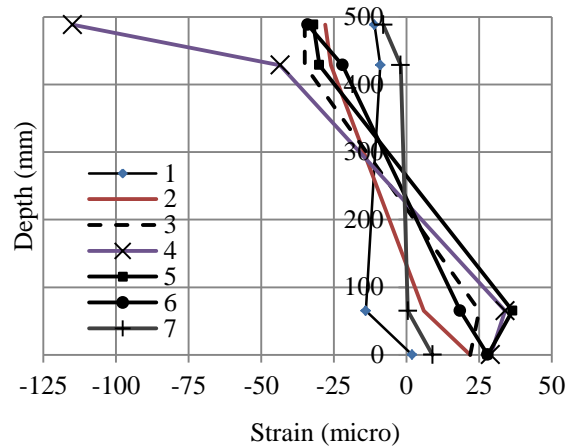


Fig. 6 Stain distribution at 70kN (Position-2)

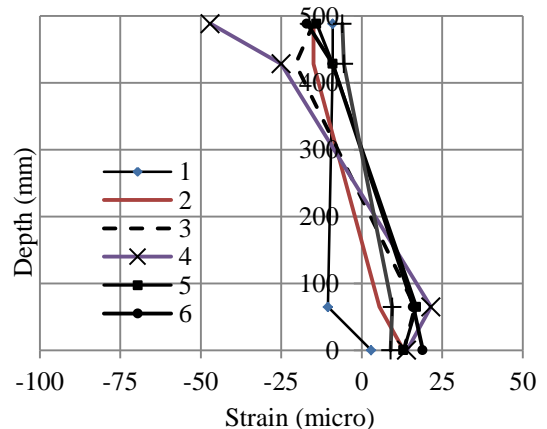


Fig. 7 Stain distribution at 70kN (Position-3)

## Neutral Axis Depth Profile of Reinforced Concrete Beams

The beam is unloaded and loaded to  $P=300\text{kN}$  until the section has fully cracked. The crack pattern of the test beam specimen at  $300\text{kN}$  is shown in Fig. 8.

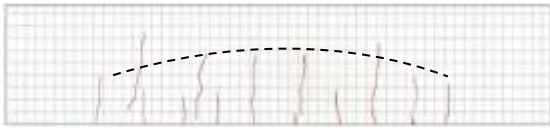


Fig. 8 Crack pattern at  $300\text{kN}$

As shown in Fig. 8, the crack pattern of the test beam at  $300\text{kN}$  is parabolic and follows the assumption. Based on the experimental results, variations of NA profile for each loading case is drawn along the longitudinal profile of the beam are plotted and shown in Figs. 9-11. As shown in these figures, the neutral axis depth profile varies with the magnitude of the load. After the section has fully cracked the NA depth profile remains constant along the longitudinal profile of the beam.

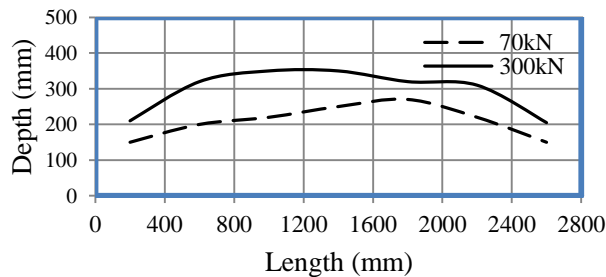


Fig. 9 Variation of NA Profiles (Position-1)

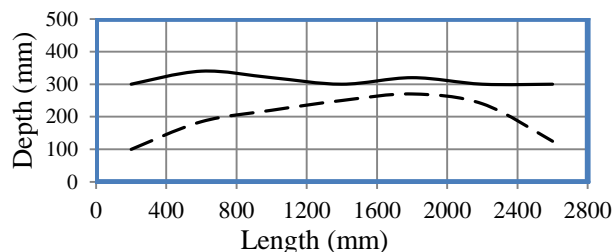


Fig. 10 Variation of NA Profiles (Position - 2)

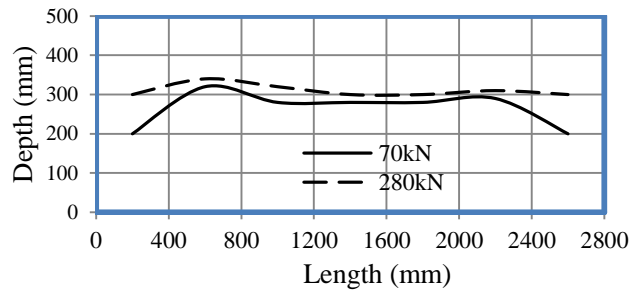


Fig. 11 Variation of NA Profiles (Position3)

As shown in Fig.11, as the spacing between the concentrated loads increases ( $1200\text{mm}$ ), the NA depth profiles are almost in similar position.

Based on the strain readings of concrete and steel bars of the experimentally tested beam specimen at different sections, the contour showing the strain distributions are plotted. The strain distribution of concrete at the top and bottom fibers of the beam at a loading stage of  $300\text{kN}$  is shown in Fig. 12. Moreover, the strain distributions of steel at the top and bottom reinforcement zones at the loading stage of  $70\text{kN}$  and  $300\text{kN}$  are shown in Figs. 13-14. As shown in the figures, the NA depth profile along the longitudinal axis of the beam is variable and follows a parabolic path.

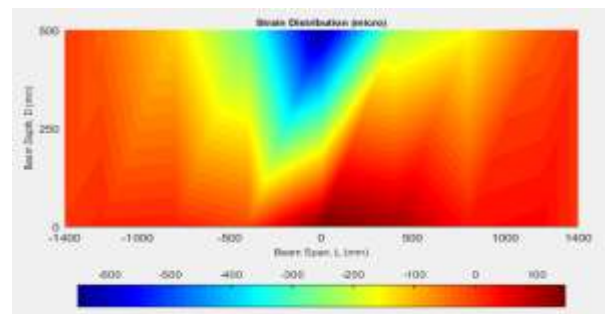


Fig. 12 Stress Distribution (Position-1, Concrete at  $300\text{kN}$ )

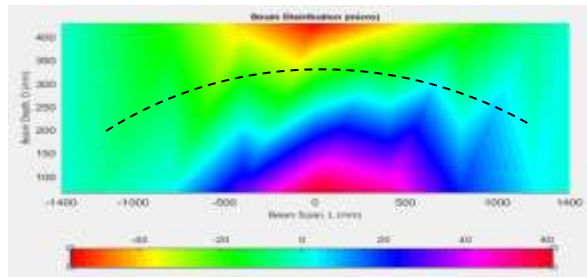


Fig. 13 Stress Distribution (Position-1, Steel at 70kN)

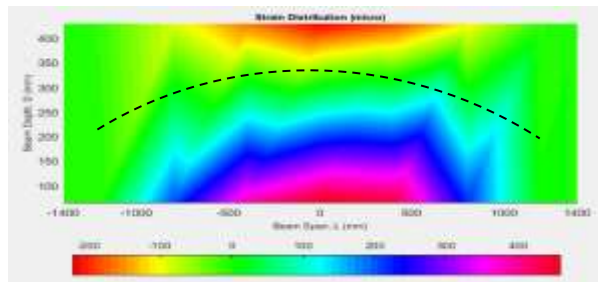


Fig. 14 Stress Distribution (Position-1, Steel at 300kN)

The NA depth for cracked and uncracked section become:  $\bar{y}_0 = 156.72\text{mm}$  and  $y_1 = 247.09\text{mm}$ , respectively. For different load positions, the NA depth profile of the RC beam was calculated numerically using Eq. (12) and compared with the experimental results (Fig. 15).

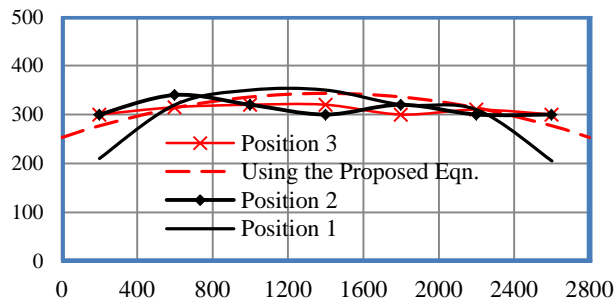


Fig. 15 Variation of NA Profiles

As shown in Fig. 18, it is observed that the NA depth profile of the experimental cases coincides with the values obtained using the numerical equation proposed by this study.

## CONCLUSIONS

- 1) For limited data of experimental results, expression for the computation of neutral axis depth and moment of inertia of single-span simply supported RC beam have been obtained.
- 2) Comparison of empirical expressions of NA depth profile of a RC beam with experimental results has been carried out.
- 3) The experimental result reveal that NA depth profile of a RC beam varies longitudinally, moves with the load and in good agreement with the analytical curve.
- 4) During calculation of deflection of RC beams variation of NA depth profile along the longitudinal axis of the beam should be considered and variation of moment of inertia should be used accordingly.
- 5) Expressions for the computation of neutral axis depth and moment of inertia can be extended for beams with different end conditions.

## REFERENCES

- [1] Kalkan, I.: *Deflection Prediction for Reinforced Concrete Beams Through Different Effective Moment of Inertia Expressions*, *Int. J. Eng. Research & Development*, Vol.2, No.1, pp.72-80, January 2010.
- [2] AASHTO: *American Association of State Highway Officials, LRFD Bridge Design Specifications, 4th edition*, Washington, 2007.
- [3] ACI-ASCE Committee 343, *Analysis and Design of Reinforced Concrete Bridge Structures (ACI 343R-95) USA*, 1995

## Neutral Axis Depth Profile of Reinforced Concrete Beams

- [4] Branson, D. E: Instantaneous and Time-Dependent Deflections of Simple and Continuous Reinforced Concrete Beams, HRP Report No.7 Part 1, Auburn University .
- [5] JSCE Guidelines for concrete, No.15, Standard Specifications for Concrete Structures, 2007.
- [6] DD ENV 1992-1-1:1992, *Eurocode 2: Design of concrete structures-Part 1: General rules and rules for buildings*
- [7] *Deflection Calculation of RC Beams: Finite Element Software Versus, Design Code Methods* retrieved from [https://e-pub.uni-weimar.de/opus4/frontdoor/deliver/index/docId/249/file/icccbe-x\\_227\\_pdfa.pdf](https://e-pub.uni-weimar.de/opus4/frontdoor/deliver/index/docId/249/file/icccbe-x_227_pdfa.pdf)
- [8] W.F., Duan, L.: *Bridge Engineering Handbook*, CRC Press LLC, Washington, D. C., 2000.
- [9] Tarekegn, A.G., Tsubaki, T.: *Restoration Design for RC Slab Bridges by AASHTO LFRD, The 21<sup>st</sup> PC Symposium on Developments in Prestressed Concrete, JPCA, pp. 29-34, Oct. 2012.*
- [10] ASTM C 78 – 02, *Standard Test Method for Flexural Strength of Concrete Using Simple Beam with Three-Point Loading*, *Annual Book of ASTM Standards, Vol. 04.02*, ASTM International, 100 Barr Harbor Drive, West Conshohocken, PA, United States, 2002.



# ANCIENT ETHIOPIC MANUSCRIPTS CHARACTER RECOGNITION USING DEEP BELIEF NETWORKS

Siranesh Getu<sup>1</sup>, Eneyachew Tamir<sup>1</sup> and Menore Tekeba<sup>2</sup>  
Corresponding Author's Emails: saragetu8@gmail.com

<sup>1</sup> School of Electrical and Computer Engineering, Bahir Dar IOT, Bahir Dar University

<sup>2</sup> School of Electrical and Computer Engineering, AAIT, Addis Ababa University

## ABSTRACT

*Very large proportion of Ethiopian literature is found in ancient ge'ez manuscripts in the form of old scriptures with papers from animal hides and skins (Branas) on which the ancient Ethiopic knowledge and civilization is recorded. This knowledge can be extracted and made usable by applying optical character recognition (OCR) systems on document images. Little efforts have been done for OCR of Ethiopic ancient manuscripts. Hand written OCR process is considered as one of the most challenging problems in the area of image processing . The unique morphology of ge'ez hand-writing system (known as "Kum Tsihfet"), the degraded quality of the documents, and non-uniform background of the Branass poses additional challenges. Because of this, the OCR technique employed can't be addressed directly by using OCR systems designed for modern printed and handwritten documents. Machine learning techniques like deep belief networks (DBNs) are becoming powerful set techniques that attempt to model complicated morphological features of handwritten texts. In this research we developed an OCR system using DBNs. The system was trained and tested using our own segmented datasets of ancient ge'ez characters containing 24 base characters only. The test result shows that a recognition accuracy of 93.75% was obtained, which is a promising result.*

**Keywords:** OCR, Deep Belief Networks, Ancient Ge'ez documents

## INTRODUCTION

OCR is the process of detecting and recognizing characters from input image

and converting into machine editable text. There are two types of handwriting recognition: off-line and on-line. The off-line OCR uses image documents from computers and converts those document images to texts. The on-line OCR systems directly takes the writers pen strokes from writing pads and converts those pen-strokes and lines directly to sequences of words [1]. As per the research work given in [2], the online hand-written OCR systems performs better accuracy using temporal pen stroke directions and sequences for recognition task.

Handwritten document recognition is considered as one of the most challenging problems in the area of image processing by many researchers. Different algorithms and systems have been proposed and implemented in the area of off-line character recognition [2]. Offline recognition system follow holistic and segmentation based approaches [3]. The holistic approach is used to recognize limited size vocabulary of words where global features extracted from the entire word image are considered. As the size of the vocabulary of words increases, the complexity of holistic based algorithms also increases and correspondingly the recognition rate decreases rapidly [4]. The segmentation based strategies, on the other hand, employ bottom-up approaches, starting from the stroke or the character level and going towards producing a meaningful word. After segmentation the problem gets reduced to the recognition of simple isolated characters or strokes and hence the system can be employed for unlimited vocabulary [4].

Many of the approaches proposed mainly focus on recognizing characters or words of specific language, which consists of its own specific features [3].

The off-line OCR systems are used to covert modern printed documents, handwritten documents, and ancient handwritten documents which are produced before printing technology starts. Geez is one of the world's ancient languages [5] and enormous amounts of handwritten material are found in churches, monasteries, museums, libraries, and many places of Europe and America stolen by travelers and invaders. These scripts are mostly written in parchments, and consist of intrinsic values and unexplored content until today.

To the best of our knowledge, there is no a research work done to address OCR issues associated with Ethiopic ancient manuscript characters of having “Kum Tsihfet” style and the rich cultural, technology, artistic, governance, science, religious and other knowledge and wisdom left unexplored due to lack of such solutions. The aim of this study is, therefore, to develop an OCR system using DBNs, train and test the network with our own segmented dataset of 24 (out of 26) base characters of Ge'ez which are shown in the first column of Figure 1.

It must be acknowledged also that there are no upper or lower case distinctions in Geez. The total geez characters are 182 without geez numbers and diacritics.

Researches on offline OCR systems are generally done for two types of documents: printed and handwritten. A reach set researches on printed text exist, [6, 7, 8] for Amharic and [2, 9] for other languages with promising results. However only limited attempts were made [3, 10, 11] in the area of Amharic handwritten document, which reveals itself open to research.

ሀ	ሁ	ሂ	ሃ	ሄ	ህ	ሆ
ለ	ሉ	ሊ	ላ	ሌ	ል	ሎ
ሐ	ሑ	ሒ	ሓ	ሔ	ሕ	ሖ
መ	ሙ	ሚ	ማ	ሚ	ም	ሞ
ሠ	ሡ	ሢ	ሣ	ሤ	ሥ	ሦ
ረ	ሩ	ሪ	ራ	ራ	ር	ሮ
ሰ	ሱ	ሲ	ሳ	ሴ	ስ	ሶ
ተ	ቱ	ቲ	ታ	ቲ	ት	ቶ
በ	ቡ	ቢ	ባ	ቤ	ብ	ቦ
ተ	ቱ	ቲ	ታ	ቲ	ት	ቶ
ኀ	ኁ	ኂ	ኃ	ኄ	ኅ	ኆ
ኦ	ኇ	ኈ	኉	ኰ	኱	ኲ
ኣ	ኣ	ኣ	ኣ	ኣ	ኣ	ኣ
ከ	ከ	ከ	ከ	ከ	ከ	ከ
ወ	ወ	ወ	ወ	ወ	ወ	ወ
ዐ	ዐ	ዐ	ዐ	ዐ	ዐ	ዐ
ዘ	ዘ	ዘ	ዘ	ዘ	ዘ	ዘ
ዩ	ዩ	ዩ	ዩ	ዩ	ዩ	ዩ
ደ	ደ	ደ	ደ	ደ	ደ	ደ
ገ	ገ	ገ	ገ	ገ	ገ	ገ
ጠ	ጠ	ጠ	ጠ	ጠ	ጠ	ጠ
ጸ	ጸ	ጸ	ጸ	ጸ	ጸ	ጸ
ጸ	ጸ	ጸ	ጸ	ጸ	ጸ	ጸ
ፀ	ፀ	ፀ	ፀ	ፀ	ፀ	ፀ
ፈ	ፈ	ፈ	ፈ	ፈ	ፈ	ፈ
ፕ	ፕ	ፕ	ፕ	ፕ	ፕ	ፕ

Figure 1: Geez Characters

As a contribution we developed an OCR system based on machine learning technique that implements DBN. In order to train and test the system, we prepared our own data sets that consists of a total of 2400 characters (100 images of the 24 base characters) extracted from 200 pages of selected ancient Ethiopic manuscripts. Subjective evaluation using percentage accuracy of performance of the system was done by examining outputs the different stages.

The rest of this paper is organized as follows: section 2 presents literature review on OCR system. Section 3 describes the methodology and implementation approach followed in this research. Test and results at different stages of the entire system is described in section 4. Finally, conclusion and future works are indicated in section 5.

### LITERATURE REVIEW

There are different ancient languages in the world with their own alphabet for writing. Books that are primed by those ancient languages reveal much information and technology to the current situation of

our world. Especially in Ethiopia, Geez scripts contain many unexplored contents. One of the tasks in processing of these documents is recognition of texts so that they can be converted to forms that can easily be processed by a machine. The advent of computing machines and the need for processing large volumes of data motivated research and development for automatic recognition of those ancient and up to date texts. On the other hand one language differs from another in writing styles, character shape, space, overlaps, and the connection of characters and also the material used to write. These problems have become challenging for many researchers in producing solution in converting to computer readable format. The research of ancient Ethiopic manuscript processing is almost unexplored. This section presents the pervious works on ancient script, modern scripts and finally Amharic recognition using different techniques.

The work in [12] investigates ancient Slavonic manuscripts from the 11th century. They propose a binarization-free approach based on local descriptors to minimize the consequences of false character segmentation. Initially Scale Invariant Feature Transform (SIFT) features are extracted which are subsequently classified using Support Vector Machines (SVM). The system was evaluated on real world data, a dataset that consists of highly degraded Glagolitic characters. Experiments on this dataset proved the systems capability to recognize degraded characters and the difference to well preserved characters [12].

The writers in [9] applied Convolutional Neural Networks (CNNs) for offline handwritten English character recognition. They modified the common model of CNN, which is LeNet-5CNN model, with special settings of the number of neurons in each layer and the connecting way between some layers. Experiments were

done based on lower case and upper case section. These two sections contain 28069 samples for uppercase and 61351 samples for lowercase from UNIPEN dataset. In order to obtain offline character images, they employ some preprocessing steps like connecting the adjacent points, extending the width of strokes and anti-aliasing. For training of the CNN, an error-samples-based reinforcement learning strategy is developed. Experiments are evaluated on UNIPEN lowercase and uppercase datasets, with recognition rates of 93.7% for uppercase and 90.2% for lowercase, respectively [9].

Another approach on Ethiopic scripts [10] tries to recognize offline handwritten Amharic words based on lexicon. The system computes directional fields of scanned handwritten documents, from which pseudo characters are segmented. They developed and proposed an algorithm for such character and word segmentation, and also script-independent text line detection tasks using direction field image. The system is tested by a database of unconstrained handwritten Amharic documents collected from various sources. They prepared the lexicon from words appearing in the collected database. Form their result, for good quality texts, they achieved a recognition rate of 87% and for poor quality texts, the recognition rate was 58% [10].

### **METHODOLOGY AND IMPLEMENTATION DETAILS**

The proposed system includes the basic steps shown in Figure 3.1 namely, image acquisition, preprocessing, segmentation, classification and recognition [11, 13]. The details of the methods are given in [11].

#### **Dataset Preparation**

We have prepared a dataset both for training and testing the OCR of ancient characters of Ethiopic manuscripts. The dataset preparation involved several steps from image acquisition followed by different image processing algorithms and

finally segmentation of characters using vertical and horizontal histograms projection. The steps used to prepare the dataset are given in the following steps:

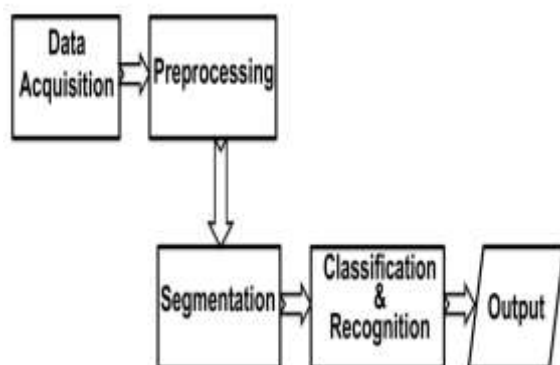


Figure 3.1 Block diagram of proposed system

### Image Acquisition

The input image can be taken through camera or scanner. The first stage in character recognition (CR) is image acquisition, which involves getting digital image of manuscript pages for input to the system. We collected about 200 pages of ancient Ethiopic manuscripts from different sources such as Ethiopian Orthodox Tewahido Churches, monasteries and also from National Archives and Library Agency for data preparation.

### Preprocessing

This step involves the following tasks:

**Grey Scale Conversion and Binarization:** Images which are in color are converted to grayscale before binarization is applied. Binarization is used to remove the noise and improves the quality of the documents by converting the gray-scale document images to black and white (binary) ones. Binarization is required because documents can often suffer degradation problems, especially in the case of historical documents due to unwanted foreground information (noise) [14]. Based on the threshold values used, there are two general techniques for binarization [15, 4]: Global binarization

and local binarization thresholding. But a technique for ancient or historical documents specifically is proposed in [14] and shows a very good result. This method is called hybrid binarization technique and we have used for our images.

**Skew Detection and Correction:** The relative inclination angle of the page being acquired during scanning or taking photo of the page must be detected and accounted for as it can cause serious performance deterioration of segmentation and recognition stage of document processing system [16].

Since skew observed in our input images are global skew problem which occurs due to capturing the scripts through digital camera or rotated scanning, it can be detected and corrected using Bounding Box Technique. Bounding Box technique [16] is a way of finding the extreme corners of text image. The advantage of this Bounding box algorithm is that if any two of the four corner points detected correctly, it will give the accurate skewed angle and it is also computationally inexpensive when compared to other methods.

**Noise Reduction:** There are many kinds of noise in images like Salt and Pepper Noise, the black points and white points sprinkled all over an image [17]. These can be reduced using filtering and applying morphological operations. We have applied morphological operation at this stage.

### Segmentation

Segmentation of hand written text document into individual character or digit is an important and crucial phase in document analysis and character recognition. There are various factors such as noise and disconnected characters that affects the process of text image segmentation [18]. The quality of the image is a significant factor for text

segmentation. In Ancient Ethiopic scripts due to ageing the text is highly affected by background noise, drop of ink and handling problem. We have used vertical profile projection for line segmentation and horizontal profile projection for individual character segmentation as it is given in [18, 19, 20].

### **Classification and Recognitions**

**DBNs for OCR of Ancient Ethiopic Manuscripts:** OCR systems extensively use the methodologies of pattern recognition, which assigns an unknown sample into a predefined class. Numerous techniques for OCR can be investigated in four general approaches of pattern recognition [21]: Template Matching, Statistical Techniques, Structural Techniques, and Neural Networks but each of these approaches except the neural network approach lacks flexibility to adapt to new unseen challenges and we have selected neural network approaches for our particular problem.

From neural networks, deep learning neural networks are powerful set of techniques. Learning in deep neural networks, is a branch of machine learning based on a set of algorithms that attempt to model high-level abstractions in data by using multiple processing layers with complex structures, or otherwise composed of multiple non-linear transformations. One of the promises of deep learning is replacing handcrafted features with efficient algorithms for unsupervised or semi-supervised feature learning and hierarchical feature extraction [22].

According to Bengio et al. [14], shallow architectures have been shown effective in solving many simple or well-constrained problems, but their limited modeling and representational power can cause difficulties when dealing with more complicated real-world applications involving natural signals such as human

speech, natural sound and language, and natural image and visual scenes. To solve this problem, it is recommended to represent a highly-varying function compactly (with few parameters) through the composition of many non-linearities, i.e., with a deep architecture. [14]

DBNs are one type of deep learning algorithms which uses a greedy layer-wise unsupervised pre-training and a light-weight supervised fine-tuning any back-propagation training algorithms [14].

**Training DBNs:** Applying gradient descent using back propagation is known empirically to find poor solutions for networks with 3 or more hidden layers. For that reason, artificial neural networks have been limited to one or two hidden layers [23].

Hinton et al. recently introduced a greedy layer-wise unsupervised learning algorithm, a generative model with many layers of hidden causal variables [14]. Greedy layer wise training is proposed to train a network taking one layer at a time, i.e. train layers sequentially starting from bottom (input) layer. Unsupervised training makes each layer learn a higher-level representation of the layer below. Then neural network is fine-tuned to the global supervised objective. The most common algorithms to train each layer in deep neural network using greedy layer wise unsupervised strategy are Restricted Boltzmann Machine (RBM) and auto-encoder (AE). AE uses back propagation algorithm for semi-supervised training of each layer pairs and computationally intensive. Therefore, we have used RBM as our training algorithm.

RBM is a generative model that uses a layer of binary variables to explain its input data [23, 24], undirected bipartite graphical model with connections between visible nodes and hidden nodes. The pixels correspond to visible units of the RBM because their states are observed; the

feature detectors correspond to hidden units. A joint configuration,  $(\mathbf{v}, \mathbf{h})$  of the visible and hidden units has an energy given by:

$$p(\mathbf{v}, \mathbf{h}) = \frac{1}{Z} e^{-E(\mathbf{v}, \mathbf{h})} \quad (1)$$

$Z$  is called partition function and is given by summing over all possible pairs of visible and hidden vectors given by:

$$Z = \sum_{\mathbf{v}, \mathbf{h}} e^{-E(\mathbf{v}, \mathbf{h})} \quad (2)$$

The probability that the network assigns to a visible vector,  $\mathbf{v}$ , is given by summing over all possible hidden vectors:

$$p(\mathbf{V}) = \frac{1}{Z} e^{-E(\mathbf{v}, \mathbf{h})} \quad (3)$$

The derivative of the log probability of a training vector with respect to a weight is given by:

$$\frac{\partial \log p(\mathbf{V})}{\partial w_{ij}} = \langle V_i h_j \rangle_{data} - \langle V_i h_j \rangle_{model} \quad (4)$$

This leads to a very simple learning rule for performing stochastic steepest ascent in the log probability of the training data which is given by:

$$\Delta w_{ij} = \epsilon \langle V_i h_j \rangle_{data} - \langle V_i h_j \rangle_{model} \quad (5)$$

where  $\epsilon$  is learning rate.

Given a randomly selected training image,  $\mathbf{V}$ , the binary state,  $\mathbf{h}_j$ , of each hidden unit,  $j$ , is set to 1 with probability:

$$p(h_j = 1 | \mathbf{v}) = \sigma(b_j + \sum_i v_i w_{ij}) \quad (6)$$

Where  $v_i h_j$  is then an unbiased sample and  $\sigma(x)$  is the logistic sigmoid function given by:

$$\sigma(x) = \frac{1}{1 + \exp(-x)} \quad (7)$$

Because there are no direct connections between visible units in an RBM, it is also very easy to get an unbiased sample of the

state of a visible unit, given a hidden vector by using:

$$p(v_j = 1 | \mathbf{h}) = \sigma(a_j + \sum_i h_i w_{ij}) \quad (8)$$

Once binary states have been chosen for the hidden units, a reconstruction is produced by setting each  $v_i$  to 1 with a probability given by equation 8 and the change in a weight then given by equation 5 above is the final weight change using the reconstruction and the given data.

**Network Architecture:** The proposed network architecture consists of a 900 input features each having binary values that are obtained from segmented character images normalized to 30x30 windows. The number of output nodes or units is determined by the number of unique classes, in our case the number of unique characters in Geez alphabet are 26.

However, as will be described in section 5.2 we have only 24 class so the number of output nodes is made to be 24. In deep neural networks the number of hidden layers is hard to decide; in our system we will try experimentally to set it empirically that give better result. The basic architecture of the network is shown in Figure 2.

During designing of the neural network the number of different parameters of the network need to be decided. The model parameters that are required for the proposed network are described below. The values used for some parameters are typical values used in research [25] and others tuned during experimentation.

Number of neurons in the hidden layer: number of processing unit or nodes in the hidden layer.

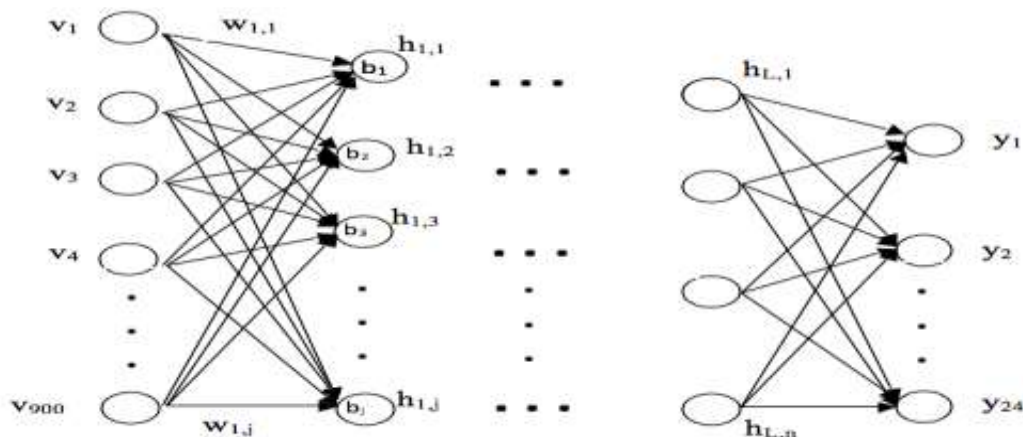


Figure 2: Architecture of the proposed deep network with 900 input, L hidden and 24 nodes of layers

**Learning rate:** Training parameter that controls the size of weight and bias changes in learning of the training algorithm. Recommended value: Real Domain: [0, 1] and its typical value: 0.3, Batch size: the number of training instance per batch. The typical value depends on the training data.

**Momentum:** momentum simply adds a fraction  $m$  of the previous weight update to the current one. The momentum parameter is used to prevent the system from converging to a local minimum or saddle point. A high momentum parameter can also help to increase the speed of convergence of the system. However, setting the momentum parameter too high can create a risk of overshooting the minimum, which can cause the system to become unstable. A momentum coefficient that is too low cannot reliably avoid local minima, and can also slow down the training of the system. Recommended value: Real Domain: [0,1] typical value: 0.9.

**Training epoch:** when this value is zero it means train by epoch, and when the value is one means train by minimum error. Recommended value: integer Domain: [0,1] and typical value is 1.

**Epoch** determines when training will stop once the number of iterations exceeds epochs. When training by minimum error,

this represents the maximum number of iterations. Value Selection domain: Integer Domain:  $[1, \infty)$ . The values practically used are as low as 50 and as high as tens of thousands. The following steps are our gross steps used to train deep neural network.

Pre-training one layer at a time in a greedy way; using unsupervised learning at each layer in a way that preserves information from the input and disentangles factors of variation; Fine-tuning the whole network with respect to the ultimate criterion of interest.

Each RBM layer is trained to maximize the product of probabilities assigned to some training set  $V$  (a matrix, each row of which is treated as a visible vector  $v$ ) as given by:

$$\arg \max_w \prod_{v \in V} P(v) \tag{9}$$

Or equivalently, to maximize the expected log probability given by:

$$\arg \max_w E[\sum_{v \in V} \log P(v)] \tag{10}$$

where  $\arg \max$  is the argument of the maxima, the probability of the input vector is maximum at the given weight during training.

The algorithm most often used to train RBMs, that is, to optimize the weight vector, is the contrastive divergence (CD)

algorithm as proposed by Hinton. The algorithm performs Gibbs sampling and is used inside a gradient descent procedure to compute weight update [15]. For computational simplicity and since it is the most widely used approach, we have used single-step contrastive divergence (CD-1) procedure which is given in the following steps:

1. Take a training sample  $v$ , compute the probabilities of the hidden units and sample a hidden activation vector  $h$  from this probability distribution.
2. Compute the outer product of  $v$  and  $h$  and call this the positive gradient.
3. From  $h$ , sample a reconstruction  $v'$  of the visible units, then resample the hidden activations  $h'$  from this. (Gibbs sampling step)
4. Compute the outer product of  $v'$  and  $h'$  and call this the negative gradient.
5. Let the weight update to  $w_{i,j}$  be the positive gradient minus the negative gradient, times some learning rate as given here with equation 11:

$$w_{i,j} = \epsilon (vh^T - v'h'^T) \quad (11)$$

The update rule for the biases  $a$  and  $b$  is defined analogously.

After each layer of RBM consisting of pairs of layers (visible and hidden) are training using RBM, finally the whole network is fine tuned in supervising manner using soft-max function criteria. The soft max activation function is useful predominately in the output layer [25]. Softmax function converts a raw value in to a posterior probability.

## Implementation Details

The proposed system is implemented in the following way:

**For Dataset Preparation Methods:** The programs are being implemented using MATLAB 2010 starting from image conversion to grey scale to the segmentation of individual characters from images.

**For DBNs:** We have used and customized deep learn tool box which is an open source MATLAB 2014 library for training the network and to make the tests.

**Experimental Setup:** A laptop computer with 3GB memory, Intel core i3 2.3GHz 3MB L3 Cache having windows 7 operating systems was used to conduct the experiment and a Sony digital camera with 16MP was used for image acquisition.

### TEST RESULTS OF THE DBN CLASSIFIER

To the best of our knowledge, since there is no other research result in ancient Ethiopic manuscripts, it was very difficult to present the comparison of the selected system with other recognition algorithms. Discussion and analysis of results are mostly based on percentage accuracy.

### Results of Dataset Preparation Methods

These steps are only used for an automatic preparation of the dataset for our training and we haven't made performance evaluations on these methods. The first step in preprocessing is converting the input color image in to gray scale image. We used the MATLAB function `rgb2gray` to get the gray scale image. The result of this function is shown in Figure 3.

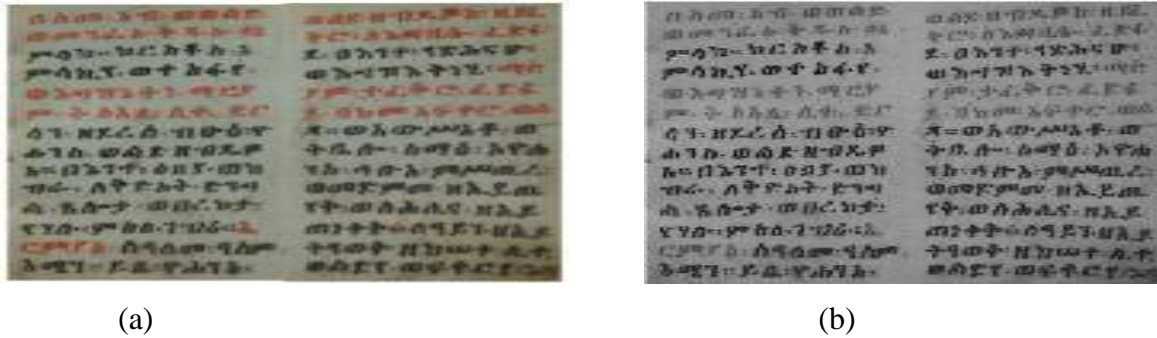


Figure 3: Output of RGB to gray scale conversion: (a) color image – left (b) gray image– right

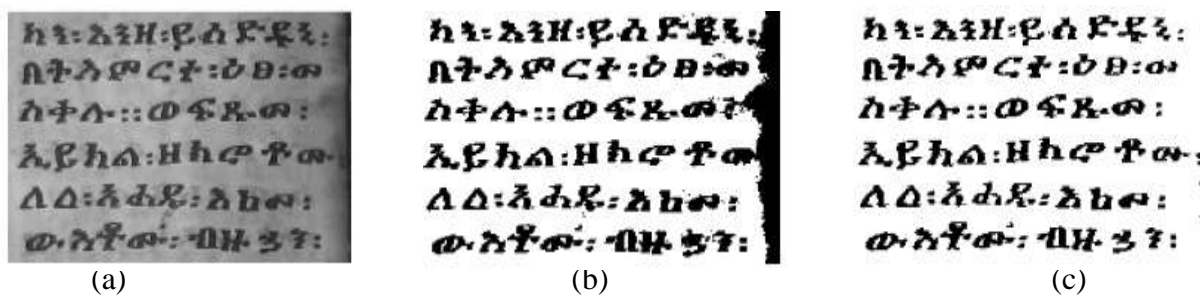


Figure 4: Output of binarization: (a) gray scale image (b) binarization using Otsu (c) binarization using hybrid

We have gotten better result using hybrid binarization technique. The comparison of the Otsu and the hybrid techniques are given in Figure 4. Ethiopic manuscripts are written in elegant format, by making straight lines as base line for writing each line of text on white codex, so it can be said that this does not create local skew

problem. The only skew problem detected is during taking picture of Ethiopic manuscripts using digital camera or during scanning, which is global skew problem. In many document analysis problems, skew angles as high as 23 degrees are observed. We have applied skew detection and correction on each image document as shown in Figure 5.

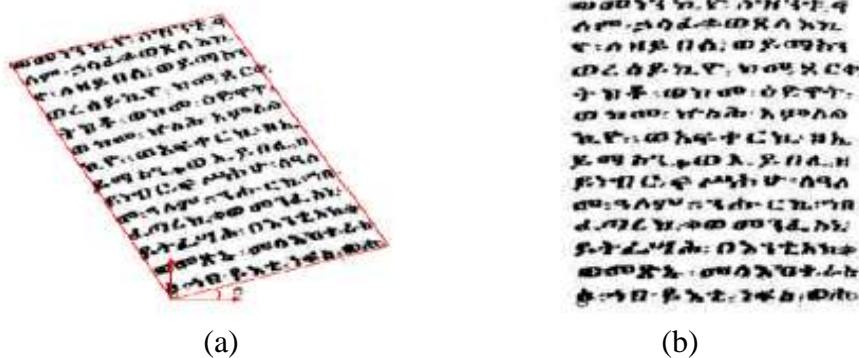


Figure 5: Output of skew detection: (a) skewed image (b) deskewed image

For segmenting lines and characters in images, vertical (Y histogram) and horizontal (X histogram) projections are implemented respectively. The result of vertical projection for a sample page is

shown in Figure 6. As shown in the figure, the lines of the sample images are segmented accurately. The algorithm was tested with a number of document pages, and all tests produced perfect results; this

shows that the selected algorithm works very well.

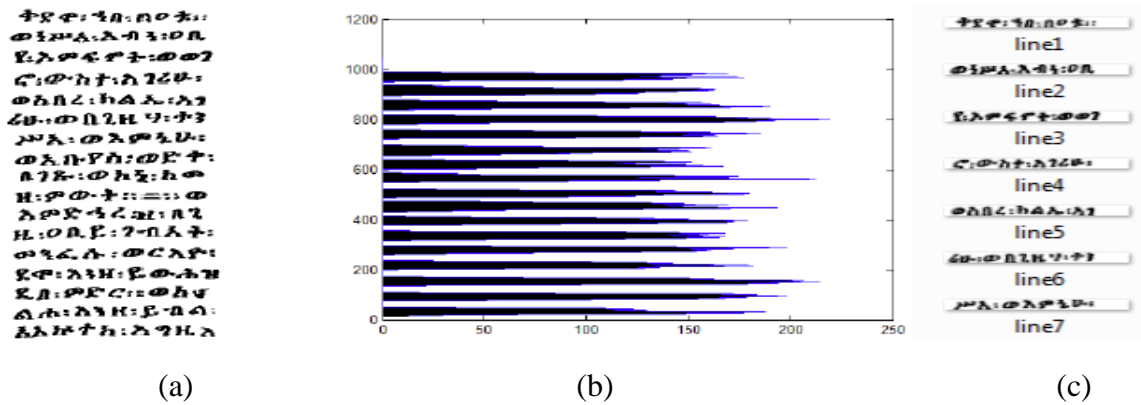


Figure 6: Output of line segmentation (a) input image (b) Y histogram (c) segmented line

One limitation of line segmentation observed was that it segments two lines together if there are characters written over a word, between two lines, usually placed as correction when mistakes were made

during writing, as shown in the first two lines of a document page and lower part of its histogram Figure 7 (a) and (b) respectively In this case, the algorithm will segment the two lines incorrectly as a single line, as shown Figure 7(c).

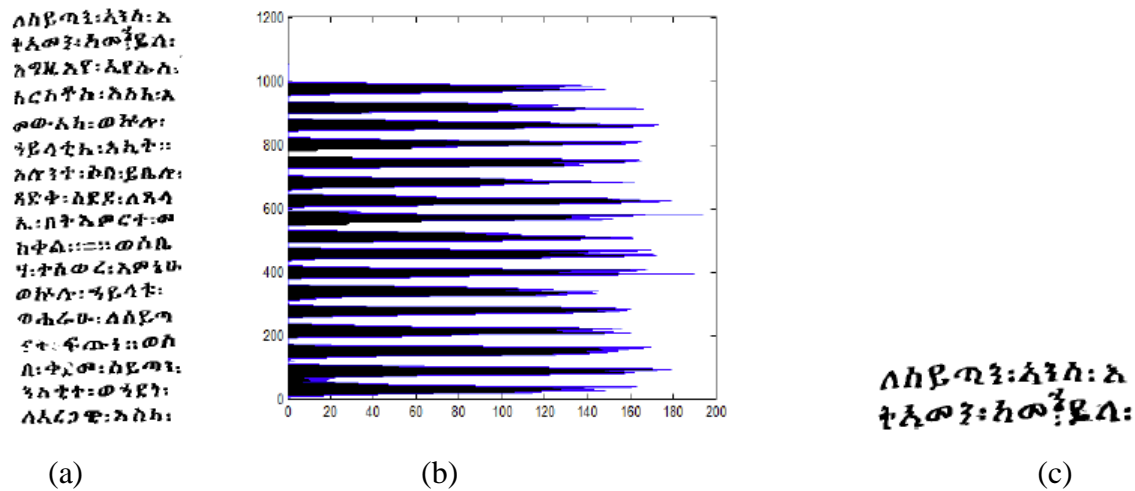


Figure 7: Line segmentation error (a) input image (b) Y histogram (c) error segmented

From the given segmented line, each of the characters is extracted automatically using the X histogram. Figure 8(c) shows sample results of segmented characters from segmented lines (Figure 8(a)) using the horizontal histogram projection (Figure 8(b)). The result shows that each character is segmented accurately.

single character is split into two characters due to opening problem, as shown in Figure 9(d).

Another challenge is when a character has unconnected component, in which case, a

After dataset preparation methods are done, we have gotten dataset which consists of images of 7065 segmented characters extracted from 200 pages of input images of ancient Ethiopic manuscripts. Out of the total segmented characters, 24 out of the 26 Geez base characters with their derived characters

were found. The remaining two characters “አ” and “ጥ” appeared four times and none respectively.

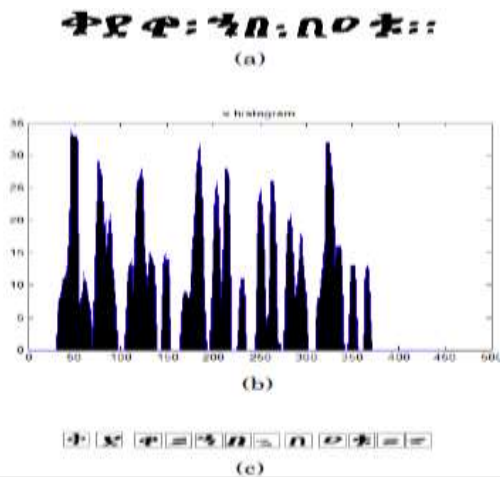


Figure 8: Output of character segmentation (a) input image (b) X histogram (c) segmented characters

These two problems created error in character segmentation results. However, it was observed that this happens rarely because Ethiopic scripts are written by preserving the space between characters.

The frequencies of some of the derived characters were also small and were not equally distributed compared to the frequency of the base characters. Base characters appeared on average from 100 up to 165. Due to this reason, the dataset consisted of only base characters and the frequency was set to 100 for each character.



Figure 9: Error in output segmentation: (a) input image (b) segmenting two characters as one (c) input image (d) segmenting one character by splitting in to two characters

Each character was labeled taking 100 characters for each base character forming one similar class, and totally the dataset contains 2400 base characters for training and testing. Among the total data set 70% was used for training and 30% used for testing the system.

**Result of Training and Recognition Test**

The proposed deep neural network was trained and tested by using the following experimental setup:

The training set is provided as an input image, arranged in 1680 x 900 pixel mat file and 1680 x 1 label mat file. Each input image character is 30x30pixels, so number of input neurons is 900.

Number of characters for classification is 24, so the number of output neurons is set to 24

Learning rate was set to 0.3, batch size was set to 50 and momentum was set to 0.5

Epoch was set to be variable; values of 50, 100, and 150 were tested

Number of hidden layers and number of neurons in each layer was also set to from 2 to 4 and different values were set and tested for each.

The pre-training algorithm for the network model used was RBM and final fine tuning used was soft max. Finally the proposed network was tested using 720 x 900 pixel mat file of 720 characters.

Various experiments were done by using different values of epoch, number of hidden layer, and number of hidden units. The recognition error is the ration of number of misclassified characters to total number of characters in the test dataset. Accuracy is also the ratio of number of correct classification to total number of characters.

Table 1: Recognition error with two hidden layers

Epoch	Two Hidden Layers		
	100 units	200 units	300 units
50	0.141667	0.0875	0.08333
100	0.113889	0.076389	0.065278
150	0.097222	0.070833	0.063889

The results of recognition errors for different hidden layers are summarized in Tables 1, 2 and 3. Tables 1 to 3 show the recognition error using 2, 3, and 4 hidden layers each with 100, 200, and 300 units for 50, 100, and 150 epochs respectively. It can be observed that, generally, the recognition error decreases as the number of epochs increases. This is expected, since the network enforces what it has learnt in each epoch. However, the rate of decrement of the error is slow, as can be deduced from the difference between two successive epochs. This again indicates that the error decrease will come to a point where no more decrease is observed, in which case the training is said to over fit.

Comparing the error values in the three tables, smallest recognition error (that is

0.0625 or 93.75% accuracy) was obtained for a network with three hidden layers, 300 hidden units and 150 epochs (See Table 2). It is also observed that in the four layers, at 150 epochs with 300 units the error is larger than the 2 and 3 hidden layers with the same number of epochs.

Table 2: Recognition error with three hidden layers

Epoch	Three Hidden Layers		
	100 units	200 units	300 units
50	0.16667	0.098611	0.079167
100	0.151389	0.090278	0.072222
150	0.141667	0.06944	0.06250

Table 3: Recognition error with four hidden layers

Epoch	Four Hidden Layers		
	100 units	200 units	300 units
50	0.218056	0.129167	0.105556
100	0.179167	0.10000	0.08750
150	0.172222	0.0875	0.077778

The above graph illustrates the overall comparison of the three network types of layers i.e. between 2, 3 and 4 hidden layers. At 50 epochs the 4 hidden layers with 100 neurons gets larger error than 2 and 3 layers. When the number of epochs increased, at 100 epochs, the error at all layers become small. However, at 150 epochs the error using 4 layers starts to increase again, may be due to over fitting. Therefore the final good result relays on 3 layers, 300 neurons with 150 epochs with 93.75% accuracy.

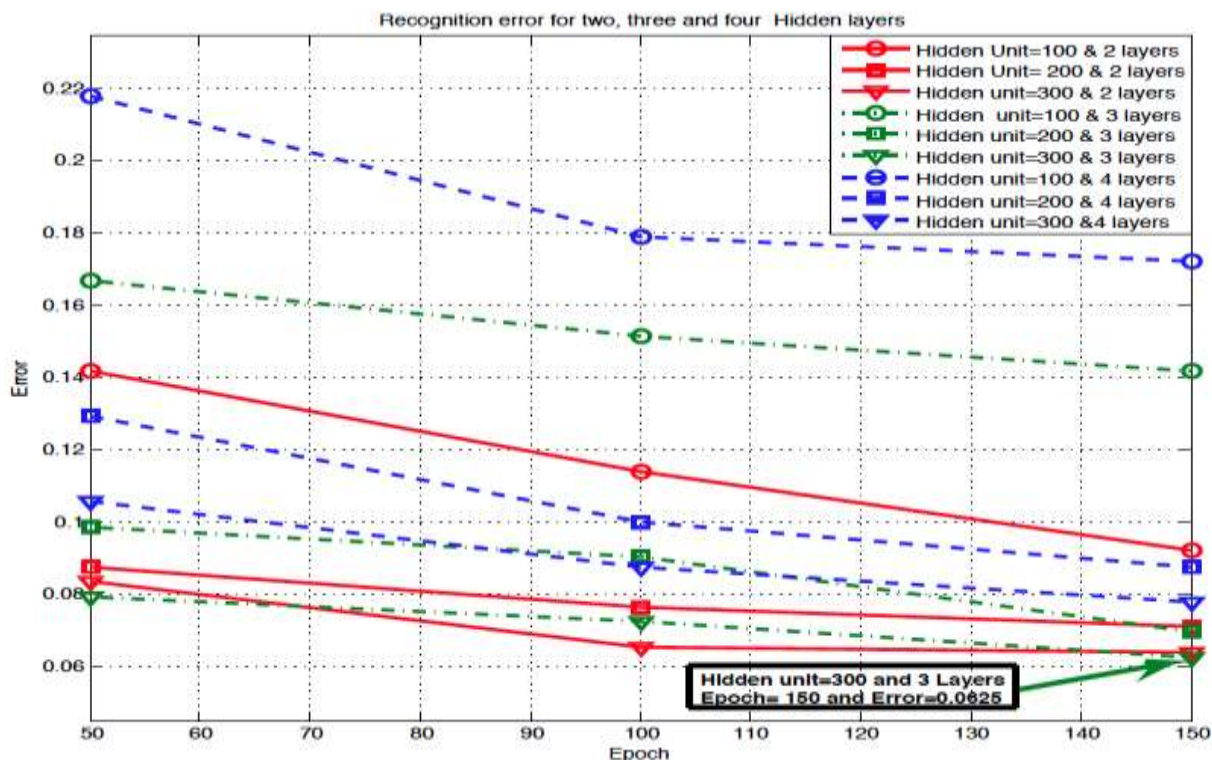


Figure 10: Graph of overall recognition error with two, three and four layers

**Comparison with other similar works**

To compare the results of our approach with others, three research results mentioned in [3, 10, and 11] were selected. The selection criteria was based on the fact that the researchers used handwritten Amharic text, otherwise since the documents are not very similar to ancient Ethiopic manuscripts we found it hard to make exact comparison. Table 4 shows rough comparison of the selected research

results with that of ours.

As the comparison table shows the recognition rate of our system produced better results. The result obtained by the HMM system is comparable to ours because it was obtained with considerably smaller number of training words of good quality documents.

Table 4 Performance comparison of different approaches

Research	Document type	No. of pages or characters used in dataset	Recognition Rate
HMM based [3]	Modern Handwritten	100 words	93% (for good quality document)
		10,932 words	76%(for good quality document)
Writer Independent [26]	Church document	114 pages	87%
Lexicon Based [10]	Modern handwritten	307 pages	87% (top -5 choices)
<b>Our approach</b>	<b>Ancient manuscript</b>	<b>200 pages</b>	<b>93.75%</b>

## CONCLUSION AND FUTURE WORKS

This research work aimed to propose a system for recognition of Ancient Ethiopic manuscript CR using DBNs. The recognition system consists of data acquisition, preprocessing, segmentation, and classification and testing the recognition. We have prepared dataset consisting of 24 base characters of 100 frequencies; totally 2400 characters are prepared in mat file. Among the total characters 1680 used for training and 720 characters used for testing the system.

The classifier network (DBN) was trained using a data set of Geez characters using RBM greedy layer wise unsupervised training and Soft max supervised fine tuning for the final RBM layer.

In our experiment we have tested to show the performance of DNN by varying a number of parameters. All the three test scenarios showed comparable and similar results (not less than 92%) even though the best result obtained was 93.75% accuracy using 3 hidden layers with 300 hidden neurons at 150 epochs.

Even though the dataset frequency for each character was low to make very good training, we have seen that DBN is an excellent technique for ancient handwritten document CR with very good accuracy.

Even though we have shown that DBNs are performing very well in recognition accuracy for ancient manuscript characters recognition task, there are issues that can addressed in future research activities. Some of these issues are:

In order to design a complete recognition system for ancient Ethiopic manuscript characters, a complete dataset should be prepared that consists of the entire Geez alphabets by collecting several manuscripts from different sources. The network model parameters of the DBNs

can be varied and experimented for optimal performance in the accuracy of the recognition.

Due to computational resource limitation, we have only trained the system to a maximum epoch of 150. By including regularization methods into the training to avoid over fitting, the network can be trained for more number of epochs and its performance can be improved with larger and computationally capable environment.

The recognition is highly dependent on the accuracy of pre-processing and segmentation for automatic manuscript recognition task. Additionally, we haven't included automatic text region detection to exclude non-text areas and segmenting multi-column text areas. Therefore, the research can be extended to include text area detections and improvements of preprocessing including image quality enhancing along with high performance segmentations.

## REFERENCES

- [1].Graves, Alex, et al, "Unconstrained on-line handwriting recognition with recurrent neural networks," *Advances in neural information processing systems*. 2008.
- [2].Prasad, Kauleshwar, et al, "Character recognition using matlab's neural network toolbox," *International Journal of u-and e-Service, Science and Technology* 6.1 (2013): 13-20.
- [3].Assabie, Yaregal, and Josef Bigun, "Offline handwritten Amharic word recognition," *Pattern Recognition Letters* 32.8 (2011): 1089-1099.
- [4].Gupta, Anshul, Manisha Srivastava, and Chitrlekha Mahanta, "Offline handwritten character recognition using neural network," *2011 IEEE International Conference on Computer Applications and Industrial Electronics (ICCAIE)*. IEEE, 2011.

- [5]. Scelta, Gabriella F., and Pilar Quezzaire-Belle, "The Comparative Origin and Usage of the Ge'ez writing system of Ethiopia," *Unpublished manuscript, Boston University, Boston*. Retrieved July 25 (2001): 2009
- [6]. Assabie, Yaregal, "Optical Character Recognition of Amharic text: an Integrated Approach," Diss. Addis Ababa University, 2002.
- [7]. Meshesha, Million, and C. V. Jawahar, "Optical character recognition of Amharic documents," *African Journal of Information & Communication Technology* 3.2 (2007).
- [8]. Cowell, John, and Fiaz Hussain, "Amharic character recognition using a fast signature based algorithm," *Proceedings on Seventh International Conference on Information Visualization, 2003. IV 2003*. IEEE, 2003.
- [9]. Yuan, Aiquan, et al, "Offline handwritten English character recognition based on convolutional neural network," *2012 10th IAPR International Workshop on Document Analysis Systems*. IEEE, 2012.
- [10]. Assabie, Yaregal, and Josef Bigun, "Lexicon-based offline recognition of Amharic words in unconstrained handwritten text," *2008 19th International Conference on Pattern Recognition*. IEEE, 2008.
- [11]. Assabie, Yaregal, and Josef Bigun, "Writer-independent offline recognition of handwritten Ethiopic characters," *Proc. 11th ICFHR* (2008): 652-656.
- [12]. Diem, Markus, and Robert Sablatnig, "Recognizing characters of ancient manuscripts," *Computer Vision and Image Analysis of Art*. Vol. 7531. International Society for Optics and Photonics, 2010.
- [13]. Shah, Mansi, and Gordhan B. Jethava, "A literature review on hand written character recognition," (2013).
- [14]. Bengio, Yoshua, et al, "Greedy layer-wise training of deep networks," *Advances in neural information processing systems*. 2007.
- [15]. Bengio, Yoshua, "Practical recommendations for gradient-based training of deep architectures," *Neural networks: Tricks of the trade*. Springer, Berlin, Heidelberg, 2012. 437-478.
- [16]. Ramappa, Mamatha Hosalli, and Srikantamurthy Krishnamurthy, "Skew detection, correction and segmentation of handwritten Kannada document," *International Journal of Advanced Science and Technology* 48 (2012).
- [17]. Sahu, Vijay Laxmi, and Babita Kubde, "Offline handwritten character recognition techniques using neural network: A review," *International journal of science and Research (IJSR)* 2.1 (2013): 87-94.
- [18]. Dave, Namrata, "Segmentation methods for hand written character recognition," *International journal of signal processing, image processing and pattern recognition* 8.4 (2015): 155-164.
- [19]. Dongre, Vikas J., and Vijay H. Mankar, "Devnagari document segmentation using histogram approach," *arXiv preprint arXiv: 1109.1247* (2011).
- [20]. Anupama, N., Ch Rupa, and E. Sreenivasa Reddy, "Character segmentation for Telugu image document using multiple histogram projections," *Global Journal of Computer Science and Technology* (2013).
- [21]. Arica, Nafiz, and Fatos T. Yarman-Vural, "An overview of character recognition focused on off-line handwriting," *IEEE Transactions on*

- Systems, Man, and Cybernetics, Part C (Applications and Reviews)* 31.2 (2001): 216-233.
- [22]. [Online]. Available: <http://deeplearning4j.org/neuralnet-overview.html>, accessed on 01/17/2016.
- [23]. Larochelle, Hugo, et al, "Exploring strategies for training deep neural networks," *Journal of machine learning research* 10. Jan (2009): 1-40.
- [24]. Hinton, Geoffrey E, "A practical guide to training restricted Boltzmann machines," *Neural networks: Tricks of the trade*. Springer, Berlin, Heidelberg, 2012. 599-619.
- [25]. Wikibooks, "Artificial neural network." [wikibooks.org](http://wikibooks.org), 2014. (Accessed on March 2016).
- [26]. Getu, Siranesh, "*Ancient Ethiopic Manuscript Recognition Using Deep Learning Artificial Neural Network*," Diss. Addis Ababa University, 2016.

# EFFECTS OF ETCHING PROCESS INACCURACY IN THE MALFUNCTIONING LEVEL OF PCB CIRCUITS - A SIMULATION BASED ANALYSIS

Hgigat Aregawi <sup>1</sup>, Mohammed Abdo <sup>2</sup>

<sup>1</sup>Department of Computer Science and Engineering, Mekelle Institute of Technology, Mekelle University, Mekelle, Ethiopia. Email: hgigat.aregawi@mu.edu.et

<sup>2</sup>School of Electrical and Computer Engineering, Addis Ababa Institute of Technology, Addis Ababa University, Addis Ababa, Ethiopia, Email: mohammed.abdo@aait.edu.et

## ABSTRACT

*The PCB is a mechanical base used for interconnection of electronic components. In PCB manufacturing industry, the quality and reliability of circuits is highly dependent upon the accuracy of the manufacturing processes. Among the manufacturing processes, etching is the most sensitive process and needs more accuracy. The etching inaccuracies cause severe problems that may result in degradation of circuit performance and malfunctioning of circuits.*

*In this research the levels of effects of etching manufacturing process inaccuracies on the malfunctioning of PCB circuits is investigated and analysed. The effects of the process inaccuracies on circuits as well as how the process is related with the affecting parameters are addressed. A four-layer multilayer board is considered for the study and the software selected to study the effects of manufacturing inaccuracies is OrCAD PCB designer. Schematic development, PSpice simulation and layout design are made for selected circuits to study the effects of the etching inaccuracies. According to the results obtained; inaccurate etching results in either larger or smaller width of traces, leaves unwanted conductive materials, and creates unnecessary holes or open circuits and short circuits.*

*In the over etching scenario, when the over etching effect is increased and results in 14.36-ohm resistance, output voltage drops from 48mV to 22mV. For the open circuit scenario, it results in zero output voltage. Similarly, for the short circuit case which is*

*the case of under etching, the output result shows 1.8nV which is very small and it can be considered as zero output voltage. For capacitive effects, the output becomes very small (140uV), unstable and oscillating. For the combined resistive and capacitive effects, the output is nearest to zero (65uV) and oscillating.*

**Keywords:** *etching, inaccuracies, OrCAD, over etching, PCB, under etching,*

## INTRODUCTION

Printed circuit board (PCB) is a device used for mounting electronic components and providing electrical interconnections to the circuits that are found in electronic or electrical devices and systems [1,2].

PCB is constructed from an insulating material placed as the core and conducting material i.e. copper coated on the surfaces. This copper plating is etched away to form the actual copper pads and connection traces on the board surfaces as part of the board manufacturing process [3, 4, 5]. There are three major types of printed circuit board constructions namely, single-sided, double-sided and multi-layered. Single-sided boards are with copper pads and traces on one side of the board and the components are on one side of the substrate.

When the number of components becomes too many for a single-sided board, a double-sided board may be used in which there are copper pads and traces on the top and bottom sides of the board. Electrical connections between the circuits on each side are made by drilling holes

through the substrate in appropriate locations and plating the inside of the holes with a conducting material. The third type, a multilayered board, has a substrate made up of layers of printed circuits separated by layers of insulation. It is designed with copper pads and traces on top and bottom of board with a variable number of internal copper layers with traces and connections. The components on the surface connect through plated holes are drilled down to the appropriate circuit layer [6].

A multilayer board consists of a number of layers of dielectric material that has been impregnated with adhesives, and these layers are used to separate the layers of copper plating. All of these layers are aligned and then bonded into a single board structure under heat and pressure. Multilayer boards with 48 or more layers can be produced with today's technologies [7].

The exposed inner layers are developed in a 1% sodium carbonate solution, which removes resist from areas that were not hardened (polymerized) by the light. In Inner Layer Etching copper is chemically removed from the areas where the dry film is removed. This creates the copper pattern that matches the film pattern.

The traditional process of exposing the copper and other areas unprotected by the etch resist film to a chemical that removes the unprotected copper, leaving the protected copper pads and traces in place; newer processes use plasma/laser etching instead of chemicals to remove the copper material, permitting finer line definitions. In Resist Stripping, developed dry-film resist is chemically removed from the panel leaving the copper on the panel.

In this traces, pads, ground plane and other design features are exposed. Finally, Automated Optical Inspection (AOI) is done after resist stripping. Inner layers are then inspected against design rules using data from the Gerber files. After inspection, the panels are chemically coated with oxide to improve adhesion of the copper surface [8, 9, 10].

In this paper, the focus of our study is with multilayer PCB manufacturing processes, and we chose a four layer which is the simplest multilayer board for our study. However, we have used simpler circuits with components consisting of less than 22 which can be even implemented with a single sided board if the design is to be done merely based on complexity. Therefore, our interest is to study on multilayer board, and we chose four layer to illustrate etching inaccuracy effects in multilayer boards.

### **PROBLEM DESCRIPTION**

PCB manufacturing processes must be accurate to minimize the failure of circuits after final production. To avoid the possible failures in PCB circuits, analysis of effects of individual process inaccuracies on the level of malfunctioning of circuits is important. It helps give awareness in making processes accurate and avoid the possible causes of PCB process inaccuracy.

The study of manufacturing inaccuracies and their effects in circuits is very important as it paves way for making processes more accurate and building robust PCB circuits and then meets customer satisfaction.

As it is very well known, the inaccuracies of the processes followed by the manufacturing technology are the main reasons for circuit malfunctioning. Therefore, in this paper the etching process inaccuracies along with the factors affecting it and the corresponding effects on the level of malfunctioning of circuits are identified and discussed.

### **ETCHING RPROCESS INACCURACIES AND AFFECTING PARAMETERS**

PCB circuits can malfunction due to the inaccurate etching of traces in the etching manufacturing process. The inaccurate etching results in either more width of copper (more width of traces than normal) or small width of traces (small copper). In addition, the inaccurate etching process leaves unwanted conductive materials, creates unnecessary holes or open circuits. This inaccuracy of PCB etching which results in thicker width of traces

and unwanted copper on the board may result in short circuits.

On the other hand, the excessive etching which happens in thinner traces and gaps may result in open circuits. Those defects are called fatal defects. There are also other forms of defects due to the inaccurate etching process which doesn't directly cause malfunctioning of PCB circuits. Those types of irregularities form neither short circuits nor open circuits immediately. Due to the inaccurate size of traces and holes on PCB circuits, the performance of the circuit is compromised. Such defects are called potential defects.

Since copper is not a perfect conductor, the inaccurate etching or inexact sizes of traces and holes (smaller sizes) presents a certain additional amount of impedance to current flowing through it, this additional impedance results in extra energy lost in the form of heat [11,12]. Moreover, when signal traces are smaller in width than normal, signal loss in the circuit occurs. There is a need to study the combined effects of all other parameters on etching. The parameters that influence the accuracy of etching process are material removal rate, etch factor, undercut, and concentration of etchant, etching time and etchant temperature.

An optimal parameter combination for maximum material removal rate and undercut within the range selected control parameters are obtained by using analysis of variance [13]. In order to obtain the effect of the etching parameter on etching performance for each different level, the average response of each fixed parameter and level for each etching performance are summed up. The undercut increases with increase concentration.

The affecting parameters for undercut are temperature, concentration and time. Out of these temperature and time are the most significant parameters on undercut.

When copper is etched, the edge of the copper trace is neither a completely smooth nor a vertical wall. The roughness called the edge definition occurs because of mask resolution limitations, non-uniformity of the acid circulation, gas bubbling during etching and etc. The wall will have a slight angle to it because as the acid begins to work its way into the exposed copper a sidewall begins to form, which also is attacked by the acid, and the copper near the etch resist begins to be removed under the mask. This effect is called etch back or undercutting.

Parasitic impedance in high-speed PCBs destroys circuit performance [14]. PCB parasites are in the form of undesired capacitors, inductors and resistors embedded within the PCB.

The standards considered in PCB design, the size of trace-to-trace width is a minimum of 3.5MIL, width of trace to hole is a minimum of 5MIL, and perpendicular traces are not allowed. If the sizes are below the minimum levels, short circuits and cross talks may happen in the given circuits.

## METHODOLOGY

In this section the method of analysing the effects of inaccuracies of PCB manufacturing processes on the level of malfunctioning of circuits are discussed. Because of the unavailability of the PCB manufacturing laboratory as the laboratory set-up is not yet established, a simulation based analysis is considered in this paper. The type of application software used for simulation as well as the procedures followed to study the effects are described.

### Software Requirement

The Software selected to study the effects of manufacturing inaccuracies is OrCAD PCB designer. Among other software's, OrCAD is

the appropriate one for this purpose because of the features it has starting from schematic capture to layout design. Schematic development, PSpice simulation and layout design are the main task of the OrCAD software in this research.

OrCAD capture is a PCB schematic designer tool. OrCAD Capture is applied for designing the schematic circuit selected for studying the effects, and OrCAD PSpice is an analog and digital simulator. It simulates a captured circuit so that its performance can be investigated.

OrCAD PSpice technology is seamlessly integrated with OrCAD Capture which is one of the most widely used schematic design solutions allowing to easily cross-probe between the schematic design and simulation plot results and measurements. This integration also allows to use the same schematic for both simulation exploration and PCB layout, reducing rework and errors.

### Implementation Procedures

The major PCB etching manufacturing process inaccuracies are considered for analysing and discussing the effects of manufacturing inaccuracies. The procedures followed to study the circuit effects of different scenario is given as follows.

- In the first step, appropriate circuit which is a two stage BJT amplifier is selected.
- The normal schematic circuit is captured on OrCAD PCB Capture.
- Simulation of the given circuits is done on OrCAD PSpice.
- A four-layer PCB layout is routed for the given schematic and the possible manufacturing inaccuracy scenarios are indicated on the circuit layout.
- Equivalent circuit model for the given increased scenario is developed

- Schematic capture incorporating circuit model for the inaccuracy scenario is done for the selected circuits.
- Difference in circuit performance and any circuit malfunctioning is observed

### EFFECTS OF ETCHING INACURACY

During etching process, the anomalies occurring on bare PCB could be largely classified in to two categories: one is excessive copper and missing copper. The incomplete etching process leaves unwanted conductive materials and forms defects like short-circuit, extra hole, protrusion, island and small space. Excessive etching leads to open circuit and thin pattern on PCB. In addition, some other defects such as missing holes, scratch, and cracks may exist on bare PCB.

For perfect etching case, the resistance of the tracks is assumed to be negligible. However, it has a considerable resistance value for the over etching scenario above. A formula for calculating the sheet resistance  $R$  of a copper trace, given the length  $Z$ , the width  $X$ , and the thickness  $Y$  is given by:

$$R = \frac{\rho Z}{XY} \quad (1)$$

Where  $\rho = 1.724 \times 10^{-6} \Omega \text{cm}$  is the resistivity of the copper.

Inaccurate etching can cause undesired signal output which is a decreasing effect. But the idea is that the effect of inaccuracy is an obstacle to getting the desired signal output. It makes the circuit fluctuate and deviate from the functionality it is designed for.

### Capacitive Effects

When the gap between two parallel traces is smaller than the standard spacing that should be between traces, capacitive impedance will be introduced across the traces and results in cross talk and unstable output.



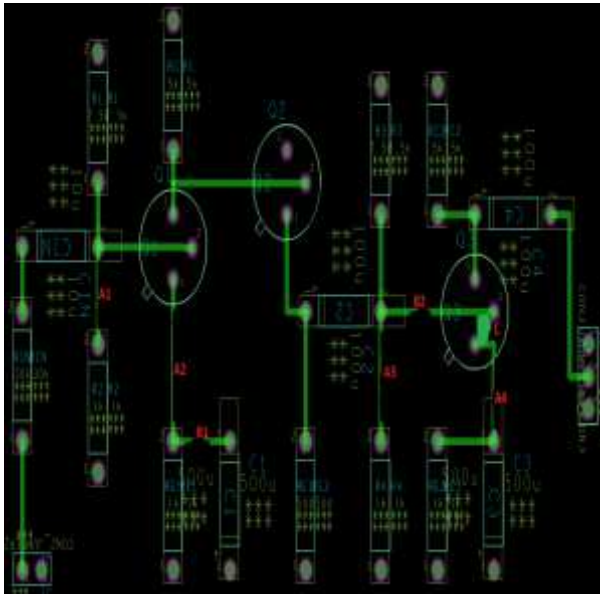


Figure 3: different etching inaccuracy scenarios

From Fig. 3, the general name for inaccuracy denoted by A1 is an over etching. This over etching scenario is modelled into a circuit to see the effect on circuit performance and malfunctioning as it is depicted in Fig. 4.

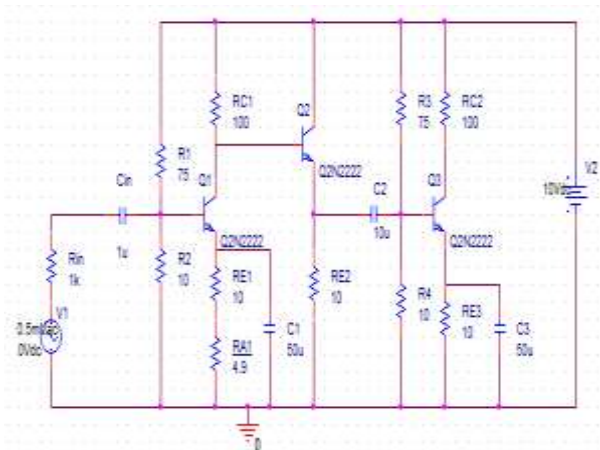


Figure 4: Equivalent circuit for over etching scenario

Fig. 5 depicts the frequency response of the circuit for different levels of over etching scenarios represented by A1 with the effect indicated by resistance  $R_{A1}$ . It shows that the gain is decreasing as  $R_{A1}$  keep increasing.

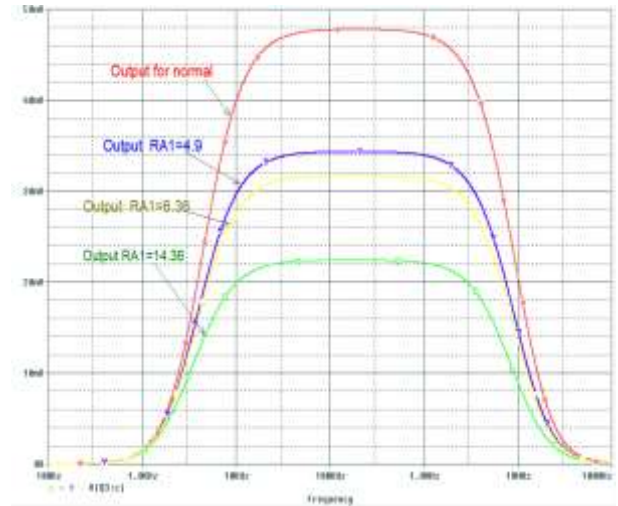


Figure 5: Frequency response for over etching scenario for different levels of RA1

**Open Circuit and Short Circuit Scenario**

The equivalent circuit for the open circuit scenario is shown in Fig. 6. As can be seen in the circuit, the input to transistor Q3 is floating (open) due to over etching.

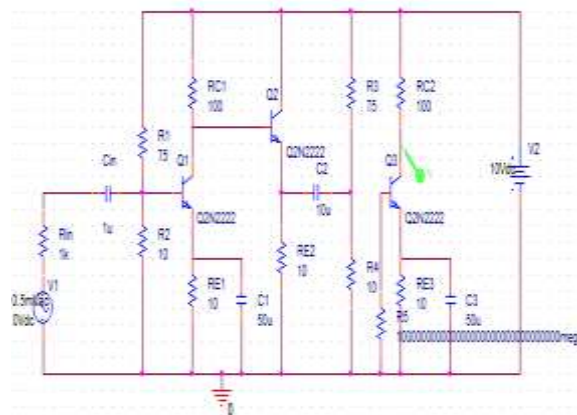


Figure 6: Equivalent circuit for open circuit scenario

The output of the circuit given in Figure 6 is depicted in Fig. 7. It shows that the effect of the open circuit scenario is fatal and it results in zero output.

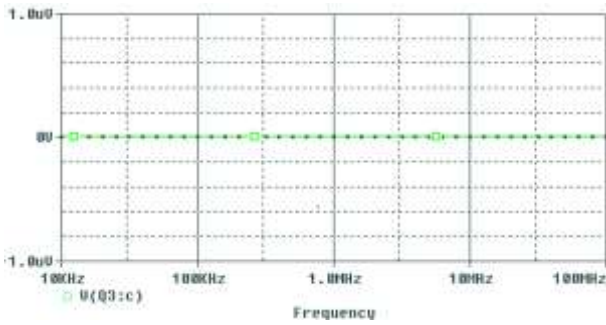


Figure 7: Frequency response for open circuit scenario

Fig. 8 shows the equivalent schematic for the short circuit scenario. It shows that the base and emitter of transistor Q3 are shorted together.

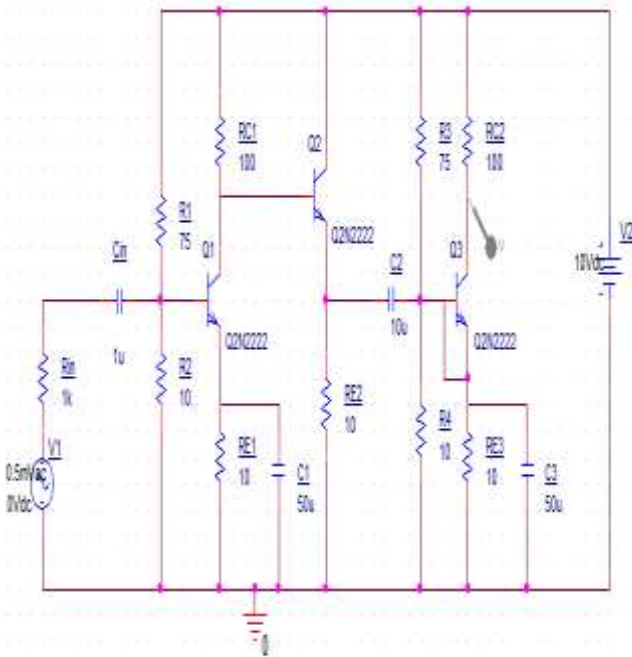


Figure 8: Equivalent schematic for short circuit scenario

Fig. 9 shows the simulation output for the short circuit scenario depicted in Figure 8. As can be seen from the figure, the output is diminished and very small as compared to the output of the normal circuit.

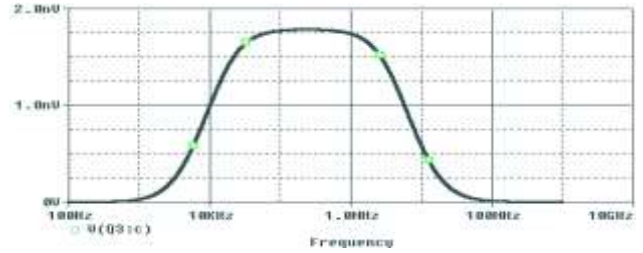


Figure 9: Frequency response for short circuit scenario

**Capacitive Effects**

Fig. 10 shows the equivalent circuit under the consideration of capacitive effects.

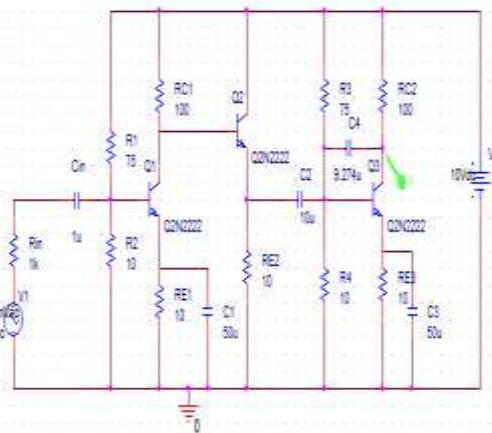


Figure 10: Equivalent circuit with capacitive effect

Fig. 11 shows the simulation output of the circuit depicted in Fig. 10 by considering different capacitive effects. As can be seen from the simulation output, cross talk or unstable output occurs over the frequency on which the expected output should be stable.

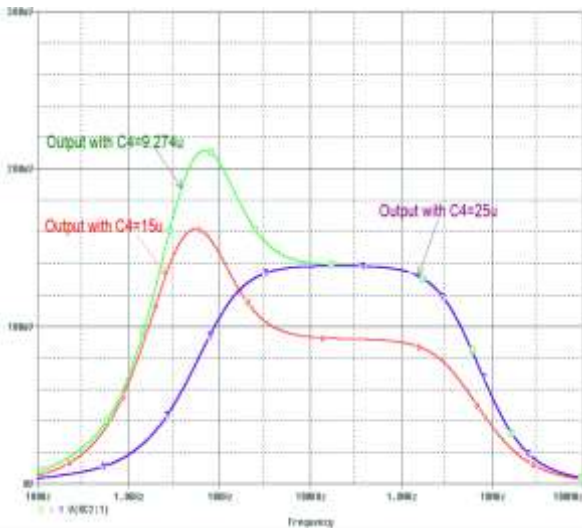


Figure 11: Frequency response for different capacitance values

When the capacitive impedance effect is 25uF, the output drops from around 50mV to 140uV and the output waveform looks like the waveform of the normal circuit. On the other hand, at lower capacitance values the output becomes unstable and gives a waveform with a different nature.

**Capacitive and Resistive Effects**

In this section, the capacitive effects due to wrong spacing between traces as well as resistive effects due to over etching are considered and the corresponding equivalent circuit is depicted in Fig. 12.

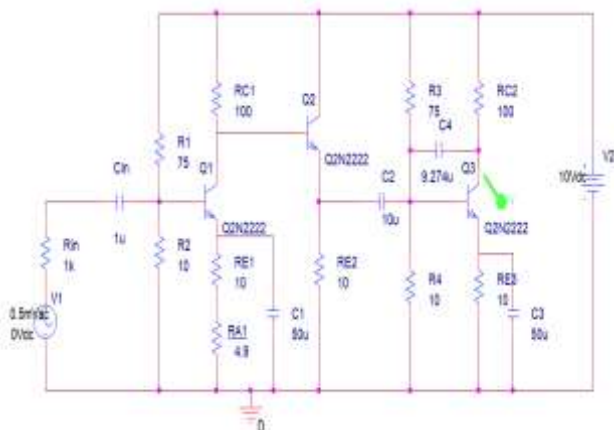


Figure 12: Equivalent circuit for capacitive and resistive effects

Fig. 13 shows the simulation result for the combined resistive and capacitive effects. As

can be seen in the figure, the output waveform results in instability and oscillations.

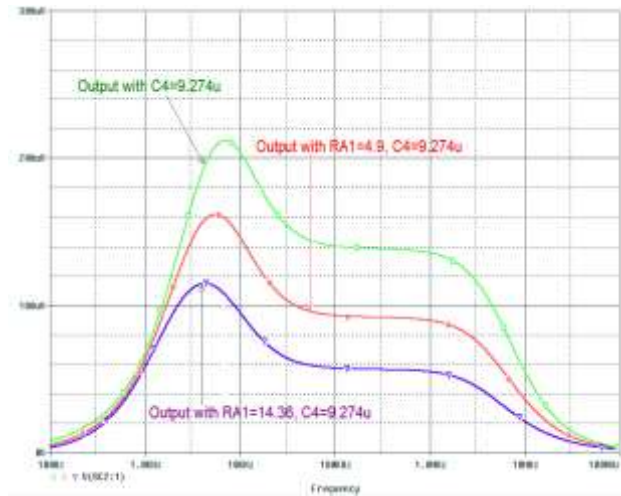


Figure 13: Frequency response for combined capacitive and resistive effects

**Analysis of effects with 4-bit ADC circuit**

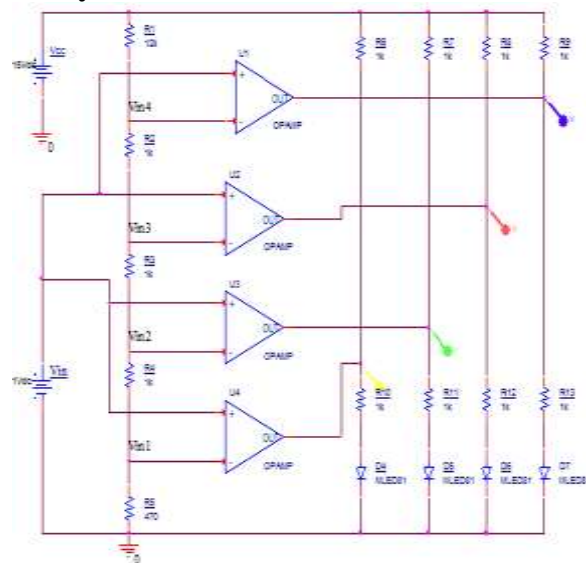


Figure 14: Implementation of 4-bit ADC

For the circuit depicted in Figure 14, we considered under etching scenario which results in short circuits, and the circuit with the effect produces no output which means the circuit totally mal functions. We also tried to analyse the over etching scenario for the circuit which finally results in open circuit. The equivalent circuit for the open circuit is depicted in Figure 15.

**CONCLUSIONS**

In this paper, simulations using OrCAD PSpice have been made to illustrate the possible effects on the different circuits caused by the possible manufacturing errors. Simulation results show that small reduction of widths of traces (over etching) results in small performance reduction of the given circuit. If the over etching rate is medium, then a medium performance reduction happens. For much larger over etching rate, there is a higher probability of totally malfunctioning of the circuit.

Table 1: Summary of simulation results

S/N	Type of defect	Resulting effect	Defect level	Output of circuit in (mV)	Remark of output
1	No defect	-	-	48	Normal
2	Over etching	Resistive	RA1=4.9Ω	34	
3	Over etching	Resistive	RA1=6.36Ω	32	
4	Over etching	Resistive	RA1=14.36Ω	22	
5	Open circuit	Resistive	R5= ∞	0	Zero
6	Short circuit	Short circuit	fatal	0.0018	Negligible
7	Over etching	Capacitive	C4=9.27 μF	0.140	Diminished & oscillating
8	Over etching	Resistive and Capacitive	RA1=14.36Ω, C4=9.27 μF	0.065	Very Diminished & oscillating
9	Under etching in ADC		severe	null	malfunction
10	Over-etching in ADC		severe	0101	Wrong output

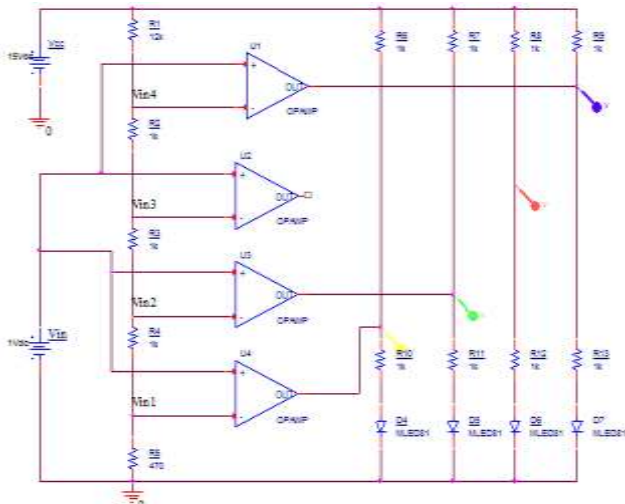


Figure 15: Equivalent circuit for open circuit scenario

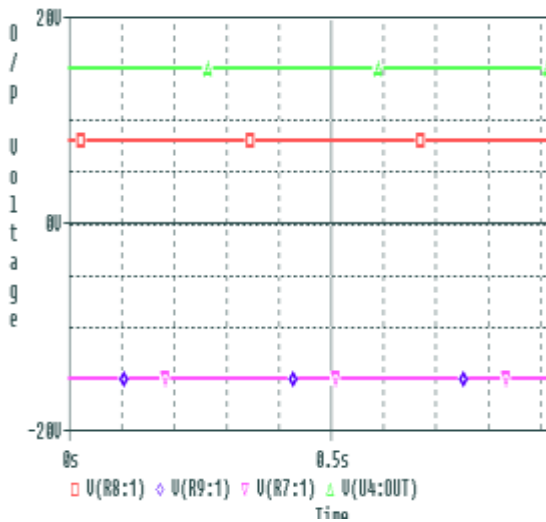


Figure 16: Output signal for open circuit scenario

As it is illustrated in Figure 16, the output for 1V input is 0101 instead of 0001 which is a wrong output due to open circuit effect.

**RESULTS**

Table 1 summarizes the simulation results. The table shows the simulation output for the non-defective (normal) circuit and defective circuits by considering different inaccuracy scenarios and defect levels. The output is obtained by giving the same input to all types of circuits.

In the over etching scenario, when the over etching effect is increased and results in 14.36-ohm resistance, output voltage drops from 48mV to 22mV. This is simply considering only one simple scenario. The situation even worsens when augmented with other effects. For the open circuit scenario, it results in zero output voltage. Similarly, for the short circuit case, the output result shows 1.8nV which is very small and it can be considered as zero output voltage.

For capacitive effects, the output becomes very small (140 $\mu$ V), unstable and oscillating. For the combined resistive and capacitive effects, the output is nearest to zero (65  $\mu$ V) and oscillating.

It can be concluded that the output of the circuits is affected as the manufacturing processes become inaccurate. It results in signal loss, poor performance and malfunctioning of circuits.

## REFERENCES

- [1] Marina Y. Koledintseva, Praveen K. R. Anmula, James L. Drewniak "Effect of Conductor Surface Roughness upon Measured Loss and Extracted Values of PCB Laminate Material Dissipation Factor" EMC Laboratory, Missouri University of Science & Technology Rolla, MO 65401, 2011
- [2] Marina Y. Koledintseva, James L. Drewniak, AmendraKoul, Fan Zhou "Thermal Effects on PCB Laminate Material Dielectric Constant and Dissipation Factor" EMC Laboratory, Missouri University of Science & Technology Rolla, MO 65401, 2011
- [3] G.A. Schuerinka, M. Slompa, Wessel W. Witsa, R. Legtenberg, E.A. Kappelb "Modeling printed circuit board curvature in relation to manufacturing process steps" 2nd CIRP Global Web Conference, London, UK, 2012
- [4] Andy Haas, TaranjitKukul "Ensuring Reliable and Optimal Analog PCB Designs with Allegro AMS Simulator" Cadence Design Systems, Silicon Valley 2007
- [5] Toshiyuki Matsuki and Yoneta Tanaka "High Overlay Accuracy Using Scaling Method in PWB Photolithography" Ushio Inc, Aoba-Ku, Yokohama, Japan, 2013
- [6] Ajay Pal Singh Chauhan, Sharat Chandra Bhardwaj, 'Detection of Bare PCB Defects by Image Subtraction Method using Machine Vision' Proceedings of the World Congress on Engineering 2011 Vol II WCE 2011, London, U.K, July 6 - 8, 2011
- [7] Barry Olney "Introduction to Board Level Simulation and the PCB Design Process" In circuit design PTY LTD, Australia, March 2012
- [8] Alexandru Topo, "Optical Correlation Techniques for Alignment in Future Pattern Generator" Master's Thesis at the Department of Production Engineering School of Industrial Engineering and Management, KTH, June 2013
- [9] Peter W. Lehmann "PCB manufacturing process improvement: drilling Machine Optimization", University of Wisconsin-stout, December 2005
- [10] Cheryl Tulkoff, Greg Caswell, Dr. Craig Hillman "Best Practices for Improving the PCB Supply Chain: Performing the Process Audit", DfR Solutions Beltsville, MD, USA, 2011
- [11]

- [12] L. J. Zheng, X.Zhang, C. Y. Wang, L. F. Wang<sup>1</sup>, S. Li<sup>1</sup>, Y. X. Song, L. Q. Zhang<sup>2</sup>, “*Experimental Study of Micro-holes Position Accuracy on Drilling Flexible Printed Circuit Board*”, 11<sup>th</sup> Global Conference on Sustainable Manufacturing, Berlin, Germany, September 23-25, 2013
- [13] Abdelghani Renbi, ArashRisseh, RikardQvarnstrom and Jerker Delsing “*Impact of etch factor on characteristic impedance, crosstalk and board density*” IMAPS, San Diego, California, USA, 45th International Symposium on Microelectronics, 2012
- [14] N.D. Misal “*Optimization of process parameters in etching during photo chemical machining process*” “Department of Mechanical Engineering, SVERI’s College of Engineering (Poly), Pandharpur, 2013
- [15] Christopher F. Wise “*Fabrication of Printed Circuit Boards Using a Table Top CNC Mill*” Departmental Engineer, New Mexico State University, Department of Engineering Technology and Surveying Engineering P.O.Box 30001, MSC 3566, Las Cruces, NM 88003-8001, [chwise@nmsu.edu](mailto:chwise@nmsu.edu), 2010
- [16] Kraig Mitzner” *Complete PCB Design Using OrCad Capture and Layout*” Elsevier, 2007



# PERFORMANCE COPARISION OF INVERTED L AND F-SHAPE DUAL BAND MICROSTRIP ANTENNA

Solomon Muluneh<sup>1</sup>, and Fikreselam Gared<sup>2\*</sup>

<sup>1</sup>Bahir Dar Institute of Technology, Bahir Dar University  
([solomonmuluneh2006@gmail.com](mailto:solomonmuluneh2006@gmail.com))

<sup>2\*</sup>Bahir Dar Institute of Technology, Bahir Dar University  
([fikreseafomi@gmail.com](mailto:fikreseafomi@gmail.com))

## ABSTRACT

*Wireless Local Area Network (WLAN) application nowadays has become more popular, since it allows users to access network services without being tethered to a wired infrastructure. In high performance point to point and point to multipoint application where size, weight, cost, performance, ease of installation are constraints, low profile antenna is very much required. To meet these requirements, microstrip antenna is preferred. In this work two dual bands inverted L and F-shape geometry microstrip antennas using probe feeding operating at 2.45GHz and 5.8 GHz for WLAN application was designed and simulated. The simulation process has been done through EMPIRE software. The properties of antenna such as bandwidth, S parameter, VSWR were investigated. The simulation results show the bandwidth is maximum for dual band F-shape antenna at 5.8 GHz frequency that is 244. The return losses are better for inverted L-shape antenna at 2.45 GHz that is -25.62dB.*

**Keywords-** Dual band, Microstrip Antenna, Probe Feeding, WLAN

## INTRODUCTION

Communications has become the key to momentous changes as it conveys information between the source and destination. Information is indeed the lifeblood of modern economies and antennas provide mother earth a solution to a wireless communication system (Abu *et al.*, 2009).

Antennas are the most important components required to create a communication link and be defined as the structure associated with the region of transition between a guided wave and a free space wave, (Constantine A. Balanis., 1997). The demand for antennas, capable to be embedded in portable devices which serve a wireless land mobile or terrestrial network. With time and requirements, these devices become smaller in size and hence the antennas required for transmit and receive signals have also to be smaller and light weight.

The current trend in commercial and government communication systems has been to develop low cost, minimal weight, low profile antennas that are capable of maintaining high performance over a large spectrum of frequencies. This technology has focused much effort into the design of micro strip (patch) antennas. Micro strip antennas appeared as a by-product of micro strip circuits, which by then had become a mature technology. Their design and realization took advantage of the techniques developed for micro strip circuits and used micro strip circuit substrates with a simple geometry, this antenna offer many advantages not commonly exhibited in other antenna configurations (Ramesh *et al.*, 2001). In principle, dual-band antennas should operate with similar features, both in terms of radiation and impedance matching, at two or more separate frequencies. It is known that a simple rectangular micro strip patch can be regarded as a cavity with magnetic walls on the radiating edges.

The first three modes with the same polarization can be indicated by  $TM_{10}$ ,  $TM_{20}$  and  $TM_{30}$ .  $TM_{10}$  is the mode typically used in practical applications whereas  $TM_{20}$  and  $TM_{30}$  are associated with a frequency approximately twice and triple of that of the mode.

This provides the possibility to operate at multiple frequencies. The simplest way to operate at dual frequencies is to use the first resonance of the two orthogonal dimensions of the rectangular patch, i.e.,  $TM_{10}$ , and  $TM_{01}$ , modes. In this case, the frequency ratio is approximately equal to the ratio between the two orthogonal sides of the patch. The obvious limitation of this approach is that the two different frequencies excite two orthogonal polarizations.

The most popular technique for obtaining a dual-frequency behavior is to introduce a reactive loading to a single patch, including stubs (Richards *et al.*, 1985), notches (Rod and Waterhouse, 1999), pins (Hammerstad, 1975), (S. Zhong *et al.*, 1983), capacitors and slots (Ramesh *et al.*, 2001). By reactive-loading approaches, one can modify the resonant mode of the patch, so that the radiation pattern of the higher order mode could be similar to that of the fundamental mode. This indicates that the use of a single feed for both frequencies on a single radiating element can be realized.

In rectangular patch with two narrow slots etched close to and parallel to the radiating edge was used to obtain the dual-frequency operation proposed by (Maci *et al.*, 1993). In this dual-frequency design, the two operating frequencies are associated with the  $TM_{01}$ , and  $TM_{30}$ , modes of the un-slotted rectangular patch. In addition, this two operating frequencies have the same polarization planes and broadside radiation patterns, with a frequency ratio within the range of 1.6-2.0 for the inset feed case.

The above approach characterizes dual-frequency patch antennas, which will be identified as orthogonal mode dual-

frequency patch antenna (Ramesh *et al.*, 2001). This can be extended to any kind of patch shape that offers two cross-polarized resonant modes.

Misran *et al.*, (2008) present a coaxially-fed single-layer compact micro strip patch antenna for achieving dual-polarized radiation suitable for applications in the IEEE Radar band C and X. Simultaneous use of both frequencies should dramatically improve data collection and knowledge of the targets in an airborne synthetic aperture radar system.

The designed antenna consists of three rectangular patches that are overlapped along their diagonals. The design and simulation of the antenna were performed using 3D full wave electromagnetic simulator IE3D. The measured results show that the designed antenna achieves VSWR less than 2 and a bandwidth of 154 MHz.

Abu *et al.*, (2009) have also proposed a slotted e-shape rectangular patch antenna with dual-frequency operation. The patch dimension of 34×23 mm, FR4 substrate material having thickness of 1.6 mm and permittivity of 4.8 were used. The measured results show that the designed antenna achieves a VSWR less than 2 with bandwidth of 3.02% (2.45-2.525 GHz) at lower frequency and 1.65% (6.125 - 6.025 GHz) at upper frequency and measured gain of this antenna is 3 dB for both working frequencies.

Wideband and dual-band characteristics of single and double notched rectangular patch antennas are also presented by Palit S.K. and Hamadi A., (1999). A comparative study of the experimental results employing coax, microstrip aperture-coupled and electromagnetically coupled feed techniques have been made for increased bandwidth and improved cross-polar level that is a measure of how an antenna is purely polarized. It is determined by the difference in decibels between the maximum radiation intensity of the co and cross polarizations.

The experimental radiation patterns were compared with simulated and theoretical patterns found to be in good agreement. Thus, the maximum measured impedance bandwidths of 26.6% in band 1 and 31.7% in band 2 have been achieved for coax-fed single-notched patches. A double-layered double-notched aperture coupled (composite) patch antenna was also designed, and further improvement in impedance bandwidth of 39% was achieved without significant degradation in radiation characteristics.

Tlili, (2010) a double C-slot microstrip antenna is designed and simulated for the WiMAX frequency range of 2.5-2.69 GHz. This antenna presents an extension to the single C slot antenna. The proposed antenna has a gain of 6.46 dBi and a size reduction of 37% when compared to a conventional square microstrip patch antenna.

Gupta, (2012) proposed design and fabrication of dual and triple band microstrip patch antennas using proximity feeding for wireless applications. The geometry shape used was an inverted T shaped slot that resonates at 2.45 and 5.8 GHz frequencies. In this design stacking and Defected Ground Structure (DGS) are used where, the size of stacked substrate is different from the main substrates. The design of the antenna has patch width and length of 29.036mm and 25.054mm respectively. The substrates used were same material having dielectric constant of 4.4 and the height of the substrate was 1.57mm. The simulation results of the designed antenna indicated that return loss and bandwidth of -16dB and 88MHz at 2.4GHz and -17.5dB and 67MHz at 5.8GHz respectively. Similarly, VSWR is 1.4 and 1.3 at frequencies of 2.4 GHz and 5.8GHz respectively.

Thus, from the reviewed literatures different types of Microstrip antenna were designed for different application and their performances are described. The design of

an efficient dual frequency small size patch antenna for recent wireless applications is a major challenge so that in this work significant size reduction, enhancement of antenna bandwidth and design of dual band frequencies with geometry of Inverted L-shape and F-Shape antennas for wireless application is proposed.

## **MATERIALS AND METHODS**

In this thesis work dual bands inverted L and F-shape geometry microstrip antennas have been designed and simulated. Probe feeding technique was used for excitation of the designed dual band microstrip antennas. Probe feed was used to couple microwave energy to the antenna and feed point can be located on anywhere within the patch but, the feed location inside the patch was properly selected to obtain good impedance match at both resonances since the antenna resonates at two frequencies one corresponding to the width and the other corresponding to the length. The center of the patch was taken as the origin and the feed point location was given by the coordinates  $(X_f, Y_f)$  from the origin. The feed point must be located on the patch at a point where the input impedance is 50 ohms for the resonant frequency. For different locations of the feed point, the return loss was compared and that feed point was selected where the return loss is most negative.

### **Design of Dual Band Proposed Micro strip Antennas**

Significant reduction of antenna size was realized by using inverted L-shaped patch geometry instead of the conventional rectangular micro strip patch antenna. The inverted-L shape antenna shown in Figure 1 consists of patch of width and lengths etched on a Rogers RT/Droid 5870 substrate of thickness  $h = 1.160\text{mm}$  and dielectric constant  $\epsilon_r = 2.330$ . The different parameters of the patch were varied and the

optimum results and their effects in the radiation characteristics were studied.



Figure 1: Inverted L shape antenna geometry at 2.45 and 5.8 GHz

As shown in Table 1 the dimensions of Inverted L-shape microstrip patch antenna at operating frequency 2.45GHz and 5.8 GHz are listed. The slot length  $L_s$  and slot width  $W_s$  are selected in such a way that it helps to get the optimized performance of the antenna. The Second antenna geometry developed for attaining dual frequency operation was having the shape of F- shape geometry, Which was consisted of patch of width and length etched on a Rogers RT/Droid 5870 substrate of thickness  $h = 1.160\text{mm}$  and dielectric constant  $\epsilon_r = 2.330$ .

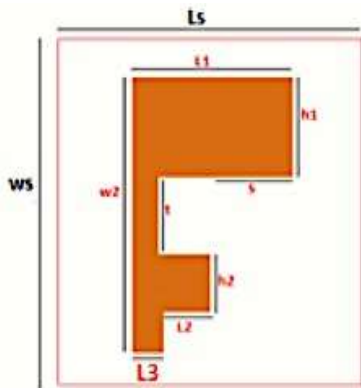


Figure 2: F-antenna geometry at 2.45 and 5.8 GHz.

**RESULTS AND DISCUSSION**

In this section the simulation results was demonstrated to show the performance of our proposed micro strip antenna shapes.

Results for return loss, bandwidth, radiation pattern, and far field radiation for both inverted L and F shape dual band antennas was discussed.

**Inverted L-Shape Antenna**

The probe feed is used to excite the designed dual inverted L-shaped antenna and the center frequency is selected at which the return loss is minimum. The designed antenna resonates at 2.45 GHz and 5.8 GHz frequencies. The return loss for 2.45 GHz and 5.8 GHz are -25.62 dB -23.29 dB respectively that satisfies the minimum required value of return loss of -10 dB and these values are shown in Figure 3 that presents the  $S_{11}$  parameters (return loss in dB) frequency.

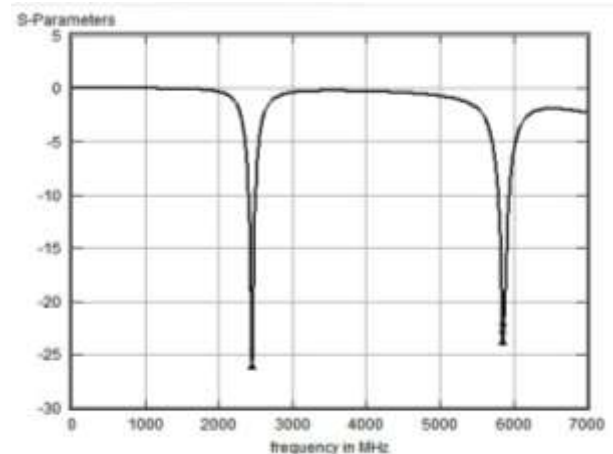


Figure 3: S-Parameter versus frequency for dual band inverted L micro strip antenna.

The bandwidth of inverted L- shape antenna can be calculated from return loss versus frequency plot. Based on this, the -10 dB and 3 dB bandwidth of the designed inverted L shape antenna are 144 MHz and 63 MHz for 2.45 GHz frequency, 190 MHz and 90 MHz for 5.8 GHz frequency respectively. -10 dB and 3dB bandwidth for 2.45 GHz and 5.8 GHz frequency has been shown in Figure 4 and 5 respectively.

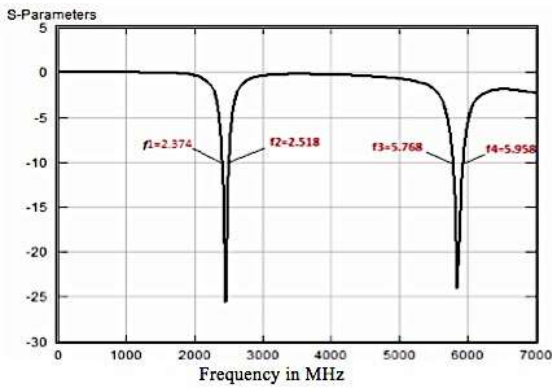


Figure 4: -10dB bandwidth of dual band inverted L antenna at 2.45 and 5.8 GHz.

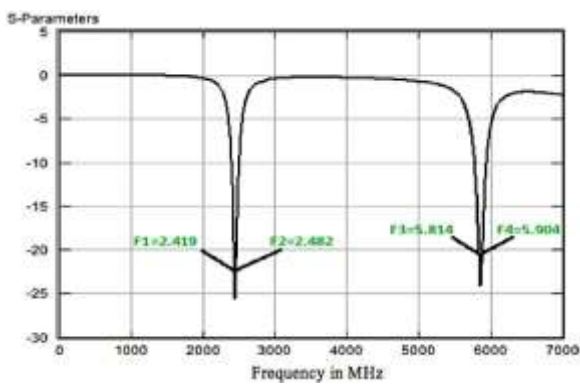


Figure 5: 3dB bandwidth of dual band inverted L antenna at 2.45 and 5.8 GHz.

Figure 5 shows the 3dB Bw, which describes the point where the power output is half than the input power. It is conventions that the power at output drops to half, performance could be tolerated. As shown in Figure 4 and 5, the -10 dB and 3 dB bandwidth of the designed inverted L shape antenna are 144 MHz and 63 MHz for 2.45 GHz frequency, 190 MHz and 90 MHz for 5.8 GHz respectively.

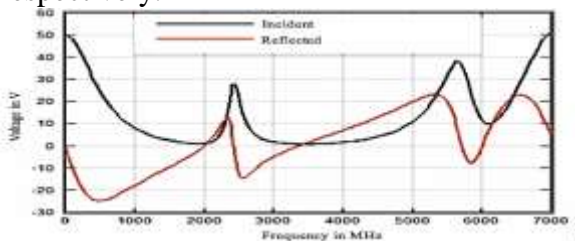


Figure 6: Frequency domain voltage radiation Pattern

can be seen from the Figure 6, the reflected voltage amplitude was smaller than the incident voltage amplitude, giving a larger return loss. From the frequency domain voltage, one can also observe that the incident voltage was stronger than the reflected voltage that gives larger return loss at the expected operating frequencies of the antenna.

The Far field radiation pattern of inverted L-shape microstrip antenna shown in Figure 7 indicates the E and H-plane pattern at 2.45GHz and 5.8GHz center frequency and it can be observed that the designed antenna has stable radiation pattern throughout the whole operating frequency band.

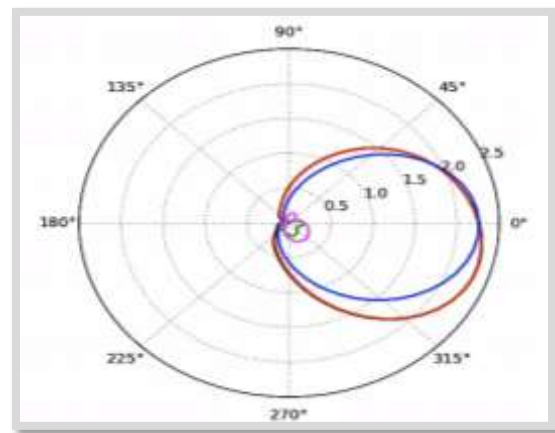


Figure 7: Far field radiation pattern polar plot (Linear).

Efficiency is defined as the ratio of the radiated power ( $P_{rad}$ ) to the input power ( $P_i$ ). The input power is transformed into radiated power and surface wave power while a small portion is dissipated due to conductor and dielectric losses of the materials used. From this the radiation efficiency and the gain of the proposed L-shape geometry are 72.22% and 2.25dBi respectively. Where power into Excitation port ( $P_i$ ) = 1.829W, incident power into excitation port ( $p_{inc}$ ) = 2.356W, and radiated power = 1.321W.

**F-Shape Antenna**

Similarly the simulation result for F-geometry of dual band microstrip antenna that resonates at 2.45 GHz and 5.8 GHz frequencies are presented and discussed in detail. As shown in Figure 8 the return loss for 2.45 GHz and 5.8GHz are -23.51 dB and -25.05dB respectively in which the minimum required return loss value, -10 dB, is satisfied.

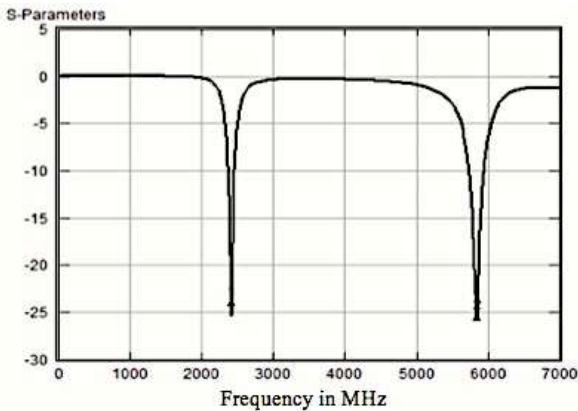


Figure 8: S-parameter versus frequency for dual band F shape microstrip antenna

Since the bandwidth of antenna can be calculated from return loss, the obtained values are shown in Figure 9 and 10. The -10dB and 3dB bandwidth of the designed F-shape antenna are 136 MHz and 72 MHz for 2.45 GHz frequency and 244 MHz and 81MHz for 5.8 GHz frequencies respectively.

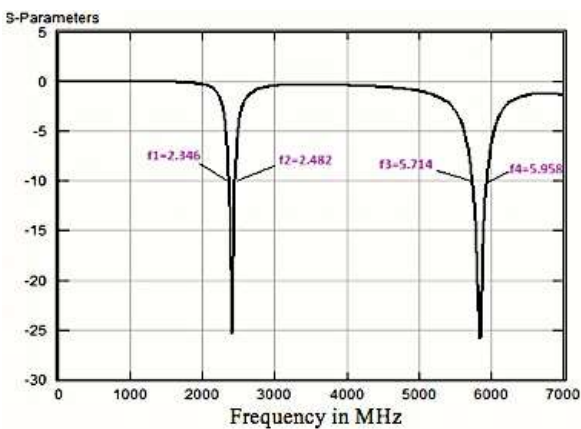


Figure 9: -10 dB band width of dual band F shape antenna at 2.45 and 5.8 GHz

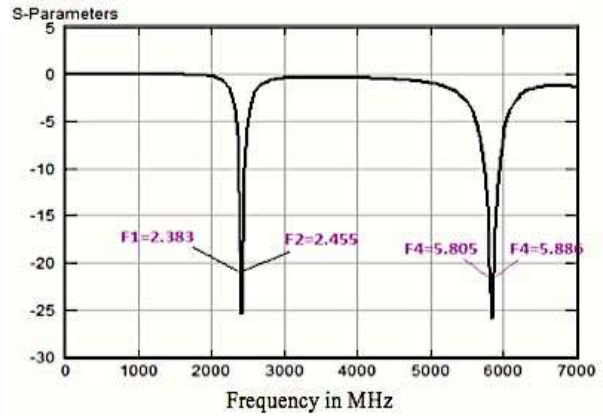


Figure 10: 3dB band width of dual band F shape antenna at 2.45 and 5.8 GHz

As can be seen from the Figure 11, the reflected voltage amplitude is smaller than that of the incident voltage amplitude, giving a larger return loss. From the frequency domain voltage cure, one can identify that the incident voltage is stronger than the reflected voltage and this assures that the return loss at the expected operating frequencies of the antenna is large.

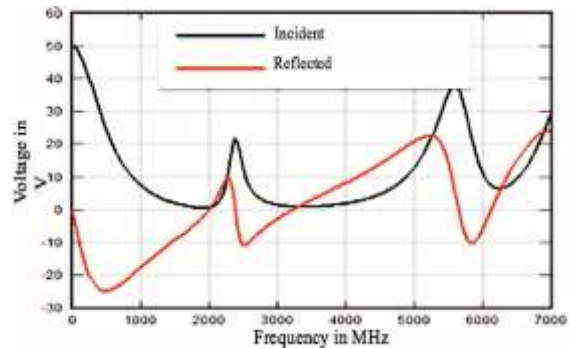


Figure 11: Frequency domain voltage radiation Pattern

Figure 12 presents the E and H- plane pattern of F-shape microstrip antenna at 2.45GHz and 5.8GHz center frequencies and this indicates that the antenna radiates power in all directions for the entire operating band.

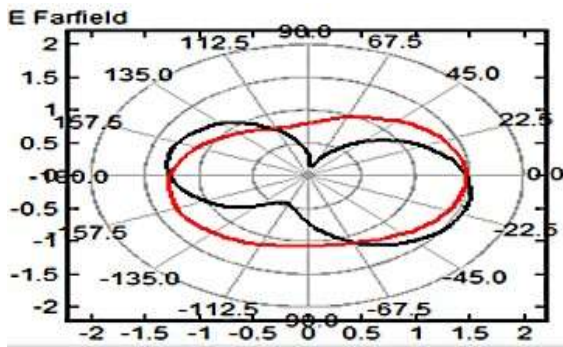


Figure 12: Far field radiation pattern (linear).

Finally, the comparison table based on different parameters that have been mention above for the two proposed geometries of microstrip antenna is shown in Table 3. Finally, the comparison table based on different parameters that have been mention above for the two proposed geometries of microstrip antenna is shown in Table 3.

Table 4 shows surface area for both proposed geometry. From the table we observe that the surface area of the radiating patch obtained for each type of antennas are  $176\text{mm}^2$  and  $129\text{mm}^2$  respectively with respect to the operating frequency of the antennas.

The result shows that the F-shaped antenna has small surface area which achieved a size reduction of 0.47% when compared with that of an inverted L-shaped antenna, Generally the performance parameters like bandwidth, return loss, and gain of the designed antenna in this work are better and there was a significant surface area reduction, so that the cost for fabricating for F-shape antenna is more cheaper than inverted L-shape antenna.

### CONCLUSIONS

This work presents design and simulation of different shapes of microstrip antenna intended to be used for WLAN application at 2.45GHz and 5.8 GHz operating frequencies. The results report dual band

inverted L-shape and F-shape microstrip antenna using probe feeding technique and comparison made with antenna parameters like: return loss, bandwidth, and Gain. As stated in results section physical parameters affects the results and performances of the antennas and it can be observed that varying these parameters in the right manner gives optimized results for a desired resonant frequency operation of Microstrip Antenna. Thus, the designed antennas give efficient results resonating at 2.45 GHz and 5.8 GHz that could be applicable for WLAN. Based on the parameters, the bandwidth is maximum for F-shape antenna at 5.8 GHz frequency that is 244 MHz for which 100 MHz is acceptable whereas the return losses are better for inverted L-shape antenna at 2.45 GHz that is -25.62dB. The VSWR of both antennas lie between 1 and 2 so that all the designs are acceptable. In General, the obtained performance values achieved the need of microstrip patch antenna.

### REFERENCES

- [1] Abu et al., (2009), "Slotted e-shape antenna design for dual frequency operation", *IEEE 3rd European Conference on Antennas and Propagation: 2416 – 2419*.
- [2] Constantin A. Balanis. (1997), "Antenna theory analysis and design". *John Wiley & sons, Inc, Hoboken, New Jersey*.
- [3] Ramesh et al (2001), "Microstrip Antenna Design Handbook", Artech House publishers, London.
- [4] Richards et al., (1985), "Dual-Band Reactively Loaded Microstrip Antenna", *IEEE Transactions on Antennas and Propagation*, 33 (5): 556-560.
- [5] Rod and Waterhouse (1999). "Microstrip patch antennas A

- designer's guide", Springer Science and Business Media.
- [6] Hammerstad (1975), "Equations for microstrip Circuit Design", Proc. Fifth European Microwave Conference, page 268-272.
- [7] Zhong S. et al., (1983), "Single Element Rectangular Microstrip Antenna for Dual-Frequency Operation" Electronics Letters, pp. 298-300, Illinois University, Urbana.
- [8] Maci et al (1993), "Single-Layer Dual-Frequency Patch Antenna", *Electronics Letters journal*, 29(16): 1441-1443.
- [9] Misran et al (2008) "Design, simulation and fabrication of a microstrip patch antenna for dual band application", *IEEE International Conference on Electrical and Computer Engineering*: 799 – 802.
- [10] Palit, S.K. Hamadi A. (1999), "Design and development of wideband and dual-band microstrip Antennas" *Microwaves, Antennas and Propagation*, IEEE Proceedings, vol. 146, no. 1, pp 35-39.
- [11] Tlili (2010), "Design of double C-slot microstrip patch antenna for WiMax application", *IEEE Antennas and Propagation Society International Symposium*: 1 – 4.
- [12] Gupta (2012), "Design and Fabrication of Dual and Triple Band Microstrip Patch Antennas Using Proximity Coupling for Wireless Applications" (PhD), Thapar Institute of Engineering and Technology, India

Table 1. Dimensions of designed inverted L- antenna geometry

Antenna Geometry	Antenna Parameter	Value (mm)	Dimensions (mm <sup>2</sup> )
	L <sub>1</sub>	16.25	21.93*22.00
	L <sub>2</sub>	6.00	
	L <sub>3</sub>	10.50	
	L <sub>4</sub>	2.25	
	w <sub>1</sub>	10.00	
	w <sub>2</sub>	16.54	
	h <sub>1</sub>	5.00	
	h <sub>2</sub>	10.00	
	L <sub>s</sub>	21.93	
	W <sub>s</sub>	22.00	

Table 2: Dimension of designed F –antenna Geometry

Antenna Geometry	Antenna Parameter	Value(mm)	Dimensions (mm <sup>2</sup> )
<p style="text-align: center;">F- Antenna</p>	L1	10.50	16*24.50
	t	6.68	
	h <sub>1</sub>	8.50	
	h <sub>2</sub>	4.81	
	L <sub>3</sub>	2.60	
	s	7.0	
	L <sub>s</sub>	16	
	W <sub>s</sub>	24.50	
	W2	22.50	

Table 3. Comparison of simulated Antenna

Antenna Configuration	Resonating Frequency	Return Loss	Bandwidth	VSWR	Gain
Dual Band Inverted L-shape Antenna	2.45 GHz	-25.62dB	144MHz	1.004	2.25dBi
	5.8 GHz	-23.29dB	190MHz	1.083	
Dual Band F-shape Antenna	2.45 GHz	-23.51dB	136MHz	1.009	1.4dBi
	5.8 GHz	-25.05dB	244MHz	1.007	

Table 4. Surface area comparisons of the proposed geometries

Antenna Configuration	Resonating Frequency	Patch Area (mm <sup>2</sup> )
Dual Band Inverted L-shape Antenna	2.45 GHz & 5.8 GHz	176mm <sup>2</sup>
Dual Band F-shape Antenna	2.45 GHz & 5.8 GHz	129mm <sup>2</sup>

# APPLICATION LAYER DDoS ATTACK DETECTION IN THE PRESENCE OF FLASH CROWD

Biruk Asmare Muse, Surafel Lemma Abebe  
Addis Ababa Institute of Technology, Addis Ababa University  
{biruk.asmare, surafel.lemma}@aait.edu.et

## ABSTRACT

*Application layer DDoS attacks are growing at an alarming rate in terms of attack intensity and number of attacks. Attackers target websites of government agencies as well as private business for different motives. In some situations, application layer DDoS attacks occur together with characteristically analogous flash crowds. This paper focuses on distinguishing application layer DDoS attacks from flash crowds. Both flash crowd and application layer DDoS attack cause denial of service. Flash crowds come from sudden surge in traffic of legitimate requests. Whereas, application layer DDoS attacks are intentionally generated by attackers to cause denial of service. Distinguishing between application layer DDoS attack and flash crowd is important because the response taken for the case of flash crowd is different from response taken for application layer DDoS attack. Flash crowds are legitimate requests which should be serviced. Application layer DDoS attacks, on the other hand, are malicious requests that should not be serviced. In this research, supervised machine learning based application layer DDoS detection approach is proposed to distinguish between application layer DDoS attack and flash crowd. Features that help distinguish application layer DDoS attacks from legitimate flash crowds were identified. Six supervised classifiers were evaluated using World Cup 98 flash crowd dataset and experimentally generated application layer DDoS attack dataset. The results show that decision tree outperformed other classifiers considering combination of classification time, F1-score and FPR. Decision tree has F1-score of 99.45% and false positive rate of 0.47%.*

**Keywords:** DDoS attack, flash crowd, application layer

## INTRODUCTION

Distributed Denial of Service (DDoS) attacks are attacks against availability of Internet services. DDoS attacks are divided into application layer and network layer attacks. Network layer attacks exploit flaws of network and transport layer protocols while application layer DDoS (APP-DDoS) attacks use application layer protocols such as HTTP, FTP and SMTP [1, 2]. The attack is conducted after creating a successful TCP connection. This characteristics makes the attack resistant to most network layer detection and mitigation systems, and hence, difficult to detect [1].

As the threats of APP-DDoS attacks grow in type and complexity, a number of approaches were proposed to help distinguish between APP-DDoS attack and normal activity [1, 2, 3, 4, 5, 6].

In this research, we deal with APP-DDoS attacks that occur together with flash crowds. Flash crowd is a sudden or anticipated large surge in number of requests to a website by legitimate clients due to the addition of some news or when a new product is released [4]. Application layer DDoS attacks have similar characteristics as legitimate flash crowds. Hence, distinguishing between flash crowds and APP-DDoS attacks is a very important network security problem. Realizing the importance, several researches proposed different approaches [3, 7, 8, 9, 10].

The existing approaches that are used to distinguish APP-DDoS attacks from flash crowd have three limitations. The first limitation is that the approaches rely on one or two features for detection [8, 10]. This impacts the robustness of such

detection systems and helps attackers to easily mimic legitimate requests in their attack. The second limitation is that some approaches rely on network layer information such as IP address entropy and packet flow rate [3, 9]. However, it is not difficult to deploy proportional attack machines to that of legitimate machines in flash crowd. The third limitation is that existing information theory based approaches require accurate model of legitimate traffic as a baseline [9]. This is usually difficult to obtain considering the variable nature of internet traffic.

To address the aforementioned problem, we propose a system that distinguishes APP-DDoS attacks from legitimate flash crowds using combination of five features: *request rate*, *page popularity*, *download rate*, *request inter-arrival time* and *ratio of successful requests*. We conjecture that these features will help to distinguish DDoS attack from flash crowd. The features could easily be obtained from web server logs and computed by considering a given time interval, called session time, for each unique client. A client is a machine which is identified by an IP address and makes a request to a server. The core part of the proposed detection system is a supervised learning classifier that classifies a client to either normal client or attack client. The classifier is trained using examples of both flash crowds and APP-DDoS attack. The examples are collection of records which contain feature values.

To evaluate our proposed approach, a data set containing examples of flash crowd and APP-DDoS attack is prepared. The World Cup 98 data [1] is used to model flash crowds. World Cup 98 data is a collection of requests made to *www.france98.com* during the duration of World Cup 98 football game. World Cup 98 data set is used as flash crowd data set in related researches [3, 8, 11, 12]. We prepared application layer DDoS attack data set by performing attack on locally hosted version of the same website using BoNeSi [13] DDoS attack tool.

Using the prepared dataset, we tested our proposed approach in terms of performance of candidate classifiers for detection, effect of session time on detection performance and contribution of identified features for detection. The result shows that although AdaBoost, random forest and decision tree classifiers have very close classification performance, decision tree outperformed all other tested classifiers considering classification time. Decision tree has F1-score of 99.45% and false positive rate of 0.47%. Furthermore, variation of session time has very little impact on the performance of decision tree classifier. Among all features, download rate and request rate have highest contribution for detection.

The specific contributions of this paper are as follows:

- A supervised classifier-based detection system that distinguishes between APP-DDoS attacks and flash crowds is proposed. The proposed approach uses features directly available from server access logs that can be computed with small resources. In addition, our detection model has minimal computational and memory overhead during operation which is important requirement for real time DDoS detection and defense systems. The proposed approach does not rely on establishing accurate legitimate traffic baseline. It is adaptive to different APP-DDoS attack and flash crowd behaviors.
- The commonly used World Cup 98 flash crowd dataset is complemented by performing APP-DDoS attack on locally cloned World Cup 98 website. The combined flash crowd and APP-DDoS dataset is available on request for replication and comparison purposes.
- The detection and computation performance of the proposed approach is empirically evaluated. The contribution of each feature to

distinguish between APP-DDoS attacks and flash crowds is also discussed.

The rest of the paper is organized as follows. Section 2 describes related research work. The proposed approach is presented in Section 3. Sections 4 and 5 discuss experiments used to evaluate the proposed approach and evaluation result, respectively. In Section 5, the proposed approach is also compared with state of the art. Section 6 discusses conclusion and future work.

### Related work

Taxonomy of flash crowds and some features that help differentiate APP-DDoS attacks from flash crowds were discussed in the work of Bhandari et al. [11]. Features such as distribution of requests among source IP, geographical distribution of source IP, URL access behavior and change in rate of request were suggested to distinguish between flash crowd and APP-DDoS attack [11]. The authors used World Cup 98 dataset to model flash crowds and created APP-DDoS attack using simulation to investigate the significance of the suggested features. The result showed that URL access behavior has more contribution to distinguish APP-DDoS attacks from flash crowds. Page popularity in our work is used to capture URL access behavior. The authors recommended combination of network layer and application layer features for APP-DDoS detection from flash crowd.

Information obtained from network packets such as source address, destination address is used together with packet flow rate and time interval to distinguish APP-DDoS attacks from flash crowd [3, 7, 8, 9]. Sahoo et.al [7] exploited generalized entropy and information distance to distinguish between APP-DDoS and flash crowd in software defined networks. Behal et al. [8] proposed ISP level detection approach using the aforementioned information distance metrics. Daneshgاده et al. [3] used a combination of machine

learning based, Shannon entropy and Mahalanobis distance to distinguish between normal traffic, flash crowd and APP-DDoS attack. The authors used similar flash crowd dataset and the same APP-DDoS attack tool with our work and obtained a precision of 93% and recall of 100%. Khalf et al. [10] proposed a software agent-based model using attack intensity and IP address information to address the problem of distinguishing APP-DDoS from flash crowd attack. Although promising results are obtained in the information based metrics, All approaches rely on the assumption that APP-DDoS attackers use less number of unique IP addresses compared to legitimate users. However, considering the large number of available IOT devices that can potentially be deployed in this attack, the attackers can deploy proportional number of unique IP addresses with legitimate users. This makes the aforementioned approaches ineffective in such scenarios.

In addition to network layer features, there are some application layer features to distinguish flash crowds from APP-DDoS attacks. Yu et al. [14] suggested page popularity to identify APP-DDoS attack from flash crowd, while, Xie et al. [15] and Ye et al. [16] suggested page access transition to identify APP-DDoS attack from legitimate flash crowd. In the work of Yu et al. [14], page access entropy was suggested by assuming that the entropy of flash crowd page access is different from APP-DDoS attack. This approach may not work when the attacker requests popular pages by studying the website. Ye et al. proposed the transition behavior between web pages for detection of APP-DDoS attack [16]. Xie et al. modeled spatial and temporal user access patterns of flash crowds using hidden Semi-Markov model to achieve the same goal [15]. Another approach that uses a combination of network layer and application layer features was suggested by Ramamoorthi et al. [17]. It uses features such as HTTP

request rate and page viewing time from application layer and session rate, number of TCP, UDP and ICMP packets from network layer. Enhanced support vector machine with string kernel was used to model legitimate flash crowd. They obtained a classification accuracy of 99.32%. Request rate, page popularity and page access pattern were commonly used features for detection of APP-DDoS attacks against normal or flash crowd [11, 14, 17].

Existing approaches that are used to distinguish APP-DDoS attacks from flash crowd have three limitations. The first limitation is that the approaches rely on one or two features for detection which impacts the robustness of such detection systems. This in turn helps attackers to easily mimic legitimate requests in their attack. For example, detection systems that rely on page popularity may fail when the attacker studies the website to identify most popular pages and then programs its zombies to request most popular pages. Again, if the detection system considers page access transition for detection, the attacker may easily program its zombies to follow a similar access pattern to that of legitimate users. This shows that using a combination of the above features will make the detection system more robust. The second limitation is that some approaches rely on network layer information such as IP address entropy and packet flow rate. However, it is not difficult to deploy proportional attack machines to that of legitimate machines in flash crowd. The third limitation is that, most existing approaches require accurate model of legitimate traffic as a baseline which is difficult to obtain considering the variable nature of internet traffic.

To address this gap in state of the art, we propose a supervised machine learning based APP-DDoS detection approach that distinguishes APP-DDoS attacks from flash crowd using a combination of features. The features used for the detection can be obtained from web server

access logs. Hence, minimal extra effort is required to collect the features. The proposed detection approach is simple and computationally efficient enough to be deployed in real systems. We evaluate our proposed detection system using World Cup 98 dataset and simulated APP-DDoS attack dataset. Similar flash crowd and APP-DDoS attack dataset is used in recent researches [5]. We further investigate the relevance of the features for the detection of APP-DDoS attack against legitimate flash crowds.

### APP-DDoS DETECTION

The proposed APP-DDoS attack detection system has two stages. The stages are *feature computation from server access log and detection stage based on the computed features*. The input for feature computation stage is web server log data. Web server logs contain information about the requests made by clients. Server log information includes the client address, time stamp, URL of the requested object, reply size and client browser information. It is difficult to have accurate attack detection by considering only the information available on server logs. Some literatures suggested additional features that are derived from basic server log information [1, 2, 4, 5, 6, 18]. We have selected *Request rate (RR)*, *page popularity (PP)*, *request inter-arrival time (RIA)*, *download rate (DR)*, and *ratio of successful requests (RSR)*. The selection was done by looking into potential contribution of the feature for detecting DDoS attack and the computational requirement of the feature in terms of memory and processing time. The justifications for selecting the features are presented in Table 1.

All features are computed for each unique client by considering a predefined time interval called session time. Client is defined as the source of the request identified by IP address. Each client has its own unique IP address. The details of these features are discussed in Sub-section 3.1.

Table 1: Feature selection reason

Feature	Justification of choice
RR	Request flooding APP-DDoS attack is characterized by high number of requests per client whereas the number of requests per client is small for flash crowd. RR is selected to help detect Request flooding attacks from flash crowds.
PP	Legitimate users in a flash crowd tend to access popular pages more frequently because they look for similar news. However, APP-DDoS attacks request different pages randomly because if they choose few popular pages, they are forced to make many requests per page compared to normal users. This will make them easy target for request rate-based filters. The PP value of APP-DDoS attack is lower than PP value of flash crowd.
RIA	Normal users take some time to view a requested page before requesting the next object. APP-DDoS attack is generated by machines that do not need viewing time. So the request inter-arrival time is smaller for APP-DDoS attacks as compared to with legitimate users in a flash crowd.
DR	When a page is requested to the server, a disk access operation is performed. The disc access time depends on the size of the requested object. Large size web objects require higher disk access time. Large size web objects can be selected to conduct asymmetric APP-DDoS attacks [1]. But normal users do not intentionally request only large size web objects. This creates a difference in download rate between APP-DDoS and flash crowd.
RSR	APP-DDoS attackers may request web objects that do not exist in the server. This makes the sever to reply with 404 error message. Legitimate users in flash crowd, however, have very low probability of requesting an object that does not exist in the website. This creates a difference in RSR between flash crowds and APP-DDoS attack.

The input of the detection stage is the value of features computed in the feature computation stage. The expected output of the detection stage is either the client is legitimate or attack. In the detection stage, we put a supervised learning classifier to make a decision.

The mitigation stage could use information obtained from the detection stage to block any pending current and future APP-DDoS requests. The IP address of the attack client could also be added to a blacklist. Mitigation stage is not the focus of this research. Figure 1 shows the stages of the proposed approach.

## Features

### Server access log

Web servers register basic information about each request such as request address, time stamp, URL, request type, response code, replay size and user agent information. Each entry in a web access log represents one request. One example entry of apache web server access log is

shown in Figure 2. The URL is relative to the web server's home directory. The time stamp has one second precision.

### Feature computation

The features used in the detection of APP-DDoS attack from flash crowds are *Request rate (RR)*, *page popularity (PP)*, *download rate (DR)*, *request inter-arrival time (RIA)* and *ratio of successful requests to total requests (RSR)*. The description and computation of the features are provided in the paragraphs below. All features are computed using a predefined session time ( $T$ ).

**Session time ( $T$ )** is a time interval in which all requests that arrive in that interval are considered together when computing features.

**Request rate (RR)** is defined as the number of requests that arrive in a session time divided by session time. RR is computed for each unique client identified by its IP address. RR can be derived from server logs by counting the number of

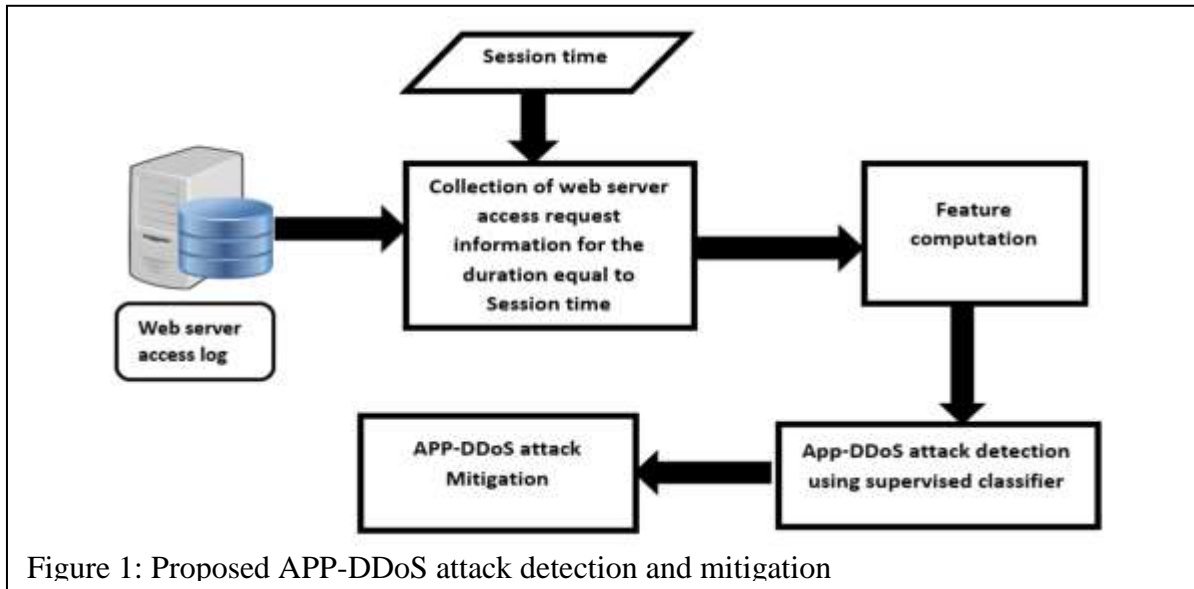


Figure 1: Proposed APP-DDoS attack detection and mitigation

requests served in  $T$  for each unique client. Equation 1 is used to compute request rate.

$$RR = \frac{N_r}{T} \quad (1)$$

where  $N_r$  is number of requests and  $T$  is the session time.

**Page popularity (PP)** is defined as the number of requests of a page or web object divided by total number of requests of all pages or web objects in the same website. A page or web object is any file that is identified by URL such as web page, image, audio, video, script, style sheet file and any other components of a website.

Before using page popularity for detection, we need to compute average popularity value of all web objects in a website. To compute average popularity, we will consider server log collected during normal operation of the website. From the collected server log, the page popularity value of each web object is computed using Equation 2.

```

::1 - - [17/Nov/2016:21:02:52 +0600]
"GET /PhpProject1/index.php HTTP/1.1"
200 2109 "-" "Mozilla/5.0 (Windows NT
10.0; WOW64; rv:39.0) Gecko/20100101
Firefox/39.0"
    
```

Figure 2: Example web server log entry

$$PP_j = \frac{NR_j}{NR_t} \quad (2)$$

where  $PP_j$  is page popularity of object  $j$ ,  $NR_j$  the number of requests of object  $j$  and  $NR_t$  total number of requests of all objects in the considered period during normal operation.

In the detection stage, we will take the average page popularity value of each web object requested by the client in a session time. The average popularity value of each requested object in the session time ( $T$ ) is summed up using Equation 3

$$PP = \sum_j NR_j * PP_j \quad (3)$$

where  $NR_j$  the number of requests of object  $j$  and  $PP_j$  page popularity of object  $j$ . All requested pages in the window time are considered in the summation.  $PP$  is computed for each client.

**Download rate (DR)** is defined as total number of bytes of reply of all requested objects in a session time divided by session time ( $T$ ). When the requested object is not found on the server, the reply size is taken as zero. Equation 4 is used to compute download rate of each client.

$$DR = \frac{\sum_i Reply_i}{T} \quad (4)$$

Where  $Reply_i$  the replay size in bytes for request  $i$  and  $T$  is session time.

**Request inter-arrival time (RIA)** is defined as the time duration between current request and previous request. The inter-arrival time between all requests in a session time are summed up. Equation 5 is used to compute request inter-arrival time of each client in a session time ( $T$ ).

$$RIA = \sum_k (t_k - t_{k-1}) \quad (5)$$

Where  $t_k$  is time stamp of request  $k$  and  $t_{k-1}$  time stamp of the immediate predecessor request  $k - 1$ .

**Ratio of successful request to total requests (RSR)** is defined as the ratio of requests with a reply code of 200 divided by total number of requests in session time. Requests with a reply code of 200 are considered as successful requests.  $RSR$  is computed for each unique client. Equation 6 is used to compute  $RSR$ . The value of  $RSR$  is between 0 and 1. A value of 0 means there is no successful request while a value of 1 means all requests are successful.

$$RSR = \frac{NRP}{NRT} \quad (6)$$

Where  $NRP$  is the total number of requests with 200 reply code that occur in session time ( $T$ ) and  $NRT$  total number of requests in the session time ( $T$ ).

### Feature scaling

The values of each feature used in the detection system have different range. For example, the download rate is usually in the range of thousands while others are in the range of decimal fractions. Some classifiers such as decision tree and Adaboost does not require all the features to be in similar scale while Support Vector Machine requires all inputs to be on the same range [19].

We applied feature scaling in order to make the values of all features in a similar range by transforming feature distribution to a normal distribution with a mean of zero and unit standard deviation, we used Equation 7.

$$x_n = \frac{x - \underline{x}}{\sigma} \quad (7)$$

Where  $x_n$  is the transformed feature value,  $x$  is original feature value,  $\underline{x}$  is the mean of all feature values and  $\sigma$  is the standard deviation of all feature values.

### Detection

The detection system distinguishes APP-DDoS from flash crowd using a supervised learning classifier. The input to the classifier is an array of five feature values corresponding to RR, PP, DR, RIA and RSR respectively. The output of the classifier is either one or zero. One means the input feature vector corresponds to APP-DDoS while zero means the input feature vector corresponds to flash crowd.

The supervised classifier used for detection is trained off-line using examples of both flash crowd and APP-DDoS attack. The training data is composed of input features  $X_i$  and corresponding label  $Y_i$ . The input feature  $X_i$  is a vector of dimension five with components RR, PP, DR, RIA and RSR respectively. The output  $Y_i$  is a binary value that indicates weather the example represents DDoS attack or normal. Attack sessions will have a value of 1 while normal sessions will have a value of 0.

After the classifier is trained it can be deployed for detection to separate legitimate flash crowd from APP-DDoS attack. The output of the classifier is used as an input to the mitigation system. The mitigation system terminates current and pending requests of an attack client. It then adds the IP address of the attack client to blacklist. Any future connection attempts are also terminated. On the other hand, a request from a legitimate client is processed as usual.

## EXPERIMENTS

In this section, we discuss evaluation of our proposed approach. We evaluate our proposed approach in terms of the following research questions.

**[RQ1: APP-DDoS detection.]** *Can we detect flash crowds from APP-DDoS attacks using our proposed approach?*

This research question helps us to evaluate our APP-DDoS detection system. More specifically, it deals with evaluation of our candidate classifiers and selecting the best classifier for our detection system.

**[RQ2: Effect of session time.]** *What is the effect of session time on APP-DDoS detection?*

In order to answer RQ2, we use the outperforming classifier from RQ1 to study the effect of session time on the classification performance of our detection system.

**[RQ3: Feature contribution.]** *What is the contribution of each feature for detection?*

In order to answer this research question, we perform qualitative and quantitative analysis to identify features that have higher contribution for detection.

### **Dataset preparation**

In this sub-section, we discuss details of dataset preparation. We describe how we prepared datasets from World Cup 98 access log and experimentally generated APP-DDoS attack access log. Dataset generation involves data preparation of flash crowds and APP-DDoS.

#### **World Cup 98 access log**

World Cup 98 access log data is used in this experiment to model legitimate flash crowds. World Cup 98 dataset [20] consists of all the requests made to the 1998 World Cup Web site ([www.france98.com](http://www.france98.com)) between April 30, 1998 and July 26, 1998. The World Cup website provided information about France 1998 World Cup during that period.

The website was hosted on multiple servers at different locations. The website received large number of requests from all clients who were interested in the World Cup game. 1,352,804,107 requests were received by the website during the

specified period. Although this dataset is old, the characteristics of flash crowd that it models, is not different than what we would have as a flash crowd in these days. World Cup 98 data set is used as a flash crowd dataset in this and related recent researches [3, 8, 11, 12, 15, 21].

The server logs of the World Cup 98 website are provided in a binary format. The tools required to process the dataset are also provided [20]. World Cup 98 dataset is divided in to multiple files with more than one file per day. The number of files depends on the number of requests on that particular day. We have chosen day 66 (June 30, 1998) of the dataset to model flash crowds because it registered maximum number of requests. From the day 66 data, we have chosen server logs of the last three hours of the day. In these three hours, there was a game between Argentina and England, which included 30 minutes extra time, causing high number of requests to the website.

Each entry in the server log files represents a single request. The recorded information for each request is timestamp, clientID, objectID, size, method, status, type and server.

An example of the log entry is shown in Figure 3. The request information contains clientID, time stamp, request type and URL of the requested object, HTTP version, response code and reply size respectively from left to right. The IP address of the client is substituted by auto-generated ID number to keep anonymity.

#### **APP-DDoS attack access log**

To the best of our knowledge, there is no dataset available for APP-DDoS attacks. As a result, we generated APP-DDoS attack on a locally hosted version of the World Cup 98 website. The World Cup 98 website ([www.france98.com](http://www.france98.com)) was hosted locally on closed environment. We performed APP-DDoS attack using a DDoS attack tool, BoNeSi [13]. BoNeSi can generate ICMP, UDP and HTTP

flooding attacks from pre-defined botnet size. This tool also accepts URL lists in a file and requests pages randomly. It also generates summary of the attack statistics.

The experimental setup used to generate APP-DDoS attack is as follows. BoNeSi tool is installed on attack machine and the cached version of World Cup website ([www.france98.com](http://www.france98.com)) is hosted on the target machine. Apache web server application was used to host the website. The attack machine is directly connected to the server machine using cat-6 cable on its network card. BoNeSi attack tool is installed on Ubuntu 16.04 Linux operating system.

In order to conduct attack using BoNeSi tool, the response of the server must be routed back to the attack machine. To achieve this, the IP address of the default gateway of the server must be the same as the IP address of the attack machine. Request flooding and asymmetric attacks are included in the DDoS attack. In request flooding attack, attacker sends application layer requests such as HTTP GET request at higher rate than normal. Request flooding attacks are characterized by high number of requests per machine [1]. In asymmetric attacks, attacker uses requests that require high workload on the server and by making such multiple requests, the attacker easily crushes the server [1]. The request rate in asymmetric attack is usually very low to avoid detection. Repeated one shot attack is a special case of asymmetric attack and hence it is included as part of asymmetric attack. In repeated one-shot attack, the attacker sends requests that require high server workload in multiple sessions to avoid detection.

```
104858 - - [30/Jun/1998:21:41:24 +0000]
"GET /english/images/nav_home_off.gif
HTTP/1.0" 200 828
```

Figure 3: Example entry of World Cup 98 access log.

Request flooding attack was generated by sending large number of requests per source IP. This is achieved by limiting the maximum number of bots involved in the attack. BoNeSi provided 50,000 unique number of IP addresses to be used. In order to cover attack scenarios of very small and very large number of bots, 50 bots were taken for small number of bots and 50,000 were taken for large number of bots.

URL of requested object is randomly chosen from all web objects in the World Cup 98 website.

To simulate asymmetric APP-DDoS attacks, 50,000 bots were deployed. The total request rate is lowered so that the number of requests per bot is small. It is difficult to calculate precise request workload. We assume that the server load is proportional to the reply size.

This assumption works for static web pages whose contents are retrieved from hard drive. All pages on the World Cup 98 website are static pages. Fifty web objects with highest reply size are chosen as a target URL. BoNeSi randomly selects one URL at a time for the request.

The attack generation lasted a day. About 1GB of access log data was obtained after conducting the attack for a day.

### Combined dataset

We merged World Cup 98 dataset access log, representing flash crowd, and APP-DDoS attack access log, representing APP-DDoS attack, to build our evaluation dataset. Since all candidate classifiers require a numerical input data, feature computation is required to convert access log dataset to the numerical dataset. As discussed in Section 3, the detection system uses five features for classification. The features are: *request rate*, *page popularity*, *download rate*, *request inter-arrival time* and *ratio of successful requests*. All features can be computed using equations discussed in Sub-Section 3.1 from server access log.

Each web-page of the World Cup 98 website has associated page popularity value computed using flash crowd access logs. The page popularity is obtained by summing the number of requests on Day 66 access logs for each page and dividing it by total number of requests. Equation 2 is used to compute the page popularity. Page popularity value of each web object is between 0 and 1.

During feature computation, we take the requested web object popularity value. If a client requests more than one web object or more than one request for similar web object in a session time, we use Equation 3 to compute the total page popularity.

A feature computation code is implemented using C++ language. The input to this code is server access logs of both attack and flash crowd. The output of the program is a CSV file. One line in the file represents the information of one client. It contains values of the five features and the label designating if the client is attacker (label value 1) or legitimate flash crowd (label value 0).

For example, the entry [0.35, 0.231039, 1950.65, 15, 1, 0] in the output file is read as *request rate, page popularity, download rate, request inter-arrival time, ratio of successful requests to total number of requests and label* respectively.

We have generated dataset for session time of 20, 40, 60, 120, 180, 240, 300, 360, 420, 480 seconds. Each dataset contains 20,000 entries of which half are flash crowd and the rest are APP-DDoS entries.

We have done experiments on Scikit-learn machine learning tool [22]. Scikit-learn is a python machine learning library that implements machine learning algorithms and provides API for training and testing. When training and testing classifiers, we used 10-fold cross validation technique.

## RESULTS AND DISCUSSION

### APP-DDoS detection

The result of RQ1 showed that it is possible to detect flash crowds from APP-DDoS attack using our proposed approach. The core part of our detection system is a supervised classifier. Although AdaBoost, random forest and decision tree classifiers have very close classification performance, decision tree outperformed all other tested classifiers considering classification time. Decision tree has F1-score of 99.45% and false positive rate of 0.47%.

In order to select a classifier for our detection system, we have tested GNB (Gaussian Naive Bayes), DT (Decision tree), SVML (SVM with linear kernel), SVMP (SVM with polynomial kernel), SVMR (SVM with radial basis kernel), Boost (AdaBoost) and random forest classifiers. We used the dataset generated using a session time of 20 seconds to compare the performance of the classifiers.

Figures 4 and 5 show the F1 and FPR scores of candidate classifiers on 20 second dataset respectively. GNB classifier showed the lowest F1 score of 90.97%. However, the best FPR was obtained by GNB. When lower F1 score is accompanied by lower FPR, it implies that most of the time the classifier guesses the input as flash crowd.

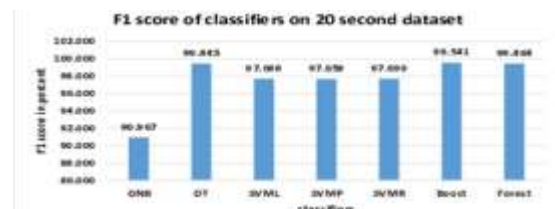


Figure 4: F1 score of candidate classifiers.

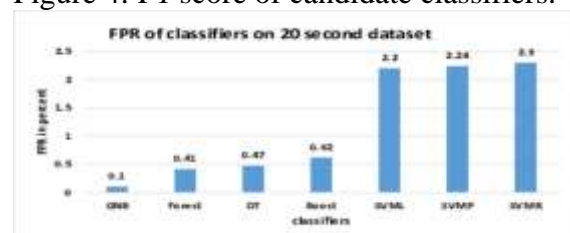


Figure 5: FPR of candidate classifiers.

As it can be seen in Figure 4, DT, Boost and Forest have F1 score higher than 99%. Boost has the highest F1 score of 99.541%. The F1 score of DT and Forest are also very close. We performed a statistical test whether the difference among scores of Forest, Boost and DT are statistically significant. We took the 10 F1 score values, obtained during 10-fold cross validation, of DT, Boost and Forest and performed analysis of variance (ANOVA) test. This test is a parametric test that requires normality check of each variable. We used the Kolomogorov-Simirnove (K-S) test of normality. The result shows that DT, Boost and Forest have a test statistic value of 0.171, 0.244, and 0.151, respectively. The corresponding P-values are 0.882, 0.51 and 0.95, respectively. The low test statistic value and high P-value ( $> 0.05$ ) indicates that each distribution is not significantly different from normal distribution. ANOVA test shows that the difference among the three classifiers is not statistically significant with 95% confidence. The same is true when we do ANOVA on FPR score of the three classifiers. The K-S test of normality of FPR shows that DT, Boost and Forest have a test statistic value of 0.17, 0.23, and 0.18, respectively. The corresponding P-values are 0.82, 0.6, and 0.81, respectively. Since all P-values are above 0.05, we can apply ANOVA test on FPR. The result of the ANOVA test implies that *we can choose any classifier for our APP-DDoS detection*

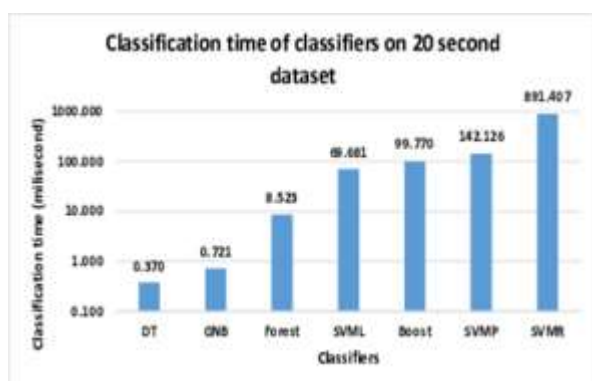


Figure 6: Classification time of candidate classifiers. (Note: The training time was not included in this measurement.)

*among DT, Boost and Forest.*

To see the effect of kernels on SVM performance, we have used ANOVA to test the difference among F1 score of linear, polynomial and radial basis kernels. ANOVA test showed that the difference in F1-score among the three kernels is not statistically significant with 95% confidence. The K-S test of normality on F1-score shows that SVML, SVMMP and SVMR have a test statistic value of 0.143, 0.133 and 0.18 respectively. The corresponding P-values are 0.97, 0.984 and 0.847 respectively.

Figure 6 shows the classification time of candidate classifiers. Classification time measures the time a classifier took to classify 10,000 examples in milliseconds. DT was the fastest classifier with 0.37 milliseconds. The classification time of DT is the smallest because DT mainly traverses a tree during classification. DT training has techniques to make the decision tree depth as small as possible. Traversing small depth trees requires small time. GNB is the second fastest with 0.721 milliseconds. The classification algorithm of GNB is relatively simpler compared to other classifiers. SVM and Boost took high classification time. SVM's require scaling of feature values which makes classification time longer compared to DT and GNB. Even though, Boost does not require scaling, Boost has to make fifty iterations to classify one example. This makes the classification time higher.

The kernel choice had big effect on the classification time of SVM. The computational complexity of SVM during classification is dependent on the complexity of the kernel. Radial basis kernel took 891.407 milliseconds while linear kernel took 69.68 milliseconds.

We have seen that DT, Forest and Boost showed comparable F1 score and FPR. But the classification time of DT is much smaller than Forest and Boost. APP-DDoS detection system must be computationally efficient in order not to contribute to the

already exhausted server resources. DT has bigger advantage compared to Boost and Forest when we consider classification time. That makes DT the recommended classifier to distinguish between flash crowd and APP-DDoS attack.

**Effects of session time**

To investigate effect of session time on the decision tree classifier detection performance, we tested decision tree classifier on data sets generated using 20, 40, 60, 120, 180, 240, 300, 360, 420 and 480 seconds session time. The result showed that the effect of session time on the performance of decision tree classifier is very small. We can choose the smallest session time of 20 seconds for our detection system without losing much in detection accuracy.

Figure 7 shows the effect of session time on F1 score of decision tree classifier. The highest F1 score was observed for 120 second session time. The difference between the highest and lowest F1 score is 0.275 %. This shows that the effect of session time on the F1 score is very small.

Figure 8 shows the effect of session time on FPR score of decision tree classifier. The FPR has even smaller variation among all session times. The difference of FPR among all session times is not statistically significant when we applied ANOVA. The K-S test of normality on FPR shows that all session times have test statistic value less than 0.33 and P-value of test statistics greater than 0.17. This shows that we can apply ANOVA test for the session times.

Session time has direct implication on the response time of the detection system. If the session time is smaller, then the detection system can respond quickly. When we see the difference between F1 score of 120 second, highest F1 score, and 20 second session time, it is only 0.2% and the FPR difference is 0.14%. As we can see, there is very little advantage gained by using 120 second session time compared to 20 second in terms of accuracy.

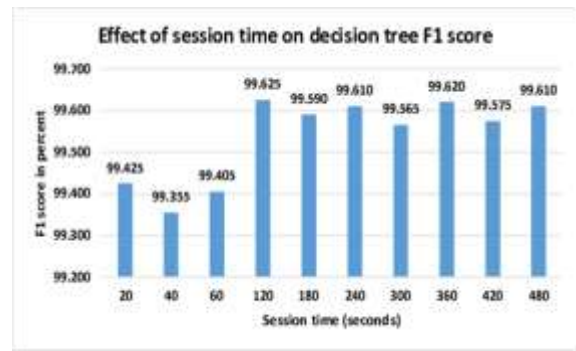


Figure 7: Effect of session time on F1 score of decision tree classifier.

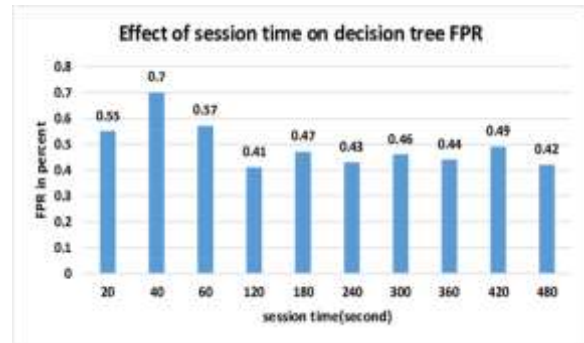


Figure 8: Effect of session time on the FPR score of decision tree classifier

For the smallest session time, 20 second, decision tree has F1 score of 99.425% and FPR of 0.55%. Based on the result obtained, we suggest using 20 second as a session time for feature computation in our detection system.

**Feature contribution**

The result of RQ3 showed that Request rate and download rate have higher contribution for detection among the five features based on qualitative analysis as well as experiment.

To investigate the contribution of each feature for detection, we have made a box plot for each feature using the 20 second data set (see Figure 9). Box plots provide insight on the contribution of each feature for detection through qualitative analysis. For easier visualization, we have normalized each feature value to a mean of zero and unit variance.

The median difference between APP-DDoS and flash is approximately 1 unit for request rate (see Figure 9 (a)). This shows that request rate contribution is potentially

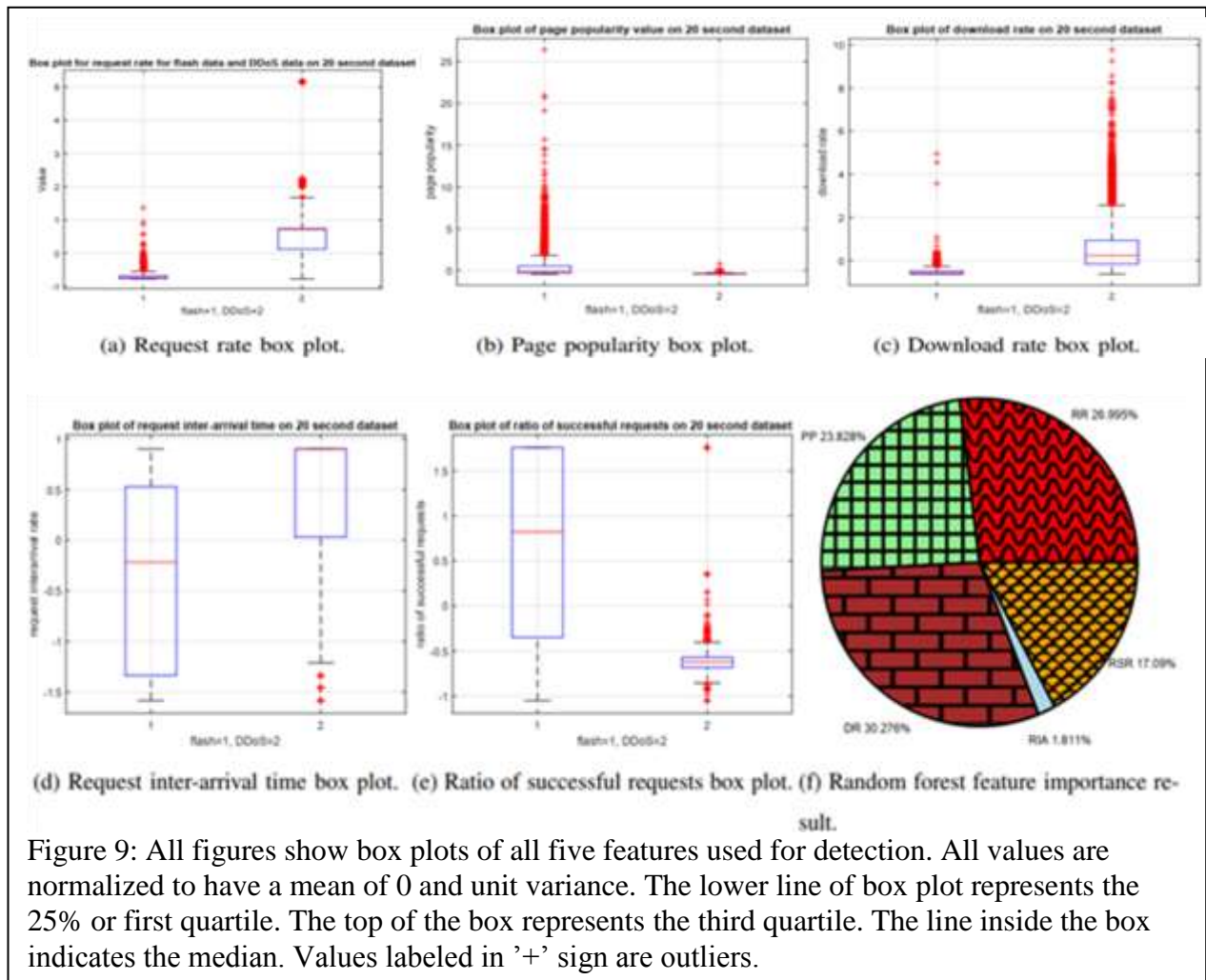


Figure 9: All figures show box plots of all five features used for detection. All values are normalized to have a mean of 0 and unit variance. The lower line of box plot represents the 25% or first quartile. The top of the box represents the third quartile. The line inside the box indicates the median. Values labeled in '+' sign are outliers.

higher. The reason for higher feature contribution is that most of the attack data is request flooding attack which is characterized by higher request rate.

The box plot for page popularity in Figure 9 (b) shows that the median of flash and APP-DDoS is very close and difficult to separate. This means that using page popularity only to separate APP-DDoS attack from flash crowds is difficult.

For the case of download rate in Figure 9 (c), the median difference between APP-DDoS and flash is approximately 0.8 units. Due to the asymmetric APP-DDoS attack, there are many outliers observed on the APP-DDoS box plot. The median difference is close to that of request rate.

Figure 9 (d) shows the box plot of request inter-arrival time (RIA). The difference between the median of APP-DDoS and

flash was approximately 1.05 unit. However, there is high overlap between flash and APP-DDoS boxes. As a result, the potential contribution of RIA for detection is relatively low.

Figure 9 (e) shows the highest median difference between flash and APP-DDoS for ratio of successful requests (RSR), which are approximately 1.35 units. The big median difference occurred because legitimate users in flash crowds request pages by following links which increases the probability of the request being successful. But APP-DDoS attacks select pages randomly which reduces the probability of the request being successful. This shows that RSR has also higher contribution for detection.

To practically test the contribution of each feature, we used random forest classifier. After training the classifier with 20 second

data set, we obtained the feature importance value and plotted a pi-chart as shown in the Figure 9 (f).

The result obtained shows that download rate has the highest contribution of 30.276% and request rate is second with contribution of 26.995%. This result is in coherence with the qualitative analysis of feature importance.

### **Comparison with literature**

To the best of our knowledge, the closest approach in terms of flash crowd and APP-DDoS dataset choice is the work of Daneshgadeh et al. [3]. Their approach leverages machine learning with information distance. They obtained a maximum of 100% recall and 93% precision which corresponds to F1-score of 96.4%. Our approach has 99.45% F1-score which is higher than Daneshgadeh et al.'s approach. They did not evaluate the computational complexity of their approach. Behal et al. [8] proposed an approach based on information theory. They used World Cup 98 dataset together with synthetically generated attack data. They achieved a true positive rate of 95%. It is not possible to compare their approach because we used different APP-DDoS attack dataset.

### **Threats to validity**

#### **a) Internal threats to validity**

Threats to internal validity are mainly caused by variation in instrumentation, and effect due to uncontrolled variables. The instrumentation used to measure variables is computer. We run all experiments on the same computer to avoid instrumental variation. The effect of uncontrolled variables is mainly observed when we measured the classification time of classifiers. The classification time may be affected by external concurrent processes that run on the same computer at the time of the experiment. To address this threat, we have repeated the measurement ten times and took the average. In addition, we

closed non-vital applications during experiment.

#### **b) External threats to validity**

The proposed approach is evaluated on specific flash crowd data set and using only one attack tool. In addition, the flash crowd data set is old which may not represent current flash crowds. Those are major threat to external validity. But our proposed approach is independent of the data. We can test our approach on any data set. We will reevaluate our approach when recent flash crowd data set is available. In addition, we can test our approach on any website without changing our detection system. The other problem is that we only found one DDoS attack tool suitable for our research. But the tool is very flexible with many configurable parameters. We tried to approximate the functionality of other DDoS attack tools by manipulating the configuration. This makes the attack tool more representative.

#### **c) Construct threats to validity**

The main threats to construct validity occur during choice of features for detection and during choice of classifiers. For example, we evaluated six classifiers from all supervised classifiers. But the best classifier may not be among the candidate classifiers. To minimize threats of construct validity because of classifier selection, we selected representative examples from most commonly used supervised machine learning algorithms. Most other supervised classifiers are derivatives of the candidate classifiers. In addition, we did not consider deep learning based classifier as it requires big data for training and we already have good results using other supervised classifiers.

The other potential threat to construct validity is the choice of features. We did not consider all possible features for detection. The reason for this is that if we choose a feature that cannot be computed from our data set, it is difficult to evaluate our proposed approach. But we have

obtained very good result using only six features by systematically choosing features that have higher contribution for detection. When we compute we did not consider requests with 300 response code (redirect). The reason for this is that we cannot determine if the redirected requests are successful or not from our server access log data. This may introduce some bias on the results.

#### **d) Conclusion threat to validity**

The main threats to conclusion validity are too small sample size, measurement error and violation of assumption in test statistics. We have 20,000 examples for both flash and APP-DDoS in our data set. When we observe both APP-DDoS attack and flash crowd data set, the feature values are similar or very close to each other. We believe that our data set sample size is not small for our problem. Since the measurement and experiment was done on computers, the measurement error only comes from computation errors from machines. Hence, the measurement error is negligible. We have used analysis of variance (ANOVA) as test statistics. The assumption of ANOVA is that the data must be normally distributed. In order not to violate this assumption, we tested our data for normality using Kolmogorov-Smirnov test. The result showed that the data used in the ANOVA test is normally distributed.

### **CONCLUSIONS**

In this paper, the problem of identifying application layer DDoS attacks from legitimate flash crowds is addressed. The researchers proposed a supervised machine learning based detection system that uses request rate, page popularity, download rate, request inter-arrival time and ratio of successful requests as features to distinguish between APP-DDoS attack and flash crowds.

Six supervised classifiers are evaluated on our dataset. F1 Score and false positive rate are used as classification performance

evaluation criteria. Classification time is also used as computational complexity evaluation criteria to compare the classifiers. The results show that it is possible to identify APP-DDoS attack from flash crowd with our proposed approach.

Decision tree (DT) outperformed other candidate classifiers considering a combination of F1 score, FPR and classification time as evaluation criteria. DT classifier has 99.445% F1 score, 0.47% FPR and the smallest classification time of 0.37 milliseconds. This shows that DT is a good candidate for the detection system.

Variation of session time has very small impact on the performance of decision tree classifier. The difference between F1 scores when 20 second and 120 second session times are used is very small. In addition, the difference between FPR scores of 20 and 120 seconds session time for decision tree classifier is not statistically significant. This implies that any session time can be chosen with very small impact on performance of the detection system.

From the proposed features, download rate has the highest contribution for detection followed by request rate and page popularity.

#### **Future work**

The main limitation of the research is the unavailability of latest data set of flash crowds. For this research, the World Cup 98 data set is used. The World Cup 98 data set is the standard application layer flash crowd data set up to now even though it was recorded before 19 years. Our proposed approach should be tested on latest data set for more concrete and applicable result. The other limitation was the unavailability of APP-DDoS data set which forced us to use DDoS attack generation tool. Based on the aforementioned limitation of this research, the following points are recommended to be addressed as a future work.

The features used for training as well as prediction are computed per session, but the researchers believe that tracking users usage history will contribute to a more robust detection. In the future, this could be used to address the impact of users history on the performance of the detection approach.

The proposed approach should be tested on a new data set that contains examples of real flash crowds and APP-DDoS attacks. We did not find standard criteria to generate application layer DDoS attack in simulation. Some standard should be set on how to generate APP-DDoS attack that closely resembles real attacks. This can be done by analyzing patterns of real world APP-DDoS attacks.

In our work, due to the limitation of our dataset, we did not consider low rate APP-DDoS attacks. One way to account for low rate APP-DDoS attack is to borrow information from TCP layer about the time it takes to complete a single request. Low rate APP-DDoS attack usually take more time to complete a single request. Furthermore, those attacks usually send partial requests so data about request content may be another clue. One extension, of our work could be to combine information from application layer and TCP layer to effectively handle low rate APP-DDoS attacks.

## REFERENCES

- [1] Ranjan, S., Swaminathan, R., Uysal, M. & Knightly, E. W., *DDoS-Resilient Scheduling to Counter Application Layer Attacks Under Imperfect Detection.*, in INFOCOM, 2006.
- [2] Xu, C., Zhao, G., Xie, G. & Yu, S., *Detection on application layer DDoS using random walk model*, in 2014 IEEE International Conference on Communications (ICC), 2014.
- [3] Daneshgadeh, S., Ahmed, T., Kemmerich, T. & Baykal, N., *Detection of DDoS attacks and flash events using Shannon Entropy, KOAD and Mahalanobis Distance*, in 22nd Conference on Innovation in Clouds, Internet and Networks and Workshops (ICIN), France, 2019.
- [4] Wang, J., Yang, X. & Long, K., *A new relative entropy based app-DDoS detection method*, in Computers and Communications (ISCC), 2010 IEEE Symposium on, 2010.
- [5] Patil, M. M. & Kulkarni, U. L., *Mitigating App-DDoS Attacks on Web Servers*, International Journal of Computer Science and Information Security **9**, 40 (2011).
- [6] Yadav, S. & Selvakumar, S., *Detection of application layer DDoS attack by modeling user behavior using logistic regression*, in Reliability, Infocom Technologies and Optimization (ICRITO)(Trends and Future Directions), 2015 4th International Conference on, 2015.
- [7] Sahoo, K. S., Tiwary, M. & Sahoo, B., *Detection of high rate DDoS attack from flash events using information metrics in software defined networks*, in 10th International Conference on Communication Systems and Networks (COMSNETS), Bengaluru, India, 2018.
- [8] Behal, S., Kumar, K. & Sachdeva, M., *A generalized detection system to detect distributed denial of service attacks and flash events for information theory metrics*, Turkish Journal of Electrical Engineering and Computer Sciences, 1759-1770 (2018).
- [9] Behal, S., Kumar, K. & Sachdeva, M., *D-Face: An anomaly based distributed approach for early detection of DDoS attacks and flash events*, Journal of Network and Computer Application, 49-63 (2018).
- [10] Khalaf, B. A., Mostafa, S. A.,

- Mutapha, A. & Abdullah, N., *An adaptive model for detection and prevention of DDoS and flash crowd flooding attacks*, in International Symposium on Agent, Multi-Agent Systems and Robotics (ISAMSR), Malaysia, 2018.
- [11] Bhandari, A., Sangal, A. L. & Kumar, K., *Characterizing flash events and distributed denial-of-service attacks: an empirical investigation*. Security and Communication Networks **9**, 2222-2239 (2016).
- [12] Yu, S., Zhou, W., Jia, W., Guo, S., Xiang, Y., & Tang, F., *Discriminating DDoS attacks from flash crowds using flow correlation coefficient*, IEEE Transactions on Parallel and Distributed Systems, vol. 23, pp. 1073-1080, 2012.
- [13] Markus-Go, *BoNeSi - the DDoS Botnet Simulator*, 2016. <https://github.com/Markus-Go/bonesi>. Accessed August 2019.
- [14] Yu, J., Li, Z., Chen, H. & Chen, X., *A detection and offense mechanism to defend against application layer DDoS attacks*, in Networking and Services, 2007. ICNS. Third International Conference on, 2007.
- [15] Xie, Y. & Yu, S.-Z., *Monitoring the application-layer DDoS attacks for popular websites*. IEEE/ACM Transactions on networking **17**, 15-25 (2009).
- [16] Ye, C. & Zheng, K., *Detection of application layer distributed denial of service*, in Computer Science and Network Technology (ICCSNT), 2011 International Conference on, 2011.
- [17] Ramamoorthi, A., Subbulakshmi, T. & Shalinie, S. M., *Real time detection and classification of DDoS attacks using enhanced SVM with string kernels*, in Recent Trends in Information Technology (ICRTIT), 2011 International Conference on, 2011.
- [18] Xie, Y. & Yu, S.-Z., *A novel model for detecting application layer DDoS attacks*, in Computer and Computational Sciences, 2006. IMSCCS'06. First International Multi-Symposiums on, 2006.
- [19] Graf, A. B. & Borer, S., *Normalization in support vector machines*, in Pattern Recognition: 23rd DAGM Symposium, Munich, Germany, September 12-14, 2001. Proceedings, 2001.
- [20] Arlitt, M. & Jin, T., *1998 World Cup Web Site Access Logs*, (1998).
- [21] Yu, S., Thapngam, T., Liu, J., Wei, S. & Zhou, W., *Discriminating DDoS flows from flash crowds using information distance*, in NSS 2009: Proceedings of the third International Conference on Network and System Security, 2009.
- [22] Pedregosa, F., Varoquaux, G., Gramfort, A., Michel, V., Thirion, B., Grisel, O., Blondel, M., Prettenhofer, P., Weiss, R., Dubourg, V., Vanderplas, J., Passos, A., Cournapeau, D., Brucher, M., Perrot, M. & Duchesnay, E., *Scikit-learn: Machine Learning in Python*, Journal of Machine Learning Research, vol. 12, pp. 2825-2830, 2011.

## **INTERNATIONAL ADVISORY BOARD**

Prof. Abrham Engida, Michigan State University, USA  
Ato Asrat Bulbula, Consultant, Ethiopia  
Dr. Beshawired Ayalew, Clenson University, USA  
Prof. Carlo Rafele, Politecnico, Italy  
Prof. Ja Choon Koo, Sungkyunkwan University, Korea  
Prof. Amde M. Amde, University of Maryland, USA  
Dr. Esayas Alemayehu, Jimma Institute of Technology, Jimma  
Dr. Fekadu Shewarega, Universitaet-Duisburg, Essen, Germany  
Prof. Gunter Busch, TU-Cottbus, Cottbus, Germany  
Dr. Kibret Mequanint, University of Western Ontario, Canada  
Dr. Mekonnen Gebremichael, University of Connecticut, USA  
Dr. Mulugeta Metaferia, Consultant, Ethiopia  
Prof. Negussie Tebedge, Consultant, Ethiopia  
Dr. Solomon Assefa, IBM, USA  
Dr. Tesfaye Bayou, Consultant, Ethiopia  
Dr. Woubshet Berhanu, Self Help Africa, Ethiopia

## **ACKNOWLEDGEMENTS**

The Editorial Board of Zede Journal of Ethiopian Engineers and Architects would like to express its sincere gratitude to the following individuals for reviewing the manuscripts that were originally submitted for publication in Zede Volume: 38

Adil Zekaria (Dr.)	Nigusse Habtu (Dr.)	Berhanu Bekeko (Managing Editor)
Asrat Worku (Dr.)	Nune Sereenivas (Dr.)	Nardos Gezahegn (Secretary)
Ephrem Teshale (Dr.)	Negussie Tebege (Prof.)	
Getaneh Terefe (Eng.)	Surafel Lemma (Dr.)	
Getachew Alemu (Dr.)	Sosena Mengestu (Dr.)	
Henok Mulugeta (Dr.)	Solomon Workeneh (Dr.)	
Mohammed Abdo (Prof.)	Samuel Lakew (Prof.)	